Technical Report

TR-05-15

# Assessment of copper resistance to stress-corrosion cracking in nitrite solutions by means of joint analysis of acoustic emission measurements, deformation diagrams, qualitative and quantitative fractography, and non-linear fracture mechanics

V G Khanzhin, S A Nikulin
Moscow State Institute of Steel and Alloys

June 2005

**Svensk Kärnbränslehantering AB**
Swedish Nuclear Fuel
and Waste Management Co
Box 5864
SE-102 40 Stockholm  Sweden
Tel 08-459 84 00
+46 8 459 84 00
Fax 08-661 57 19
+46 8 661 57 19

# Assessment of copper resistance to stress-corrosion cracking in nitrite solutions by means of joint analysis of acoustic emission measurements, deformation diagrams, qualitative and quantitative fractography, and non-linear fracture mechanics

V G Khanzhin, S A Nikulin

Moscow State Institute of Steel and Alloys

June 2005

*Keywords:* Copper, Stress-corrosion cracking, Tensile tests, Acoustic emission.

# Abstract

A study of stress-corrosion cracking (SCC) of copper in 0.1M $NaNO_2$ aqueous solution is presented. The fracture kinetics was monitored by measuring the acoustic emission (AE) signals. Macro- and micro-fractography analysis, using scanning electron microscopy (SEM), was employed to investigate the fracture mechanisms. Estimates of stress intensity factor, $K_I$, and $J$-integral were derived in order to assess the resistance of copper to stress-corrosion cracking. Two kinds of SCC tests under continuous circulation of the corrosive solution were employed in the present study:

1. Constant extension rate ($2 \cdot 10^{-6}$ s$^{-1}$) tests on pre-cracked, middle tension (MT) panel specimens.
2. Tests on pre-cracked, compact tension (CT) specimens at a fixed (by a fixing bolt) opening of the crack walls ($\delta = 0.3$ mm, $K_I = 27$ MPa·√m). The time base for these tests was about two months. After the completion of the SCC test, the CT specimen was additionally tested, under a constant-rate (0.02 mm/s) off-center extension.

In the both kinds of tests, the SCC fracture kinetics is found to exhibit two typical stages:

Stage 1: SCC initiation stage (after a certain incubation period, $T_1$, measured to be $T_1 \cong 3$–4 hours for MT specimens under constant extension, the corresponding stress was $\sigma \cong 40$–70 MPa, and $T_1 \cong 200$ hours for CT specimens under a fixed crack wall opening).

Stage 2: Active fracture process (SCC macro-fracture) distinguished by strong AE pulses (which are registered after time $T_2 \cong 8$ hours for MT specimens and $T_2 \cong 800$ hours for CT specimens).

Fractography analysis has shown that the zone of SCC fracture in MT specimens extends to approximately 1,500 μm. A 400–700 μm deep zone of brittle transgranular fracture, which included small areas showing characteristic SCC 'striations', was observed adjacent to the fatigue pre-crack area. At higher straining of MT specimens, the SCC crack front is found to shrink, due to crack tunneling between the shear lips extending from the specimen sides, and also to propagate by characteristic 'SCC lobes', which have a dark appearance and a rough surface morphology. At even higher loads on MT specimens, the SCC process becomes completely suppressed by the developed plastic deformation. The plastic crack opening proceeds by the usual mechanism of ductile fracture. The total crack advance in the CT specimen after 1,200 hours of testing (total time of SCC testing about 1,400 hours, minus the incubation period, 200 hours) was about 1.3 mm, which gives an estimate of the average crack growth rate of order of $3 \cdot 10^{-7}$ mm/s, for the conditions of continuous pumping of the corrosive solution through the crack.

The fracture resistance of copper was estimated to be $K_I = 10.5$ MPa·√m, $J_I = 114.6$ kJ/m$^2$ and $K_I = 29.3$ MPa·√m, $J_I = 578$ kJ/m$^2$ for the first and the second stage of SCC kinetics, respectively. For the off-center loaded CT specimen, pre-embrittled after the static SCC test, the $J$-integral estimates were $J_I = 98.3$ kJ/m$^2$ and $J_I = 380.4$ kJ/m$^2$, for the first and the second kinetic stages of SCC fracture, respectively.

# Contents

# 1 Introduction

The present pilot project has been planned as a logical continuation of previous studies of stress-corrosion cracking in copper /1–3/. Relevance of the stress corrosion cracking to the Swedish nuclear waste storage project is described in Refs /3, 4/. The present analysis is based on the following results, obtained in the previous studies:

1. Slow strain rate tests (SSRT) on small size specimens have shown a considerable (more than 4-fold) reduction of the ductility level for copper in $NaNO_2$ solutions; that is, a sensitivity of the mechanical properties of copper to the environment has been established.
2. A stable, planar growth of a corrosion macro-crack has been achieved under static load conditions on compact tension specimens having side grooves, which are to ensure planarity of the crack propagation under the conditions of extensive plastic deformation of copper. The tests have confirmed, once again, the well-known result that the presence of side grooves introduces certain inaccuracies in the estimates of the stress intensity factor (due to undercutting from the side grooves).
3. Another well-known result has been re-established, that the use of a force parameter of *linear* fracture mechanics ($K_{1C}$) for evaluation the resistance of small-size samples to fracture is problematic because of crack blunting, which occurs when the zone of plastic deformation develops. Under the conditions of severe plastic deformation, the growth of a corrosion crack occurs in an unpredictable fashion (macro-branching).

The present pilot project has been directed at obtaining detailed microscopic and kinetic data regarding the process of stress corrosion cracking of pure copper. In particular, the aims of the present project were:

- to develop methodology and equipment for assessing the resistance of a ductile material to stress-corrosion cracking, by combining mechanical tests with continuous monitoring of the SCC process using acoustic emission,
- to study the mechanisms of stress-corrosion cracking of copper in aqueous solutions,
- to obtain quantitative estimates of the resistance of copper to stress-corrosion cracking, using parameters of linear and non-linear fracture mechanics.

It has been found in previous studies that environmentally assisted fracture of copper occurs in the presence of considerable plastic deformation, which makes it difficult to estimate the resistance of copper to stress-corrosion cracking in terms of the parameters of *linear* fracture mechanics such as $K_{ISCC}$. In the present project, estimates of the copper resistance to stress-corrosion cracking are obtained using the parameters of non-linear fracture mechanics, which are recommendable for use in the presence of considerable plastic deformations, in particular, in cases where extensive plastic flow of material occurs.

In the present study, the critical crack opening has been determined by registering the emission of acoustic signals accompanying the start of SCC crack propagation. The experience in obtaining such estimates has been gained in our previous assessments of the fracture resistance of zirconium cladding tubes, performed on small-size specimens.

# 2 Materials for testing

The present investigation was carried out on copper samples supplied by SKB. The supplied material is found to have a relatively large grain size, up to 200 µm. The micrograph showing the grain structure of a typical sample is presented in Figure 1. The grain size distribution (Figure 1c) was determined using the linear intercept method.

The mechanical properties of the material in air were deduced from the stress-strain diagrams obtained in tensile tests on three cylindrical specimens, whose gauge section was 10 mm in diameter and 50 mm in length, so called 'five-fold' specimens, Figure 2. The results of tensile tests are presented in Figure 3.

The corrosive solution used in the present SCC tests was suggested by SKB: It was a 0.1 $\text{mol}\cdot\text{dm}^{-3}$ $NaNO_2$ solution in water, pH = 7.0–7.1. All the SCC tests were conducted at a free corrosion potential and at room temperature (about 20°C).

# 3 Methodology

## 3.1 SCC tests on middle tension and compact tension specimens

Two different techniques of stress-corrosion tests were used in the present study:

- SCC tests at a constant extension rate (CERT) on middle tension (MT) plate specimens, under continuous circulation of the corrosive solution through the crack. Using these experiments we planned to determine the kinetics of SCC under a slow strain rate extension of the specimen, as well as to obtain quantitative estimates of copper resistance to fracture at different stages of SCC.
- SCC tests on double cantilever beam (DCB) specimens, also called compact tension (CT) specimens, at a fixed initial opening of the crack. In these tests we hoped to estimate the lower bound of the SCC fracture resistance, $K_{ISCC}$, as the critical stress intensity factor at which the SCC crack propagation stops.

### 3.1.1 MT specimens for SCC tests at a constant extension rate loading

In the present study, constant extension rate tests were performed on middle tension panel specimens with a through-thickness crack. The specimen geometry is sketched in Figure 4. The length of the strained (gauge) section of the specimens was equal to 50 mm. Figure 5 shows a panel specimen in the grips of a testing machine, as well as the mechanical diagram recorded in a tensile test performed on a panel specimen in air.

Design of MT panel specimens (principal dimensions 100×50×8) included:

- two mounting holes (14 mm in diameter), for mounting the specimen in the grips of fatigue testing machine «Schenk» during generation of fatigue pre-cracks of variable length,
- one 5-mm central hole for continuous circulation of the corrosive solution through the specimen,
- side grooves on both sides of the plate, across the central hole. Their purpose was to allow for a controllable generation of fatigue pre-cracks in the ductile copper material, as well as to increase the mechanical rigidity of tests, thereby preventing crack branching during crack growth. Each groove was 1-mm deep and 2-mm wide, so that the thickness of the specimen near the notches was equal to 6 mm,
- two identical notches were cut by spark erosion along the side-grooves, in the two opposite directions away from the central hole. The width of the notches was about 300 μm, and their depths were varied from 3 to 6 mm for different specimens,
- sharp fatigue pre-cracks were generated from the notches. The length of pre-cracks was varied from 1 to 7 mm for different specimens. The sum of the central hole diameter, of the depths for the two spark-erosion notches, and of the lengths for the two fatigue-generated pre-cracks is given in Table 1 for each specimen.

The fatigue pre-cracks in the MT panel specimens were generated by applying cyclic loading (at a frequency $f = 20$ Hz, a maximal load of 26 kN, and a minimal load of 1.4 kN) using fatigue testing machine «Schenk». Characteristic surface morphology of fatigue fracture is shown in Figure 6.

### 3.1.2 CT specimens for SCC tests at a fixed (constant) crack opening

Double cantilever beam specimens, otherwise called compact tension specimens, for tests at a fixed (constant) crack opening are drawn in Figure 7. The specimens were designed for use in SCC tests for obtaining estimates of $K_{ISCC}$. Fixed crack opening, which was secured using a fixing bolt, provided a decreasing stress intensity factor at the crack tip during crack growth. In these experiments, $K_{ISCC}$ is determined as the critical stress intensity factor at which the crack growth stops (monitored using AE).

Design of CT specimens (principal dimensions 100×60×23) included:

- a 6-mm wide notch with a V-shaped tip,
- a sharp fatigue pre-crack generated from the notch tip (the length of pre-cracks was varied from 2 to 16 mm for different specimens),
- two mounting holes (14 mm in diameter), for mounting the specimen in the grips of fatigue testing machine «Schenk» during fatigue pre-crack generation,
- side grooves (3-mm wide, 1-mm deep) which were made in order to increase the rigidity of tests, as well as to prevent crack branching,
- a 10-mm steel bolt and a 10-mm steel dowel (supporting cylinder), for adjusting and fixing the crack opening,
- a cylindrical pedestal (at the back of the specimen) for attaching the AE sensor as well as for mounting the electronic module for signal pre-amplification and pre-processing (Figure 7).

CT specimens had fatigue-generated pre-cracks of various lengths (2–16 mm), for obtaining different levels of stress intensity factors in different specimens at a fixed opening of the specimen. The pre-cracks were generated by applying a cyclic load to the specimens, with a maximum load of 10 kN and a minimum load of 0.6 kN in each cycle. The frequency of cyclic load on fatigue testing machine «Schenk» was $f = 10$ Hz. A graduation dependence wall opening – crack length is shown in Figure 8. Figure 6 shows the surface morphology of fatigue fracture that is characteristic of the studied material.

### 3.1.3 Methodology of SCC tests, combined with acoustic emission measurements, of copper specimens in 0.1M aqueous $NaNO_2$ solution

Figure 9 shows a drawing and three photos of panel specimens connected to the circulating solution system pipeline. Figure 10 shows a block diagram of the experimental setup for studies of the SCC kinetics on panel copper specimens using constant extension rate tests (CERT) combined with acoustic emission (AE) monitoring. The loading assembly of testing machine (the assembly includes plastic cups with pipes for continuous circulation of the corrosive solution as well as AE sensors, all attached to the specimen) is shown in Figure 11.

The experimental setup shown in Figure 10 consists of the following main functional blocks:

- system for slow-rate tensile loading of a panel specimen,
- system for continuous circulation of the corrosive solution through the specimen during SCC tests,
- two-channel computerized system for detection, continuous recording, and subsequent processing of the AE signals.

### *System for mechanical loading of MT panel specimens*

Panel specimen (Figure 5) was mounted in flat (serrated) grips of a universal testing machine. Flat grips of the testing machine covered the mounting holes (near the ends of the specimens) that had been used for fastening the specimen in the cyclic fatigue machine. The gauge part of the specimen (the distance between the edges of the flat grips) was equal to 50 mm. The specimens were continuously loaded at a constant extension rate of $2 \cdot 10^{-6}$ $s^{-1}$ during the SCC tests; the testing time was varied between 17 and 24 hours.

### *Circulating solution system*

In the present work, 0.1M $NaNO_2$ aqueous solution (6.92 g $NaNO_2$ per one liter of distilled water, pH = 7.0–7.1) was used as the corrosive solution. In the present work, we used continuous pumping of the corrosive solution, a kind of corrosion experiment in stirred solution. It is commonly accepted that stirring of the solution increases the corrosion rate by accelerating the removal of corrosion products, as well as by facilitating the supply of oxygen to cathode zones. Stirring of the corrosive solution was implemented by continuously pumping the solution through the central hole of the specimen during the test. The circulating solution system included a hermetically sealed reservoir (item 6 in Figure 10) containing 5 liters of $NaNO_2$ solution. Circulation was driven by a pump (item 7 in Figure 10) installed on top of the reservoir. A circulation pump from the cooling system of a small-scale electron microscope «Tesla» was used for that purpose. The assembly of the reservoir with the pump is shown in Figure 11b. During the test, the solution was pumped through a line of flexible pipes, at a velocity of about 1 m/s. The internal diameter of the pipes was 8 mm, and the total length of the pipeline was up to 8 meters. In order to reduce the acoustic noise originated by the operating pump, the reservoir with the pump was put into an acoustically insulated box, Figure 11c. To suppress the transmission of noise through the liquid, acoustic filters (item 8 in Figure 10) were installed into the pipeline. Suppression of noise in acoustic filters occurs due to percolation of the solution through media with different acoustic resistances (filtering gaskets). Two small cups of plastic glass were hermetically attached, using specially shaped rubber gaskets, to the opposite sides of a specimen, Figures 9b–d and 11a. The cups were connected to the pipeline through specially designed couplings. In this way a closed-loop recirculation system was built.

### *Two-channel computerized system for detection, recording, and processing of the AE signals during long-term tests*

Acoustic emission was continuously monitored during the stress corrosion tests on the copper specimens. Two specially designed AE sensors were attached to the (preliminary polished) opposite edge sides of a panel specimen (item 4, Figure 10), in front of the stress-corrosion zone. With the purpose of reducing the possible interference of electromagnetic noise from external sources, piezoelectric sensors were made physically integral with specially designed small-size analog pre-amplifier, to form a single module for AE signal detection and pre-amplification (item 4 in Figure 10). An additional proofing from external electromagnetic noise was ensured by running the signal detection and pre-amplification modules off an independent power source (a storage battery).

A two-channel AE signal detection scheme was utilized in the present work. Application of this scheme allowed us to meet simultaneously the two (often appearing incompatible) main requirements to AE signal detection in the SCC studies:

1. Ability to detect low-amplitude, high-frequency signals (‘continuous’ emission), in order to monitor slow evolution of the corrosion sites.

2. Ability to detect relatively seldom events of low-frequency, high-amplitude AE pulses (‘burst’ or ‘discontinuous’ emission) from macroscopic cracking in the material embrittled due to corrosion.

The analog processing modules (item 4, Figure 10) included:

- compact pre-amplifiers and amplifiers,
- low-frequency and high-frequency filters,
- signal detectors and normalizers whose characteristics were adjusted for the subsequent analog-to-digital transformation of the AE signals in the input controller of a PC (item 9, Figure 10).

The following frequency and dynamical characteristics were chosen for the two channels:

1. Channel for monitoring of ‘continuous’ emission:
   - frequency band 100 kHz – 20 MHz,
   - dynamical range up to 30 dB.
2. Channel for monitoring of ‘burst’ emission from macro-fracture events during SCC:
   - frequency band 10 kHz – 1 MHz,
   - dynamical range up to 70 dB.

Thus, the use of two frequency-separated channels for the AE signal detection allows one to monitor the corrosion processes that occur on different structural levels. The pre-processed AE signals are fed into the multi-channel 12-bit digital input controller (L-Card 1250) of the computerized measuring system (item 9 in Figure 10). The controller was programmed to operate at a certain frequency of digital signal processing during a certain time interval of continuous monitoring. In order to prevent information losses due to possible malfunctions, the computerized measuring system was rebooted by operator several times during a test. At each reboot, the accumulated data were archived on the hard disk drive of the computer. The duration of a reboot procedure was about 1–2 minutes. Each of the 3–4 files that were recorded during one test contained the data accumulated during 3 to 10 hours of continuous monitoring. The SCC monitoring by AE was performed using the LabVIEW interface. The files with the accumulated information were processed using specialized software. Typical AE diagrams are shown in Figures 16–20.

## 3.2 SCC kinetics monitoring using acoustic emission

Figure 14 shows: (a) installation for SCC tests combined with AE monitoring, (b) panel specimen with the attached AE sensor that is made physically integral with small-size electronic module for analog pre-processing, and (c) placement of the AE sensors on a specimen during tests. Figure 15 shows mounting of an AE sensor and of an analog pre-processing module on the cylindrical pedestal of a CT specimen (a, b), as well as a photo of a CT specimen with the installed electronic module and with the attached system for continuous circulation of corrosive solution through the crack (c).

Load (*P*) – displacement (*f*) diagrams were recorded continuously during extension of the panel specimens. The recording device had the following scales: Y-axis 1 cm = 2.5 kN load, X-axis 1 cm = 0.1 mm displacement. Joint load-displacement and AE diagrams (aligned using time markings) are shown in Figure 20.

The AE signal amplitudes (dB) were expressed relative to the noise level during the test:

$$V_p = 20\log_{10} (V_{signal} / V_{noise}) \text{ dB} \tag{1}$$

Here $V_{signal}$ is the AE signal amplitude and $V_{noise}$ is the noise level, both expressed in volts.

The noise level was determined using the following standard technique. At the beginning of test on every specimen (20–30 minutes after the test had been started) the loading was discontinued and the specimen was completely unloaded and then loaded again. The level of noise was measured during the second loading. By virtue of the Kaiser effect, acoustic emission does not occur during secondary loading until the primary load level is exceeded. All the signals during reloading can be regarded as electrical and mechanical noise. This noise was recorded, for each specimen, during a time interval of 20 minutes, which corresponded to about $10^6$ data points of the computerized measuring system. The noise level was calculated automatically by the computerized system, as an average over all the registered data points. The load was controlled using the load-displacement diagram that was being recorded. Joint analysis of the mechanical and AE diagrams allowed us to determine the load, $P$, and displacement, $f$, that correspond to the beginning of different stages of the SCC kinetics, which were discriminated by acoustic emission.

The acoustic emission signals recorded during the static SCC test on a CT specimen are presented in Figure 19. Figures 19a–d show typical 9-hour records, and Figure 19d shows the whole AE diagram recorded during the first 0–500 hours of the static SCC test (there was an interval, in the middle of the test, when the SCC process went on unmonitored, because of a failure in the computer system). Figure 21 presents the AE signals and a joint AE and deformation diagram recorded during a constant extension rate (0.22 mm/s) test on the CT specimen, which was performed after completion of the static SCC test to obtain estimates of the fracture resistance parameters on the CT specimen.

## 3.3 Quantitative estimate of copper resistance to SCC

For the given specimen geometry and test design, a joint analysis of the SCC kinetics and of the load-displacement ($P$-$f$) diagrams allows one to obtain quantitative estimates of the parameters of linear ($K_I$) and non-linear ($J_I$) fracture mechanics. These parameters may be regarded as measures of resistance of copper to stress-corrosion cracking.

### 3.3.1 Stress intensity factor $K_I$ for test designs 'Panel specimen with a through-thickness crack under uniaxial extension' and 'Pre-cracked compact tension specimen under off-center extension'

Stress intensity factor was calculated for the following test design: A center cracked panel specimen with a through-thickness crack of a size 2$L$, under stress σ in the cross-section of the crack /5/:

$$K_I = \sigma \cdot \sqrt{\pi L} \cdot Y(\lambda) \tag{2}$$

where $Y(\lambda)$ is the so-called $K$-calibration factor. In the present work, it was determined as

$Y(\lambda) = 1 + 0.128 \cdot \lambda - 0.288 \cdot \lambda^2 + 1.525 \cdot \lambda^3$.

For the 10 tested MT specimens, the relative depth of the crack, $\lambda = L/b$ (where $b = 25$ mm is the half-width of a specimen), was varied in the range $\lambda = 0.25–0.36$; thus giving the values of the $K$-calibration factor $Y(\lambda) = 1.03–1.10$. The estimates of $K_I$ were obtained using the stress values that corresponded to the characteristic stages of SCC discriminated by AE (Table 2, Figure 20).

**Table 1. Initial crack length, *2L*, in the tested specimens. Applied stress, *P*, at which AE indicating the given SCC stage was detected.**

| Specimen number | Initial crack length, mm | SCC initiation stage Load *P*, kN | SCC macrofracture stage Load *P*, kN |
|---|---|---|---|
| 1 | 17.9 | 12.7 | 35.0 |
| 2 | 14.1 | 16.3 | 36.3 |
| 3 | 15.6 | 16.3 | 35.6 |
| 4 | 12.4 | 17.3 | 59.6 |
| 5 | 17.6 | 12.5 | 27.5 |
| 6 | 13.7 | 12.0 | 47.5 |
| 7 | 16.9 | 12.5 | 38.0 |
| 8 | 15.4 | 14.3 | 40.5 |
| 9 | 13.9 | 9.5 | 43.8 |
| 10 | 16.0 | 14.0 | 36.8 |

Immediately after completion of the static (total time 1,400 hours) SCC test at a fixed crack opening, the CT specimen was tensile tested at a constant strain rate of 0.02 mm/s. The fracture of the pre-embrittled (due to the long exposure to the corrosive solution) material was monitored by AE (Figure 21). For comparison purposes, the force criterion of fracture resistance, $K_I$, was calculated at the first stage of the fracture kinetics (Figure 21c), for the double cantilever beam (DCB) specimen geometry ($a \geq h$):

$$K_I = \frac{2 \cdot \sqrt{3} \cdot P \cdot a}{h \cdot \sqrt{h} \cdot t} \qquad (3)$$

where:

$P = 14.1$ kN – load at which active fracture of the pre-embrittled CT specimen is detected by AE under the constant rate testing,

$a = 60$ mm – total crack length (from the line of applied force to the crack tip),

$h = 29.5$ mm – half of the specimen height (Figure 7),

$t = 20.5$ mm – thickness of the CT specimen between the side grooves (Figure 7).

### 3.3.2 Energy criterion of resistance to cracking, $J_I$-integral

Corrosion-assisted fracture of copper, as observed on pre-cracked panel specimens under continuous extension, is accompanied by evolving plastic deformation. Therefore, for such kinetic regimes the resistance to cracking was also estimated employing the widely-used criterion of elastoplastic fracture mechanics – the *J*-integral /7/. In the present work, the *J*-integral was calculated according to the procedure suggested by J A Begley and J D Landes /8/, using equation derived by J R Rice /7/, for a specimen of thickness *t*:

$$J = -\frac{1}{t}\left(\frac{dA}{dL}\right) \tag{4}$$

where:

$A$ = mechanical energy absorbed during deformation of the specimen (work of deformation);

$L$ = crack length (Table 1);

$t$ = 6 mm – thickness of the specimen between the side grooves.

The procedure to estimate the $J_I$-integral included the following steps (Figure 22):

1. Load-displacement diagrams are obtained for specimens having pre-cracks of different lengths (examples are presented in Figure 20).
2. (Figure 22a): The absorbed mechanical energy during deformation of every specimen is calculated (as the area under the *P*-*f* curve, from the origin to the *f* value identified by the AE as the start of a certain stage of SCC, see Figure 20).
3. (Figure 22b): Dependencies 'work of deformation vs initial crack length' are plotted.
4. The *J*-integral value is calculated using these dependencies and Equation (4).
5. (Figure 22c): Dependencies '*J*-integral vs *f*' are plotted for specimens with different initial pre-cracks.
6. The *J*-integral values that correspond to different stages of SCC (such as SCC initiation and SCC macro-fracture), are calculated using the dependencies obtained on step 5, see Table 2.

For the tensile test (after completion the static SCC test) on the CT specimen, the energy criterion of fracture resistance, *J*-integral, was calculated, for comparison purposes, using the following simplified dependence /9/:

$$J = \frac{2A}{b \cdot t}\frac{(1+\alpha)}{(1+\alpha^2)} \tag{5}$$

$$\alpha = \left[\left(\frac{2a}{b}\right)^2 + 2\left(\frac{2a}{b}\right) + 2\right]^{1/2} - \left(\frac{2a}{b} + 1\right)$$

where:

A = integrated area under the load "*P*" versus displacement "*f*" diagram, from $f = 0$ to the *f* value corresponding to the beginning of the first and the second stage of fracture kinetics, during constant rate extension test on the CT specimen (Figure 21c), $A_1 = 28.2$ J ($P_1 = 14.1$ kN) and $A_2 = 109.2$ J ($P_2 = 15.1$ kN), respectively,

$b$ = 28 mm – length of the unbroken part of the specimen (Figure 7),

$t$ = 20.5 mm – thickness of the CT specimen between the side grooves (Figure 7).

### 3.3.3 Quantitative estimate of copper resistance to SCC obtained using CT specimens at a fixed (constant) crack opening

Fixed opening of the crack walls in a CT specimen creates conditions of a decreasing stress intensity factor, $K_{\mathrm{I}}$, at the crack tip during the crack growth. Since $K_{\mathrm{I}}$ decreases as a function of time, the crack shall eventually stop. The value $K_{\mathrm{I}}$ at which the SCC crack propagation is found to stop in these experiments may be taken as an estimate of $K_{\mathrm{ISCC}}$ for copper in 0.1M $NaNO_2$ solution.

The stress intensity factor near the crack tip at the beginning of a test (after the initial opening of the crack walls), as well as at the end of the test (when the crack had stopped) was calculated /5, 6/ using the principles of linear fracture mechanics, from the dimensions of the specimen (see Figure 7) and the elastic modulus of copper, E = 121 GPa,

$$K_{\mathrm{I}} = \frac{E \cdot \delta \cdot h \cdot \left[3h(a+0.6h)^2 + h^3\right]^{1/2}}{4\left[(a+0.6h)^3 + h^2 a\right]} \qquad (6)$$

where:

$E$ = elastic (Young's) modulus,

$a$ = total crack length (from the line of applied force to the crack tip) measured after the test,

$\delta$ = crack opening, 0.3 mm,

$h$ = 30 mm – half of the specimen height.

## 3.4 Metallographic and fractographic studies

Quantitative estimates of the grain structure of the material were performed using the linear intercept method (Figure 1). The cross-sections were analyzed on an optical microscope «METAM PB-23» at magnifications ×80–300. The fracture surfaces were examined with an optical microscope «ПМТ-3M» at magnifications up to ×500. Quantitative fractography analysis was performed with a scanning electron microscope «HITACHI S-800» at magnifications up to ×5,000.

# 4 Results and discussion

## 4.1 Kinetics of SCC fracture in copper panel specimens

Typical AE diagrams, recorded during the SCC tests on copper specimens, are shown in Figures 16–20. Two types of AE signals can be distinguished:

- signals of ‘continuous’ emission, Figures 16a,b,
- signals of ‘burst’ emission, can be seen as pulses of relatively high (20–50 dB) amplitude in Figures 16c,d.

The individual signals of ‘continuous’ emission are short, overlapping pulses of relatively small amplitude. Often, the signals of ‘continuous’ emission result from micro-fracture events originated by the chemical or electrochemical processes that occur during SCC /11/. For instance, the process of electrochemical etching/polishing of metals is usually accompanied by easily detectable ‘continuous’ acoustic emission. The power of the AE signal in such experiments can be varied by changing the electric current circulating in the electrochemical cell. In our SCC tests on copper specimens, the level of ‘continuous’ emission changed as a function of the applied load, which indicates that the SCC process is irregular. Variation of the SCC character, on a short time-scale, is seen as short (0.01–1 s) rises or falls of the signal. On a longer time-scale, the AE diagrams exhibit a slow (1–2 hours) fall-off of the ‘continuous’ AE level, corresponding to either a decay of the SCC process or a change of its mechanism (Figures 16a,b).

A change in the mechanism of corrosion-assisted fracture often manifests itself as a change in the AE character. In the case of our interest, a decay of the process leads to the occurrence of strong AE bursts (Figure 16c,d). At low load levels a slow development of the corrosion sites takes place, whereas at higher load levels the material, embrittled due to corrosion, seems to fail by rupture of ligaments between the fracture facets (Figures 33–35). Our technique allowed us to reliably detect the ‘continuous’ acoustic emission accompanying small-scale SCC processes, and in our estimates of material’s resistance to fracture we used the signals of both ‘burst’ and ‘continuous’ acoustic emission as parameters characterizing the fracture kinetics (Figure 20). The AE diagrams measured during loading of MT panel specimens show two distinct stages:

1. Some 3–4 hours (typical SCC ‘incubation time’) after the start of a test ($f = 1.5$–2 mm), first AE pulses of 5–10 dB in amplitude are detected. Later, the intensity of such signals may increase or decrease, but the fact that such signals appear is characteristic of the recorded AE diagrams (Figure 20) and is well reproduced. In the following, this (*first*) stage of the SCC kinetics will be referred to as *‘SCC initiation’*.
2. Some 5–10 hours after the start of a test ($f = 4$–6 mm), high-amplitude (20–50 dB) AE pulses (bursts), induced by macro-fracture events in the material, are reliably detected. Macro-fracture events under SCC are usually ‘prepared for’ by the preceding micro-fracturing of the material. In the following, this (*second*) stage of SCC kinetics will be referred to as *‘SCC macro-fracture’*, see Figure 20.

For compact tension (CT) specimens the SCC initiation stage is found to begin after about 200 hours ($V_P = 6$–15 dB), see Figure 19.

## 4.2 Fractographic observations and SCC mechanisms: MT panel specimens

Fracture mechanisms of copper panel specimens during the constant extension rate tests under continuous pumping of corrosive 0.1M $NaNO_2$ solution through the central crack were studied using the macro- and micro-fractograms obtained by scanning electron microscopy (SEM). A specimen prepared for SEM analysis is shown in Figure 23a. Typical SEM micrographs are presented in Figures 24–39.

Figures 6 and 24b–d show micrographs of the fatigue pre-crack zone. Materials fracture within this zone has a mixed character, with areas of transgranular and intergranular fracture. Even after the long exposure to the corrosive solution during the time of the SCC CERT test, the fracture surface in the fatigue pre-crack zone does not show significant traces of corrosion.

At the initial stage of the specimen extension at a constant rate, when the crack opening occurs without detectable stress corrosion cracking, the fracture surface near the tip of the fatigue pre-crack has a so-called ‘stretch zone’, which is characteristic of ductile materials such as copper. The mechanism of the stretch zone formation is sketched in Figure 24, where we also give a micrograph showing the characteristic ‘smooth’ surface morphology of the stretch zone that is adjacent to the fatigue pre-crack front.

The SCC crack starts from the fatigue pre-crack tip and propagates in the transgranular fracture mode. The areas of brittle, transgranular SCC fracture sometimes exhibit easily noticeable ‘crystallographic’ orientations of the fracture surface, see Figure 25a–d.

At final stages of CERT tests on MT specimens we observe the usual ductile fracture, by rupture of walls between the pores formed at non-metallic inclusions (Figure 27). Similar fracture surface appearance is observed for cylindrical specimens tested in air (Figure 3b).

We observe that the evolution of SCC character in the tested panel specimens occurs in several steps. For example, a transition from a transgranular fracture mode (cleavage along parallel, crystallographic planes) to a fracture mode with ‘striations’ is shown in Figure 28a. Intermittent character of corrosion damage manifests itself in the characteristic striations that are seen in the fracture micrographs (Figure 28b–d). The intermittent character of SCC in copper and some other ductile fcc materials is well known, but its microscopic origin is still under debate /4/. Figure 29 illustrates one of the proposed mechanisms of discontinuous (stepwise) crack propagation during SCC – through the oxide film rupture caused by the dislocation activity within slip lines /13/. The possibility of crack growth by slow changes of the load applied to the specimen in $NaNO_2$ solution, due to the oxide film rupture by dislocations exiting the specimen surface, was also discussed in Ref /1/ on page 15.

The microstructure of the material is rather complex. In particular, it shows the presence of annealing twins (Figure 1). The microstructure is sometimes found to manifest itself in alternating changes of the crack propagation plane, which produce a 3-dimensional morphology of the fracture surface, with a characteristic length-scale of about 30 μm, see Figure 36.

As the load on MT specimen increases with time during the test, the topography of SCC striations (Figure 28) becomes smoother (Figure 30). Etching of the fracture surface at the crack tip appears to be enhanced: The fracture surface has a dark appearance characteristic of a corroded surface (Figure 31).

At late stages of tests, the SCC propagation is found to occur by several ‘lobes’ or ‘patches’, as schematically shown in Figures 31 and 33. Plastic deformation, which extends from both sides of the specimen into the SCC fracture zone, leads to a narrowing of the SCC crack front (the so-called ‘crack tunneling’ effect), see Figure 32. As the plastic deformation evolves with increasing load on the specimen, the SCC process becomes extinguished: the crack opening is almost entirely controlled by ductile fracture. SCC ‘patches’ can still be found occasionally at different levels of the ductile crack front, as shown in Figure 37. At a later stage, a fully plastic crack opening is observed, by usual ductile failure of the material (Figure 27).

Totally, five different SCC fracture morphologies, corresponding to different fracture mechanisms, have been identified using fractographic studies of the SCC tested specimens:

1. Transgranular cleavage along several parallel planes (Figure 25a–h).
2. Fracture by cleavage steps (Figure 25i–l).
3. Brittle transgranular ‘vertical’ cleavage (see Figure 35 showing ‘ridges’ on the fracture surface).
4. Brittle transgranular cleavage with crack arrest markings at slip lines produced by slip bands (Figure 28).
5. Failure by SCC ‘lobes’ or ‘patches’ (Figures 31–32).

The acoustic emission (AE) diagrams, Figures 18 and 20, show that there are several types of fracture kinetics for slowly strained pre-cracked specimens under the conditions of continuous pumping of the corrosive solution through the crack. Some AE diagrams distinctly show that the first stage (SCC initiation) of stress-corrosion cracking is followed by the second stage (SCC macro-fracture) distinguished by strong acoustic pulses from macro- and micro-fracture events in the specimen. The fracture process may decay and re-activate. As a result, the AE-diagrams obtained under nominally identical conditions, and on similar specimens, may look quite different. This may be a consequence of the poor reproducibility of corrosion processes in general, at least according to our experience.

A possible explanation of the observed differencies in kinetics and fractography for similar specimens is that the SCC zone that is adjacent to the fatigue crack front is relatively narrow; typically below 1,500 μm (the zone of brittle fracture is as narrow as 400–700 μm). Keeping in mind the large grain size in the studied material (see Figure 1), one can expect that the crack initiation and propagation in the SCC zone may be strongly influenced by the particular grain orientations.

Indeed, it is known that the electrochemical properties of different grains of a copper single crystal are notably different. For instance, the dependence of dissolution rate on the grain orientation produces etching patterns on the surface of copper sheets with rolling textures. Similarly, different SCC mechanisms may operate at different positions along the crack front in a large-grain material, something what we probably observe.

Let us now discuss the fractograms that do not show SCC, Figure 24b–d. Fatigue pre-crack region can be seen at the bottom in these figures. A mixture of transgranular and intergranular fracture is observed in this region. Immediately adjacent to the fatigue pre-crack region is a so-called ‘region of plastic advance of the crack’, the latter is typically observed on notched specimens of ductile materials. This region, also called a ‘stretch zone’, is quite extended in the present case. It is believed that such regions are formed by shear stresses when the material splits along the slip bands that have been prepared by the preceding plastic deformation. /10/. Two sketches illustrating the development of a stretch zone at the crack tip during crack opening are shown in Figure 24a.

Another typical element of the fracture surface is the well-developed system of voids (ductile fracture) that forms during mechanical rupture of each specimen after completion of the test (see, for instance, Figures 3b and 27).

The third useful element for our analysis is the pattern of fractured ligaments (Figure 33); their fracture may be ductile (Figure 34) or brittle (Figure 35). The development and fracture of a ligament are schematically illustrated in Figures 34a and 35a. As the crack walls are becoming more and more separated under the action of external load, the ligament connecting two adjacent crack segments becomes thinner (necking) and eventually fails in a more or less ductile fashion, thereby producing different fracture geometries such as a cup & cone geometry, or a fully ductile necking of the cross-section area into a point, or, as shown in Figure 34, a fully ductile necking of a flat ligament into a line. The presence of ridges (ruptured ligaments) on the fracture surface is a signature of micro-cracking ahead of the crack tip (Figure 33).

Let us now review some of the micrographs showing fractured ligaments in the fractured copper specimens:

- Chains of short ridges (ruptured ligaments) can be seen on the left-hand side of Figure 34b. Crack propagation direction is from bottom to top.
- A single ridge (not a chain) formed by ductile rupture of a ligament (Figure 34c). Due to a high ductility of copper the ligament was reduced in the cross-section area to a line, by necking. A matching ridge can be found on the opposite fracture surface.
- A pile of transcrystalline microfacets can be seen in the central area of Figure 34d (similar microfacets can be seen in Figure 2 of Ref /6/). To the left of the central area there is a ridge which remained after the corresponding ligament has been reduced in the cross-section area to a line. This is a unique place in the specimen where the crystallographic orientations happened to be such that one can see the details of the ligament deformation – its side surface is densely covered with steps of slip lines.
- There is yet another kind of ligaments, which is relevant for one of the SCC mechanisms of copper. A ligament connecting two adjacent SCC patches failed in a brittle fashion, producing 'vertical' transgranular cracks (Figure 35). Figure 35a shows a scheme (according to Bridgman /14/) of the stress state of material in a ligament. The stress state is triaxial, due to the curvature of the ligament surface. The shear stresses cause opening of vertical cracks in the material embrittled by corrosion. As a result, one finds characteristic 'ridges' between the SCC zones, Figure 35b–d.

One particularly interesting model of the SCC mechanism involves slip lines /12, 15–17/. According to this model, the protective film on the surface is ruptured in the vicinity of the crack tip, as a result of localized plastic flow. The slip lines develop a high pressure which tears the protective film. The so-formed areas of juvenile, unprotected metal undergo rapid anodic dissolution. The dissolution process is localized near the crack tip, within the slip plane where the plastic flow process is still active (or within a stack of slip lines – depending on the scale of the observed surface steps, 0.75–1.4 µm – see Figures 28, 29). In this SCC zone, the crack area that is left far behind the crack tip is effectively unloaded and does not take part in the cracking process. This area can only be additionally etched by the flowing corrosive solution, if the solution allows for that. The 0.1M $NaNO_2$ solution that was used in the present work was inactive in that respect: The fracture surface of the fatigue crack was preserved in the solution during tens of hours.

## 4.3 Fractographic observations and SCC mechanisms: CT specimens

At present, one SCC test on a compact tension (CT) specimen has been completed. The test was performed at a fixed crack opening, δ in Equation (4), using continuous circulation of the 0.1M $NaNO_2$ solution through the crack (see Figure 12). The test duration was 1,400 hours. Immediately after the completion of test, while the corrosive solution was still present at the crack tip, an off-center tensile loading was applied to the specimen; the deformation rate was 0.02 mm/s. (Figure 21a). Deformation diagram was recorded during the tensile test, in order to derive estimates of crack resistance parameters, $K_I$ and $J_I$, using the standard methodology for compact tension specimens, Equations (3)–(5). After the tensile test, the specimen was pulled apart and prepared for SEM analysis; see Figure 23b,c. Typical SEM micrographs are shown in Figures 38 and 39.

The fracture mode in the fatigue pre-crack zone, as well as in the SCC zone, is found to be mostly transgranular. Characteristic river-band and feather-like patterns are present on the fracture surfaces (see Figures 38, 39). However, the fracture surface of the CT specimen, including the fatigue pre-crack zone, appears much more corroded and is covered with a thick oxide film after the static SCC test (see Figures 23b, 38, and 39), as compared to the fracture surface of CERT-SCC tested MT panel specimens. Therefore, it was relatively difficult to locate the boundary between the fatigue pre-crack zone and the SCC zone (see Figure 39b), while the final crack length could be easily measured, using the stretch zone that formed when the specimen was off-center loaded after completion of the static SCC test (Figure 23c). The average depth of corrosion-assisted crack growth (Figure 23b) was estimated as 1.3 mm; its actual value varied from 1.1 to 1.8 mm along the crack front, due to a non-uniform crack front advance at different parts of the specimen.

The corrosion-assisted fracture developed inside the specimen, without extending towards the specimen sides. The observed SCC mechanisms are presented in Figures 39c–l. The most characteristic features of the fracture surface of SCC tested CT specimen are SCC striations. This is, probably, an indication of the fact that SCC crack growth occurs by localized anodic dissolution (via the FRAD mechanism). A necessary condition for the SCC occurrence by this mechanism is creep of the material near the crack tip, which causes ruptures of the passivating film (Figure 29).

## 4.4 Stress intensity factor and *J*-integral at typical kinetic stages of SCC of MT panel and CT specimens

The estimates of stress intensity factor and of *J*-integral for MT panel specimens (Table 2) were obtained using the values of load and displacement that corresponded to the two SCC stages, as discriminated by the AE. The average values, as well as the mean-square deviations from average, were estimated for $K_I$ (using 10 specimens) and $J_I$-integral (using 5 specimens, No 6–10 in Tables 1 and 2).

For CT specimens under a static SCC test at a fixed crack opening, δ = 0.3 mm, the initial value of the stress intensity factor was equal to $K_I = 27$ MPa·√m. During the crack growth (1.3 mm, on average, during 1,400 hours of the static SCC test) the stress intensity factor value decreased to $K_I = 25.6$ MPa·√m. In the tensile test performed on the pre-embrittled CT specimen (Figure 21), the first (initiation) kinetic stage of fracture was observed at a stress intensity factor of $K_I = 28.2$ MPa·√m. Estimates of stress intensity factor at the second stage of fracture kinetics (developed plastic deformation) were not performed. Fracture resistance of the CT specimen was evaluated using the energy criterion, *J*-integral. The following estimates were obtained, $J_I = 98.3$ kJ/m$^2$ and $J_I = 380.4$ kJ/m$^2$, for the first and the second kinetic stages of fracture, respectively.

**Table 2. Estimates of copper resistance to SCC.**

| Specimen number | SCC initiation stage | | SCC macrofracture stage | |
|---|---|---|---|---|
| | $K_{1C}$, MPa·√m | *J*-integral (calculated form the work of deformation of the whole specimen), kJ/m$^2$ | $K_{1C}$, MPa·√m | *J*-integral (calculated from the work of deformation of the whole specimen), kJ/m$^2$ |
| 1 | 11.2 | – | 30.8 | – |
| 2 | 12.1 | – | 25.3 | – |
| 3 | 13.5 | – | 24.0 | – |
| 4 | 9.9 | – | 34.3 | – |
| 5 | 11.0 | – | 24.1 | – |
| 6 | 8.3 | 123 | 32.7 | 560 |
| 7 | 10.1 | 126 | 30.6 | 597 |
| 8 | 11.0 | 75.9 | 31.6 | 588 |
| 9 | 6.6 | 103 | 30.4 | 588 |
| 10 | 11.3 | 145.2 | 29.2 | 557 |
| Average value ± dispersion of average | 10.5 ± 0.6 | 114.6 ± 11.7 | 29.3±1.2 | 578 ± 8.1 |

# 5 Summary of the obtained results

The present study of stress-corrosion cracking of copper in 0.1M $NaNO_2$ aqueous solution included:

1. Monitoring of the fracture kinetics by means of registering the acoustic emission signals (Section 3.2).
2. Investigation of the fracture mechanisms using macro- and micro-fractographic analyses (Section 3.4).
3. Obtaining quantitative estimates of the cracking resistance of the material, at different stages of SCC kinetics, using the parameters of linear (stress intensity factor, $K_I$, Section 3.3.1) and non-linear ($J$-integral as determined within the measuring procedure by Begley and Landes, Section 3.3.2) fracture mechanics.

Two kinds of SCC tests (Section 3.1) under continuous circulation of the corrosive solution were performed in the present study:

1. Constant extension rate ($2 \cdot 10^{-6}$ $s^{-1}$) tests on pre-cracked, middle tension panel specimens. The time base for these tests was 17–24 hours.
2. Tests on pre-cracked, compact tension specimens at a fixed opening of the crack walls. The time base for these tests was about 1,400 hours.

According to the results of AE measurements during the time of tests (17–24 hours and 1,400 hours for MT and CT specimens, respectively) the kinetics of stress-corrosion cracking has two stages. For a CT specimen, regular AE pulses of amplitude $V_P$ = 6–15 dB above the noise level were first registered after 200 hours of test. The pulses of 'burst' acoustic emission with $V_P$ = 15–20 dB were registered after about 800 hours of test (Figure 19e).

For MT specimen under continuous loading conditions the initiation of stress-corrosion cracking was detected, by acoustic emission, after 3–4 hours of test; the deformation and the load of the specimen were $f$ = 1.5–2.5 mm and $P$ = 9–17 kN, respectively (see Figure 20 and Table 1). The second stage of SCC kinetics, characterized by strong pulses of 'burst' acoustic emission of amplitude $V_P$ = 40–55 dB, was observed after 5–10 hours in these tests, (at $f$ = 4–6 mm and $P$ = 28–60 kN, see Figure 20 and Table 1).

AE-based diagnostics of fracture, aimed at revealing the process kinetics, includes discrimination of signals (for instance, those that exceed the noise level) as well as monitoring the changes in the emission character (such as, for instance, occurrence of strong pulses of 'burst' AE, see Figure 20).

’Continuous’ emission of small amplitude (but of high intensity), which accompanies micro-cracking during the fracture process, is registered during both the first and the second SCC stages (see Figures 16a,b, 18a, and 20). Falls and rises of the AE power (Figure 20) reflect, most likely, the discontinuity of the stress-corrosion cracking process – its extinction and re-activation /18–20/. After detection of strong AE pulses, which manifest the beginning of the second stage of SCC, the fracture may develop either by micro-cracking (accompanied by small-amplitude AE signals, see Figure 18a) or by formation of large zones of fracture (Figure 18b).

The acoustic emission level during slow-rate ($2\cdot10^{-6}$ $s^{-1}$) straining of center cracked panel (middle tension) specimens in air is only slightly above the noise level, as usual for slowly strained ductile materials. The fracture surface of the specimens pulled in air exhibits a smooth 'stretch zone' of a plastic advance of the crack, which is typical for fatigue pre-cracked specimens of ductile materials (Figure 24). The stretch zone is formed by the action of shear stresses (Figure 24a) that 'split' the material along the slip planes that have been 'prepared' by the preceding plastic deformation /10/. In the absence of corrosion the stretch zone is followed by the zone of usual ductile fracture of copper (Figure 27).

According to the fractography of SCC tested MT panel specimens, the zone of corrosion-assisted fracture (Figures 25–37) extends to approximately 1,500 µm. Microfractographic analysis has revealed a 400–700 µm deep zone of brittle transgranular fracture. This zone is adjacent to the fatigue pre-crack front. Areas of brittle transgranular fracture having several different surface morphologies were observed (see Figures 25 and 26); the variation of the surface morphology may indicate that different micro-mechanisms of fracture are operative in different areas. The mechanisms of brittle fracture during SCC in copper, as well as in other ductile materials, have been discussed in the literature /12, 15–17, 21–23/. In particular, dislocation models of corrosion-assisted fracture have been discussed in the framework of electrochemical approach to SCC. These models assume that a planar configuration of dislocations may cause transgranular fracture (along cleavage planes) under the conditions of plastic deformation /22/. Such cleavage along several parallel planes (probably caused by a number of apparently coplanar micro-cracks, see Figure 25c) is shown in Figure 25a. The 'wavy' appearance of the fracture surface in Figure 25a was probably caused by the slip lines that had developed at the stage of plastic deformation that preceded fracture /15, 16/. We also observed brittle trans-granular fracture along non-coplanar (crossing) slip planes (Figure 25b), as well as 'chevron' fracture (Figure 25e). Previously reported /23/ cleavage steps were also observed in the present study (Figures 25i–l). Cleavage steps are thought to form during a relatively long-term arrest, followed by re-initiation, of the SCC crack front. Some features of the fracture surface, such as the apparent change of the corrosion-assisted fracture mechanism as well as the etching of material (Figure 25l) and the secondary cracks observed at the bottom of the cleavage step (Figure 25b), are consistent with this point of view. The specimens that exhibited high-amplitude ($V_P$ = 20–30 dB , Figure 20a) pulses of 'burst' AE at the first stage of SCC kinetics were also found to exhibited areas of brittle transgranular fracture (cleavage), immediately adjacent to the fatigue pre-crack zone, on their fracture surfaces (Figures 26, 32). Areas of brittle fracture of copper were also observed at later stages of the specimen fracture (Figures 35b,c,d) and may be correlated with the pulses of 'burst' AE of high amplitude, $V_P$ = 25–50 dB (Figure 20). At the last stage of slow-strain rate tests on MT plate specimens the usual ductile fracture of copper is found to occur, without visible signs of corrosion damage.

A similar sequence of fracture mechanisms was observed in a previous study /24/ on cylindrical (2.5 mm in diameter) 99.9% and 99.99% copper specimens strained at a constant rate of $10^{-6}$ $s^{-1}$ in 1M $NaNO_2$ aqueous solution. Transgranular cracks, which developed (possibly /25/ already at the stage of uniform deformation, at a stress level of $\sigma \cong 160$ MPa) from the specimen surface, were found to decrease the yield stress and to lower the ductility limit (characterized using the strain-to-failure parameter) from 45% (copper in air) to 20% (copper in $NaNO_2$ solution). However, the ring-shaped zone of brittle fracture (500–800 µm in depth) was immediately followed by the ductile fracture zone in the published fractograms /24/. The fracture surface of MT plate specimens tested in the present work exhibits a transition zone of stress-corrosion cracking, which lies between the zones of brittle and ductile fracture (Figure 37b, crack propagation from bottom to top).

As has been discussed /1/ the corrosion-assisted fracture of continuously strained copper specimens may be initiated by rupture of the surface (oxide) film at the exit of active slip planes. The SCC mechanism that considers film rupture due to localized plastic flow is well known (Figure 29). The opened areas of unprotected metal may undergo rapid anodic dissolution. Zones showing characteristic SCC 'striations' have been found on fracture surfaces in the present study (see Figure 28). The width of a striation varies in the interval 0.75–1.4 µm. Transitions from a zone of brittle transgranular cleavage to a zone with SCC striations have also been observed (see Figure 28a).

However, on some fracture surfaces we found areas where the crack propagation plane changed every 15–20 µm (see Figure 34, crack propagation direction from top to bottom). It is difficult to explain the formation of such areas, showing alternating crack propagation planes, merely on the grounds of localized plastic flow /15, 16/. One possible explanation is that the change of the crack trajectory is caused by the internal grain structure, for instance, by sheets of annealing twins (their presence in the structure is illustrated by Figure 1a,b). It is known, for instance, that the difference in electrochemical properties between differently oriented grains leads to a non-uniform etching of copper sheets having rolling textures.

The mechanism of corrosion-assisted fracture changes as a function of distance from the fatigue pre-crack front. The fracture surface begins to loose its distinct topographic features (see Figure 30). The smearing of the surface morphology may be a result of the evolving strain hardening of copper by multiple dislocation glide activity within the four non-coplanar families of {111} planes in the FCC crystal structure /26/. In the following, corrosion-assisted fracture propagates within 'lobes' (see Figure 31) having a characteristic dark appearance, due to a tarnish film of corrosion products (Figure 32, crack propagation direction from top to bottom). The fracture surface in this zone contains areas of both transgranular (Figure 31d) and intergranular (Figure 31b,c) fracture. Although the strong etching of the surface makes it difficult to identify the fracture type within this zone, the fracture seems to be mostly transgranular – no substantial changes of the crack trajectory are observed (Figure 31c). The dark color of the fracture surface, produced by this SCC mechanism, may already be seen at an optical magnification. SCC 'lobes' are different in color from the surface of fatigue pre-crack zone, from the surfaces in the areas of brittle and intermittent (with 'striations') fracture, as well as from the surface of ductile fracture that was formed when the specimen was pulled apart after completion of the test. It is noteworthy that the fracture surface in the fatigue pre-crack area neither changed its color nor contained signs of active etching/dissolution during the whole time of its exposure to the $NaNO_2$ solution (see Figures 1d and 6). The specific color and surface morphology of the SCC lobes, as well as noticeable surface etching, may indicate that specific electrochemical conditions existed within this narrow SCC zone (Figures 31, 32). For instance, this zone might have a different steady-state potential of the metal, so that an electrochemical macro-couple might have formed between the crack mouth and open surfaces such as the crack walls. Also, the evolution of SCC is usually sensitive to changes of the stress state – the corrosion front is narrowed due to the development of plastic deformation (Figure 32).

Non-uniformity of corrosion assisted fracture can also be seen on AE diagrams, both at the first and at the second kinetic stages of SCC. 'Continuous' acoustic emission accompanying microfracture events (at the level of $V_P$ = 9–12 dB) may slowly decay, within periods of 1–2 hours, Figure 16a,b) reflecting a slow down or a temporary stop in the stress-corrosion cracking process.

The SCC crack may advance by several 'lobes' (as in Figures 31a and 26c, crack propagation direction from top to bottom in both figures) leaving ligaments of unfractured material between them (Figure 33). The ligaments are typical elements of the studied fracture surfaces. Our fractographic analysis has revealed that, under continuous straining of the specimen, the ligaments may fail either by ductile rupture (Figure 34) or by brittle cleavage (transgranular fracture in Figure 35, crack propagation from top to bottom). Because of its high velocity, the brittle cleavage produces pulses of 'burst' AE /25/, which appear on the AE diagrams on the background of decaying 'continuous' acoustic emission ($V_P$ = 20–30 dB, Figure 16a,b).

At the transition to a plastic opening of the crack, the SCC front becomes discontinuous. Corrosion-assisted fracture develops by 'patches', which form steps on the fracture surface (Figure 37). This macro- and micro- inhomogeneity of the fracture process is reflected in the acoustic emission – the signals of both 'burst' and 'continuous' AE are detected (Figure 20). Further development of plastic deformation suppresses the stress-corrosion cracking processes.

At the beginning of every kinetic stage of SCC of panel specimens, the crack resistance parameters were estimated using a joint analysis of the AE diagrams and of the mechanical 'load-displacement' diagrams (Figure 20). The results of the estimates of $K_I$ (using a series of 10 MT panel specimens, see Section 3.3.1) and of $J$-integral (using a series of 5 MT panel specimens, see Section 3.3.2) are summarized in Table 2. For the beginning of the first kinetic stage of SCC (see Figure 20 and Table 2) the following estimates were obtained: $K_I = 10.5 \pm 0.6$ MPa·√m, $J_I = 114.6 \pm 11.7$ kJ/m$^2$. For the beginning of the second kinetic stage the corresponding estimates were $K_I = 29.3 \pm 1.2$ MPa·√m, $J_I = 578 \pm 8.1$ kJ/m$^2$.

The average crack growth length in the CT specimen was about 1.3 mm during 1,200 hours of corrosion-assisted fracture (the total time of the static SCC test was 1,400 hours, including an incubation period of 200 hours determined by AE, see Figure 19d), at the initial stress intensity factor level $K_I$ = 27 MPa·√m and the final level $K_I$ = 25.6 MPa·√m. The estimated average crack growth rate was $3 \cdot 10^{-7}$ mm/s, which is somewhat higher than that obtained in Ref /1/ for the same level of the stress intensity factor. The difference may be probably attributed to an accelerated kinetics of SCC due to the continuous pumping of the corrosive solution used in the present study. In order to check whether the long-term (1,400 hours) exposure to the corrosive solution had any after-effect on the mechanical properties of copper, the CT specimen was additionally tensile tested (off-center loading, strain rate 0.02 mm/s) immediately after the static SCC test. Test geometry, recorded AE diagram, and the joint (using time-markings) $P$-$f$ and AE diagrams are shown in Figure 21. The fracture kinetics, monitored using AE, shows two characteristic stages (Figure 21b,c). The first rise of the acoustic signal, which is found to occur at $K_I$ = 28.2 MPa·√m (Equation (3)) and $J_I$ = 98.3 kJ/m$^2$ (Equation (5), Figure 21c), is probably caused by the multiple microfracture events along the crack front. The second stage of the fracture kinetics ($J_I$ = 380.4 kJ/m$^2$) may be attributed to the development of relatively large areas of active fracture, as a result of straightening of the crack front by means of, for instance, rupture of internal and side ligaments. As soon as all the pre-embrittled material has been fractured, the crack advance stops, and the AE signal level falls off (Figure 21b,c). The fracture surface has the usual appearance produced by ductile fracture. The acoustic emission was not monitored when the specimen was further loaded in the region of fully ductile fracture. The $J$-integral values obtained during the additional test on the CT specimen are close to the estimates obtained for the corresponding stages of the SCC fracture kinetics (micro- and macro-fracture) of panel MT specimens (see Figure 20 and Table 1). The estimate of the stress intensity factor for the first stage of fracture kinetics, $K_I$ = 28.2 MPa·√m, has been obtained on the CT specimen under the conditions of a transition to plastic deformation (which may be seen from the load-displacement diagram, Figure 21). Therefore, the derived value may require more accurate determination.

Acoustic emission is often the only technique that offers sufficient sensitivity for in situ monitoring of fracture events on the microstructure level. In this connection, the following important issues questions should be addressed: (i) Relationship between the results of observations and the physics of the monitored process, and (ii) Reliability of the derived quantitative estimates. AE monitoring allows us to distinguish two stages in the SCC kinetics. Two-stage behavior is often found for corrosion-assisted fracture processes /18–20/. The first stage, *SCC initiation*, begins after a certain 'incubation time', during which no detectable corrosion damage occurs. The duration of the 'incubation time' depends on the character of detected signals. For instance, the relatively 'crude' method of visual detection of the SCC crack growth may be opposed to the AE-based method that allows one to reliably detect the signal induced by a formation of a 10 μm deep cleavage facet /25/. Since the first acoustic signals from micro-fracture events in the material are detected, it takes some additional time before the second stage, *active development of stress-corrosion sites*, begins /19/. This transition is often associated with a change in the fracture mechanism (for instance, the transition from the crack growth mode by small micro-fracture events to the macro-crack growth mode may be considered as the beginning of the second stage of SCC).

In order to assess the reliability of quantitative estimates related to fracture, it is preferable to make a direct comparison of the AE signal with the corresponding fracture area /25/. In practice of SCC studies, however, these estimates are difficult to obtain /19/, especially at early stages of the SCC processes. In such cases, the statistical reproducibility of the obtained estimates (for fixed experimental conditions and test geometry) may be used as a criterion of reliability. Corrosion processes are usually difficult to reproduce, which is why one needs extended statistics for measurements of this kind. Therefore, the relatively low values of dispersion of average, obtained in the present study (see Table 2) for the fracture resistance parameters at both kinetic stages of SCC, were somewhat unexpected. The average values of the fracture resistance parameter $K_I$ for the first and second stages of SCC were found to be close to the lower and upper bounds, respectively, of the $K_{ISCC}$ estimates (16–30 MPa·√m) obtained in several previous studies /3/. As it has been mentioned above, the lower bound of this interval may depend on the sensitivity of the applied measuring technique. The effect of strain hardening of the material near the tip of the fatigue-generated pre-crack should also be taken into account. It has been shown /27/ that strain hardening decreases the fracture resistance of copper; the fact that cold-worked alloys show an increased susceptibility to SCC is also well known.

# 6 Conclusions

1. In both kinds of SCC tests, performed in the present study on pre-cracked copper specimens in 0.1M $NaNO_2$ aqueous solution, two kinetic stages of the SCC process have been revealed using acoustic emission measurements:
    - SCC initiation stage begins after a certain incubation time (3–4 hours for constant extension rate tests on MT panel specimens or after 200 hours for test on CT specimens at a fixed opening of the fatigue pre-crack). At this stage the crack advances by small steps; the amplitude of AE pulses is $V_P = 6–15$ dB above the noise level, for both kinds of tests.
    - SCC macro-fracture stage begins after 8 hours of test on an MT panel specimen or after 800 hours of test on a CT specimen. At this stage an active development of relatively large stress-corrosion sites takes place, which is accompanied by high-amplitude AE pulses, up to $V_P = 50$ dB for MT panel specimen and $V_P = 15–20$ dB for CT specimen.
2. The surfaces of fractured MT panel specimens show a 1,500 μm deep zone of SCC fracture, followed by a zone of usual ductile fracture. The development of plastic deformation is found, first, to narrow the SCC front and, then, to completely suppress SCC. A similar influence of plastic deformation (near the tip of the fatigue pre-crack and/or near the side grooves) may be a cause of the poor reproducibility of SCC in copper that was found in some experimental studies.
3. Macro-fractographic studies show that corrosion-assisted fracture of copper in 0.1M $NaNO_2$ aqueous solution, at a slow-rate ($2 \cdot 10^{-6}$ $s^{-1}$) straining of MT panel specimens, occurs according to two main mechanisms:
    - Brittle transgranular SCC. The corresponding fracture zone is 400–700 μm deep and is adjacent to the fatigue pre-crack zone.
    - Corrosion-assisted fracture, localized within ‘patches’ or ‘lobes’. These SCC ‘lobes’ have a rough surface morphology and a characteristic dark color (probably, due to a tarnish film of corrosion products).

    The observed different SCC mechanisms in copper may imply different rates of SCC.
4. Microfractography reveals that transgranular fracture may produce different surface morphologies, depending on the operating micro-mechanisms of SCC. In the present study, the following surface morphologies have been observed:
    - crystallofraphically oriented areas of transgranular cleavage along several parallel planes (with some traces of preceding plastic deformation also being present),
    - fracture on non-coplanar planes,
    - ‘chevron’ morphology of fracture,
    - non-crystallographic transgranular fracture,
    - areas of brittle fracture within the SCC ‘lobes’ or ‘patches’ that form at a late stage of SCC evolution.
5. The observed fracture type of the CT specimen is mostly transgranular. SCC striations are typically observed on the fracture surface.

6. The average crack growth length in the CT specimen was about 1.3 mm during 1,200 hours of corrosion-assisted fracture (the total time of the static SCC test was 1,400 hours, including an incubation period of 200 hours determined by AE, see Figure 19d), at the initial stress intensity factor level $K_I = 27$ MPa·√m and the final level $K_I = 25.6$ MPa·√m. The estimated average crack growth rate was $3 \cdot 10^{-7}$ mm/s, which is somewhat higher than that obtained in Ref /1/ for the same level of the stress intensity factor. The difference may be probably attributed to an accelerated kinetics of SCC due to the continuous pumping of the corrosive solution through the crack.

7. Fracture resistance parameters were estimated, at the beginning of every kinetic stage of SCC of panel specimens, using a joint analysis of the AE diagrams and of the mechanical 'load-displacement' diagrams. For the beginning of the first kinetic stage of SCC (see Figure 20 and Table 2) the following estimates were obtained: $K_I = 10.5 \pm 0.6$ MPa·√m, $J_I = 114.6 \pm 11.7$ kJ/m$^2$. For the beginning of the second kinetic stage the corresponding estimates were $K_I = 29.3 \pm 1.2$ MPa·√m, $J_I = 578 \pm 8.1$ kJ/m$^2$. The *J*-integral values obtained during the additional test on the CT specimen, $J_I = 98.3$ kJ/m$^2$ and $J_I = 380.4$ kJ/m$^2$, are close to the estimates obtained for the corresponding stages of the SCC fracture kinetics (micro- and macro-fracture) of panel MT specimens. The estimated stress intensity factor for the first stage of fracture kinetics of the CT specimen was $K_I = 28.2$ MPa·√m. The fact that different estimates of the fracture resistance of copper can be derived for the two kinetic stages of SCC may explain the scatter of fracture resistance estimates that is found in the literature. Also, the effect of specimen pre-history (strain hardening of the material near the fatigue pre-crack tip, during the specimen preparation) may require more careful analysis.

# 7 Acknowledgements

This study was entirely funded by SKB, the Swedish Nuclear Fuel and Waste Management Company. The authors wish to express their gratitude to S G Khanzhin (Head of Defectoscopy Division, Laboratory of Metals, Konakovo Power Station, Konakovo, Russia) for his help in conducting tests and for many fruitful discussions. Fatigue pre-crack generation part of the specimen preparation was done in collaboration with A G Mazepa (Head of Fatigue Testing Laboratory, CNIITMASH, Moscow, Russia). Alexander Arsenkin (PhD student, MISiS, Moscow) is acknowledged for his assistance in the fractography studies. L O Werme (SKB, Stockholm) and P A Korzhavyi (KTH, Stockholm) are acknowledged for stimulating discussions and useful comments.

# References

1 **Pettersson K, Oskarsson M, 1997.** A study of stress corrosion crack growth in copper for nuclear waste canister application, Preprint TRITA-MAC-0611, Royal Institute of Technology (KTH), Stockholm.

2 **Saario T, Laitinen T, Mäkelä K, Bojnov M, 1999.** Literature survey on stress-corrosion cracking of Cu in presence of nitrites, ammonia, carbonates and acetates, Working Report 99-57, POSIVA OY, Helsinki.

3 **Rosborg B, Werme L, 2001.** The Resistance of Pure Copper to Stress Corrosion Cracking in Repository Environments, SKB TR-01-25, Svensk Kärnsbranslehantering AB.

4 **King F, Ahonen L, Taxén C, Vuorinen U, Werme L, 2001.** Copper corrosion under expected conditions in a deep geological repository, SKB TR-01-23, Svensk Kärnsbranslehantering AB.

5 **Feddersen C E, 1967.** Discussion to: Okabe Strain Crack Toughness Testing of Metallic Materials, ASTM STP 410, 77.

6 **Blumenauer H, 1978.** Werkstoffprüfung, (Deutscher Vld f. Grundstoffindustrie, Leipzig), 426 pp.

7 **Rice J R, 1968.** A path independent integral and approximate analysis of strain concentration by notches and cracks. J. Appl. Mech. Ser. E 35, 379.

8 **Begley J A, Landes J D, 1972.** The J-integral as a fracture criterion. In: Fracture Toughness, Part II, ASTM STP 514, 1.

9 **Clarke G A, Landes J D, 1979.** Evaluation of the J-integral for the compact specimen, Journal of Testing and Evaluation, JTEVA, Vol 7, No 5, pp 264–269.

10 **Pelloux R M N, 1970.** Crack Extension by Alternating Shear, Engineering Fracture Mechanics 1, 697.

11 **Jagrelius-Pettersson R F A, 2001.** Applications of acoustic emission in corrosion research – a literature survey, Research Report IM-2001-017, Swedish Institute for Metals Research, Stockholm.

12 **Flanagan W F, Lichter B D, 1996.** A mechanism for transgranular stress-corrosion cracking, Intl. J. of Fracture 79, 121.

13 **Hertzberg R W, 1976.** Deformation and fracture mechanics of engineering materials, (John Wiley & Sons, New York).

14 **Bridgman P W, 1952.** Studies in large plastic flow and fracture, in Metallurgy and Metallurgical Engineering series, edited by R F Mehl (McGraw-Hill Book Company, Inc, New York).

15 **Lian K, Meletis E I, 1996.** Environment-induced deformation localization during transgranular stress corrosion cracking, Corrosion 52, 347. (Fig 1 on p 349 and Fig 9 on p 354).

16 **Meletis E I, Lian K, 1996.** Deformation evolution during initiation of transgranular stress corrosion cracking, Intl. J. of Fracture 79, 165. (Fig 10 on p 175).

17 **Magnin T, Chambreuil A, Chateau P, 1996.** Stress corrosion cracking mechanisms in ductile FCC materials, Intl. J. of Fracture 79, 147. (Fig 3 on p 150).

18 **GerberichW W, Jones R H, Friesel M A, Nozue A, 1988.** Acoustic emission monitoring of stress corrosion cracking, Mater. Sci. & Eng. A 103, 2357.

19 **Nikulin S A, Khanzhin V G, Kurianova E Y, Markelov A P, 1997.** Acoustic emission technology for quantitative monitoring stress corrosion cracking in materials, Proceedings of the 5th European Conference on Advanced Materials – Processes and Application, (Maastricht, NL), pp 238–241.

20 **Chatterjee U K, Sircar S C, Agrawal G S, 1984.** Acoustic emission studies on environmental cracking in brasses, in Advances in Fracture Research (Fracture 84), Proceedings of the 6th International Conference on Fracture (Pergamon, Oxford), pp 2,379–2,385.

21 **Sieradzki K, Newman R C, 1985.** Brittle behaviour of ductile metals during stress-corrosion cracking, Phil. Mag. A 51, 95.

22 **Swann P R, Pickering H W, 1963**. Implications of the stress aging yield phenomenon with regard to stress corrosion cracking, Corrosion 19, 369.

23 **Sieradzki K, Sabatini R L, Newman R C, 1984.** Stress-corrosion cracking of copper single crystals, Metal. Trans. A 15, 1941.

24 **Pednekar S P, Agrawal A K, Chaung H E, Staehle R W, 1979.** Transgranular cracking of copper in 1M $NaNO_2$ solution, J. Electrochem. Soc. 126, 701.

25 **Nikulin S A, Shtremel M A, Khanzhin V G, Kurianova E Y, Markelov A P, 1999.** Analysis of fracture scale and material quality monitoring with the help of acoustic emission measurements, Acoustic Emission Standards and Technology Update, ASTM STP 1353, 125.

26 **Cho J W, Jin Yu, 1991.** Near-crack-tip deformation in copper single crystals, Phil. Mag. Letters 64, 175.

27 **Pardoen T, Scibetta M, Chaouadi R, Delannay F, 2000.** Analysis of the geometry dependence of fracture toughness at cracking initiation by comparison of circumferentially cracked round bars and SENB tests on copper, Intl. J. of Fracture 103, 205.

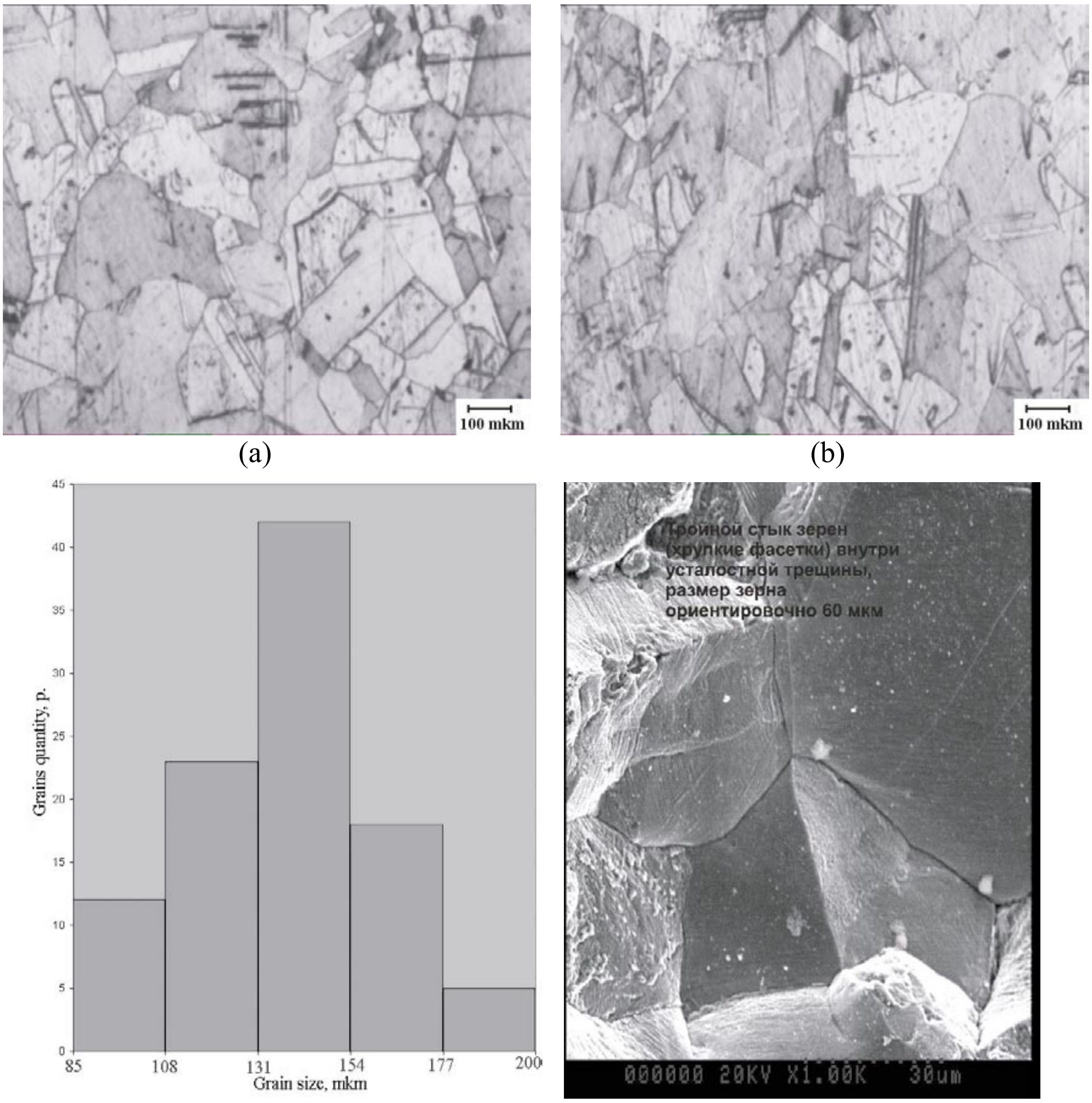

(a) (b)

(c) (d)

***Figure 1.*** *Grain structure of the studied material.*
*a, b – grain structure micrographs for two polished sections of a copper specimen;*
*c – diagram of the grain size distribution in the copper material;*
*d – triple joint of copper grains at the fracture surface within the fatigue pre-crack area.*

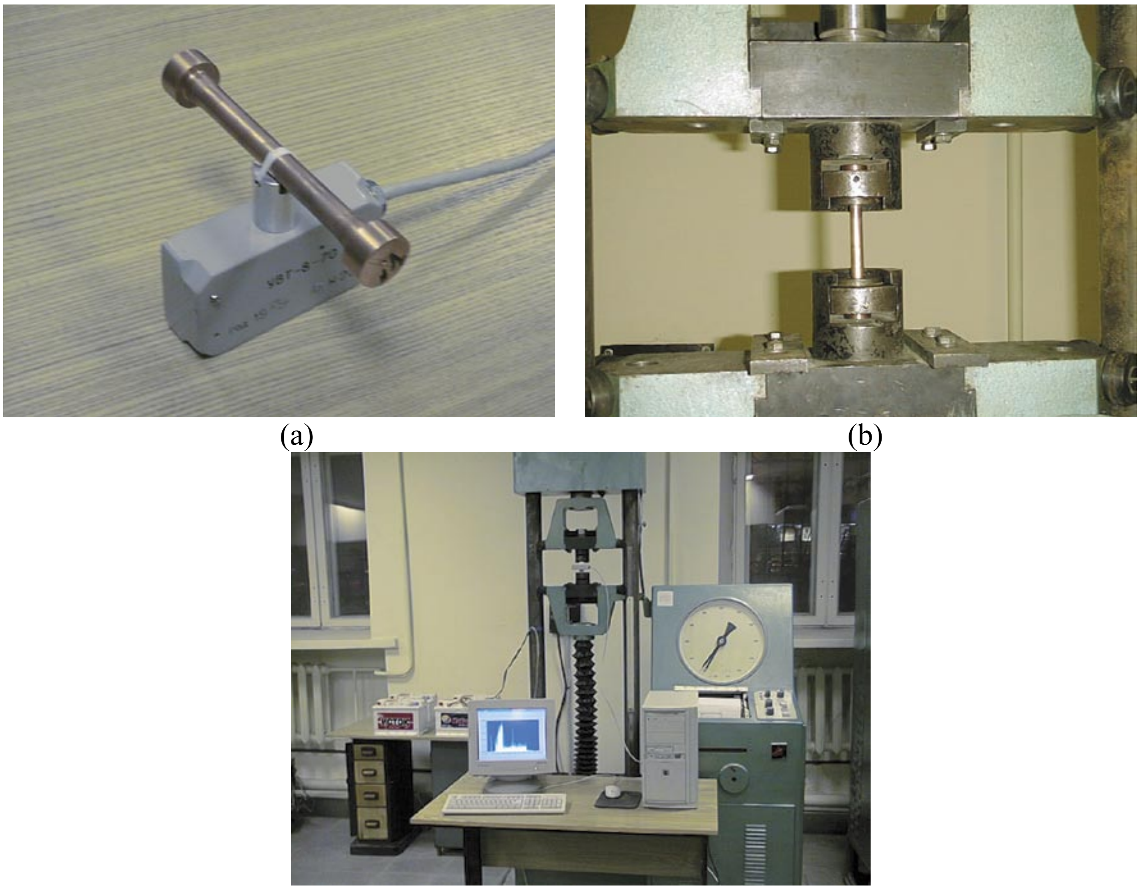

(a) (b)

(c)

*Figure 2. Specimens for mechanical tests.*
*a – cylindrical 'fivefold' specimen for tensile tests;*
*b, c – specimen mounted in the grips of a testing machine.*

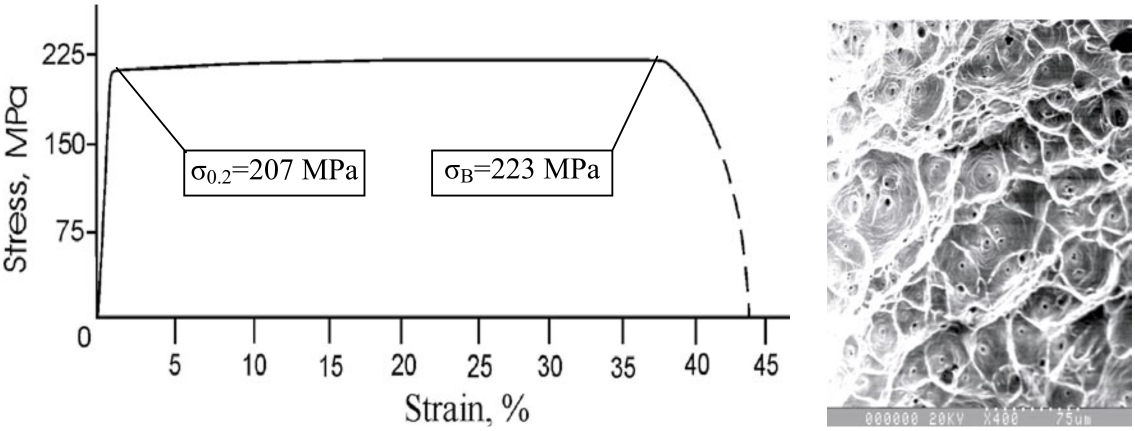

(a) (b)

*Figure 3. Tensile test on cylindrical copper specimens.*
*a – schematic deformation diagram of a tensile tested copper specimen;*
*b – fracture surface of a copper specimen tested in air.*

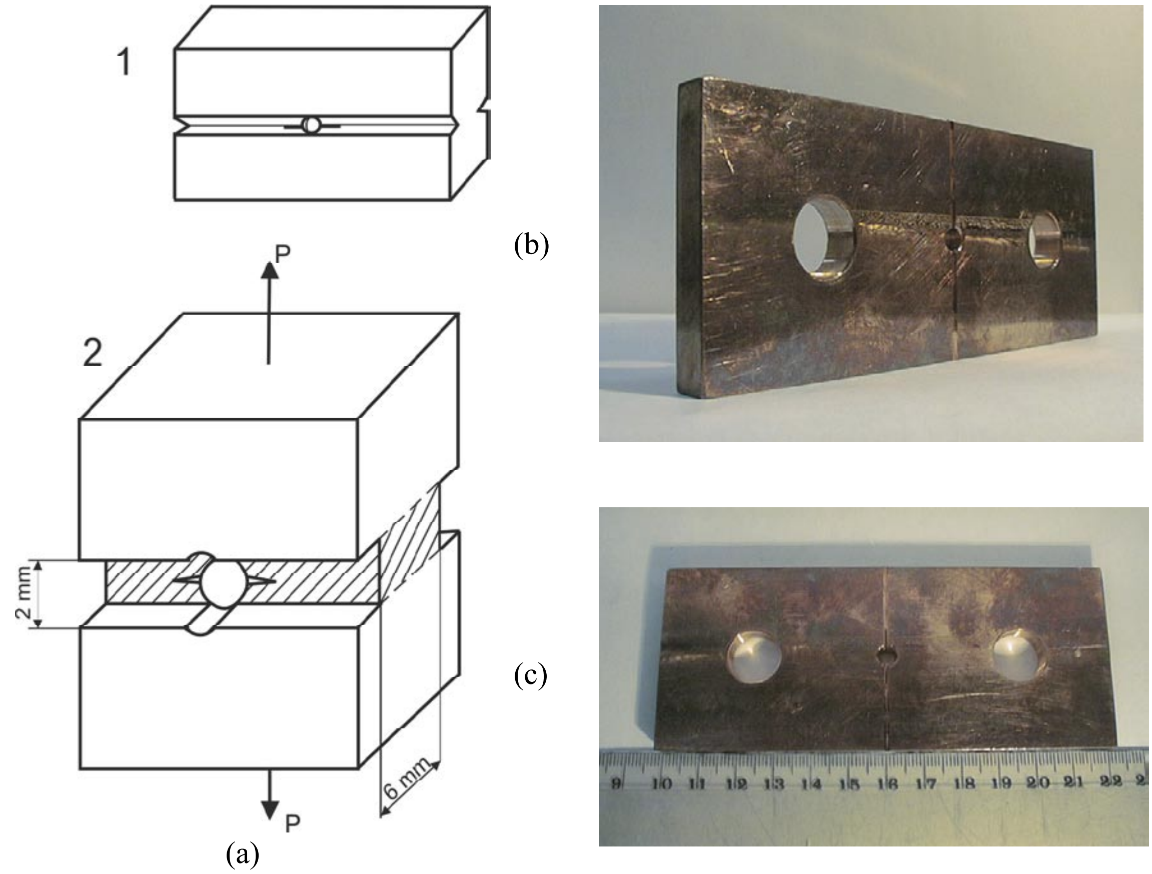

***Figure 4.*** *MT panel specimen for SCC tests.*
*a, b, c – schematic drawing and two photos of an MT panel specimen.*

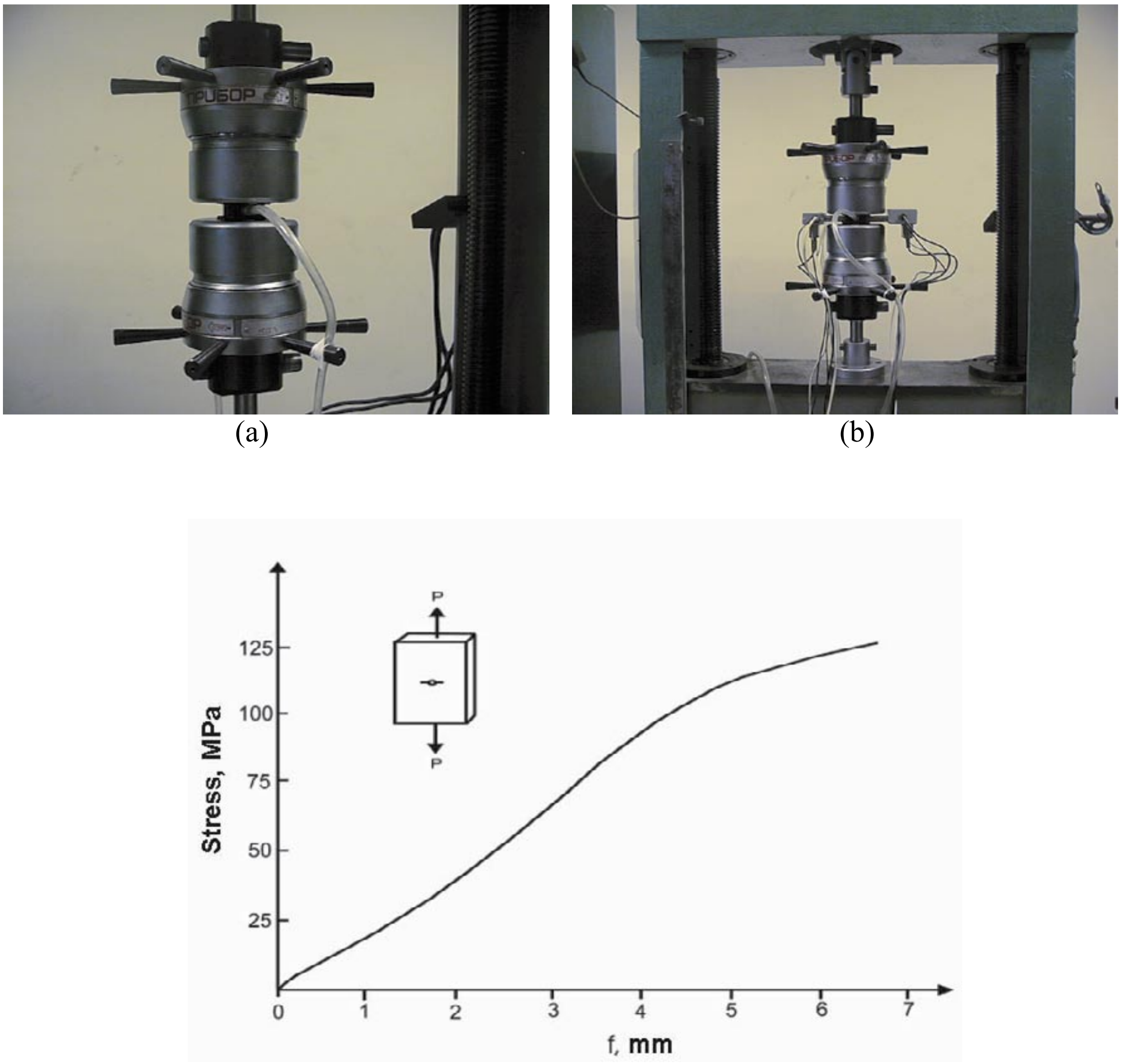

(a) (b)

(c)

***Figure 5.*** *SCC tests on MT panel specimens.*
*a, b – MT panel specimen mounted in the grips of the testing machine;*
*c – deformation diagram of a tensile test on an MT panel specimen.*

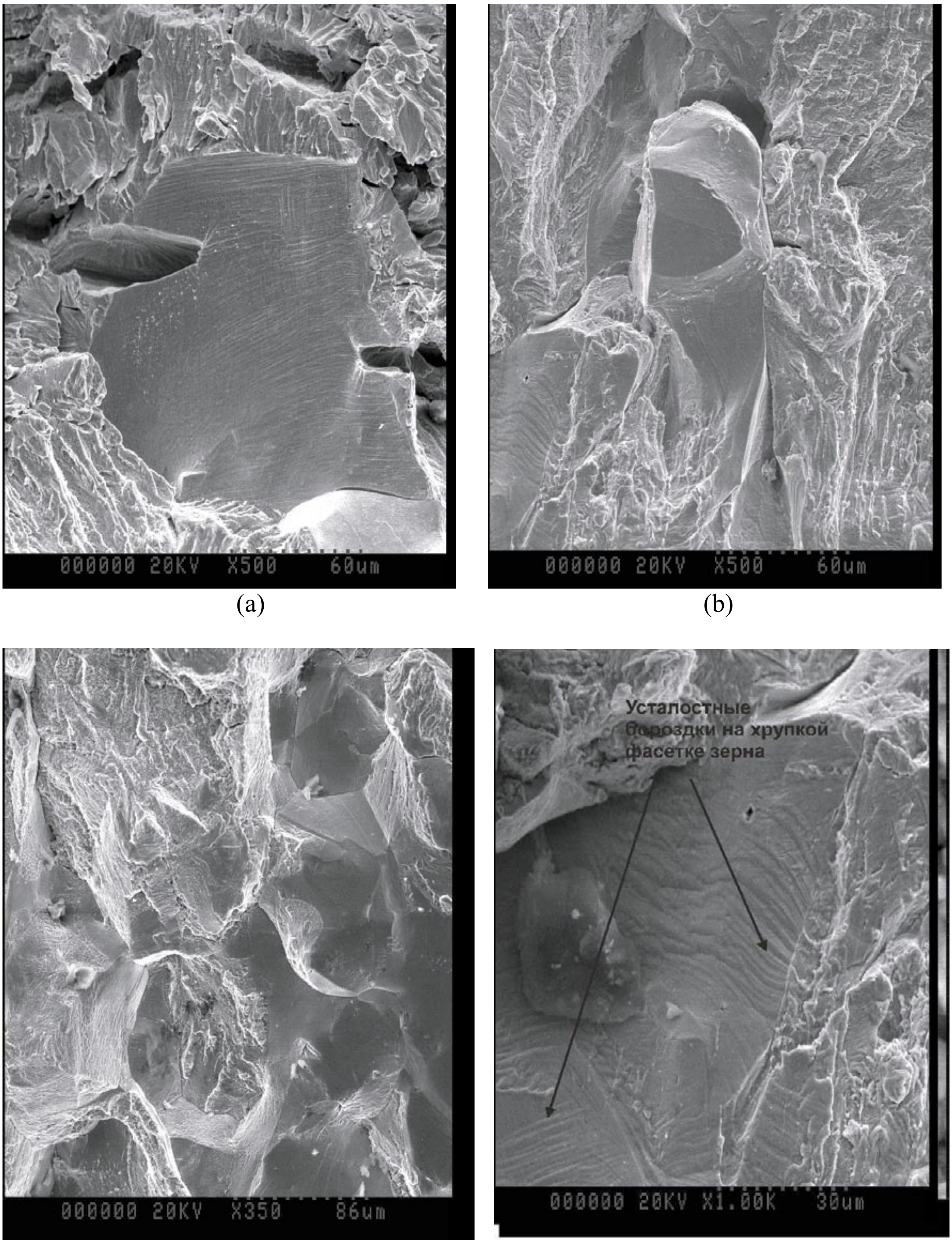

(a) (b)

(c) (d)

***Figure 6.*** *Surface fractography of the fatigue-generated pre-crack.*
*a – grain-boundary facet with internal transgranular cracks;*
*b, c – mixed trans- and inter-granular fracture;*
*d – grain facet with fatigue grooves.*

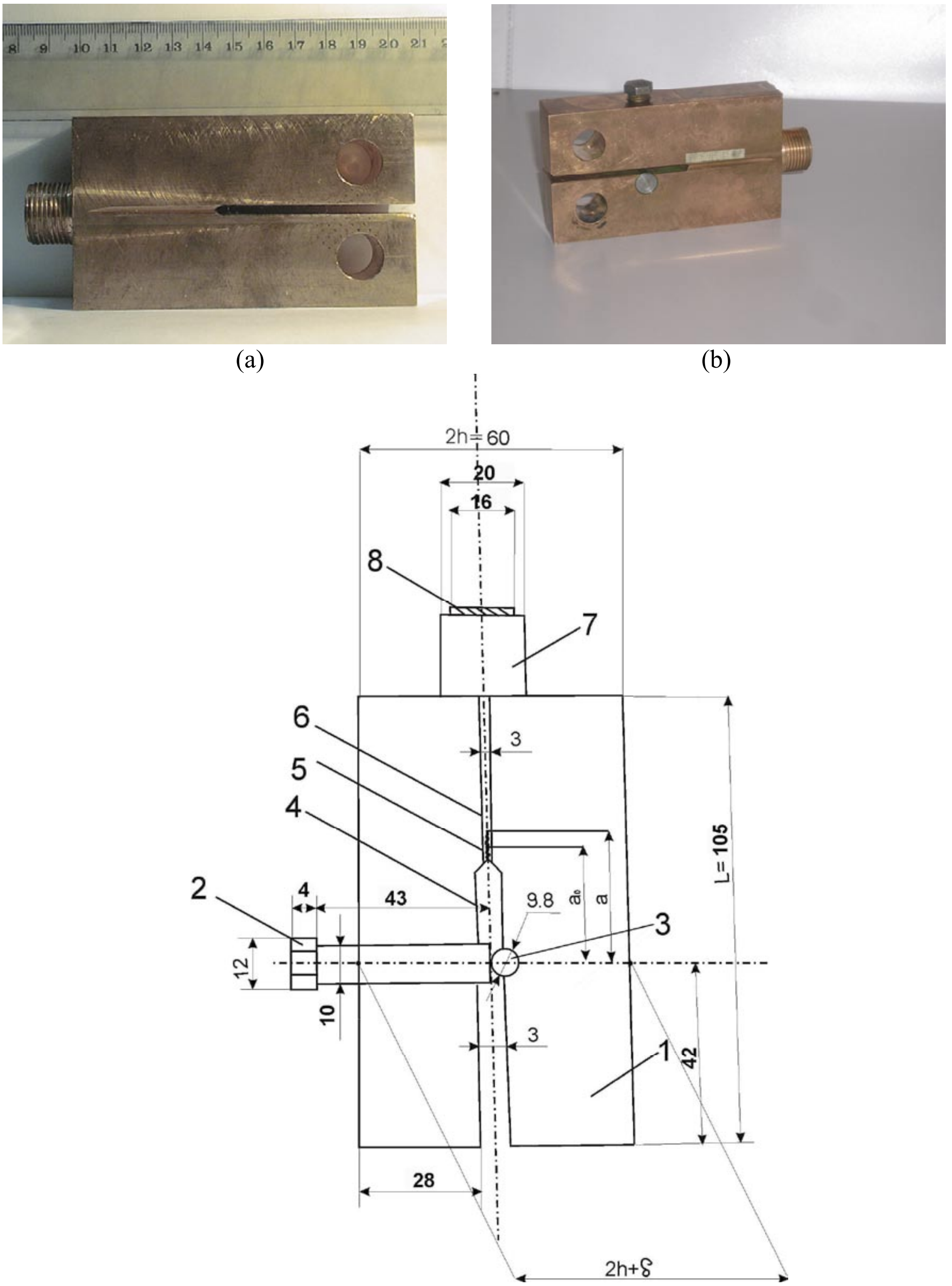

(a) (b)

(c)

***Figure 7.*** *Compact tension (CT) specimen for SCC tests at a fixed crack opening.*
*a, b – two photos of a CT specimen;*
*c – drawing of a CT specimen:*
*1 – CT specimen, 2 – fixing bolt, 3 – supporting cylinder (dowel), 4 – edge notch,*
*5 – fatigue-generated pre-crack, 6 – side groove, 7 – cylindrical pedestal with a thread,*
*8 – acoustic emission sensor.*

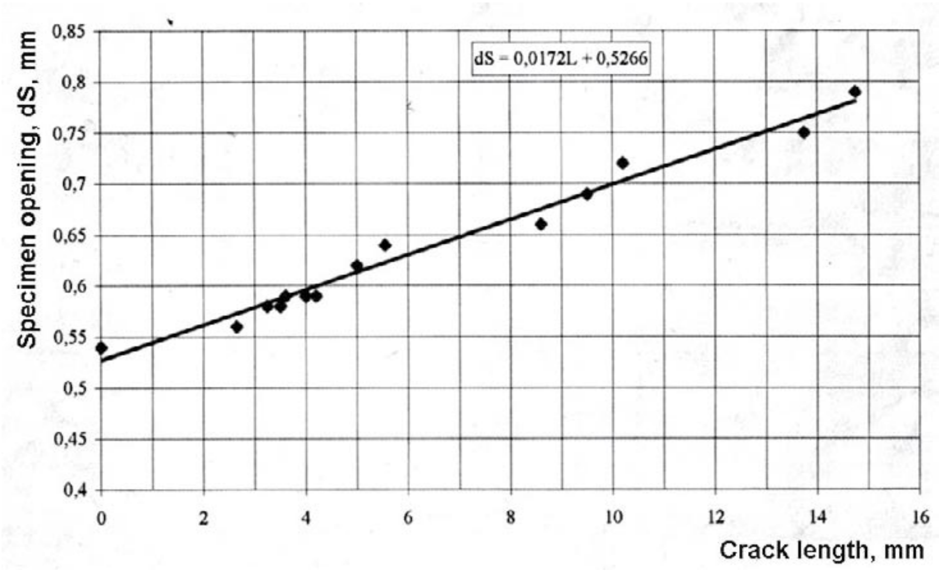

***Figure 8.*** *Calibration dependence for fatigue crack generation in CT specimens: Opening of the CT copper specimen in the direction of applied force vs. crack length. Cyclic loading: F = 0.5-10 kN.*

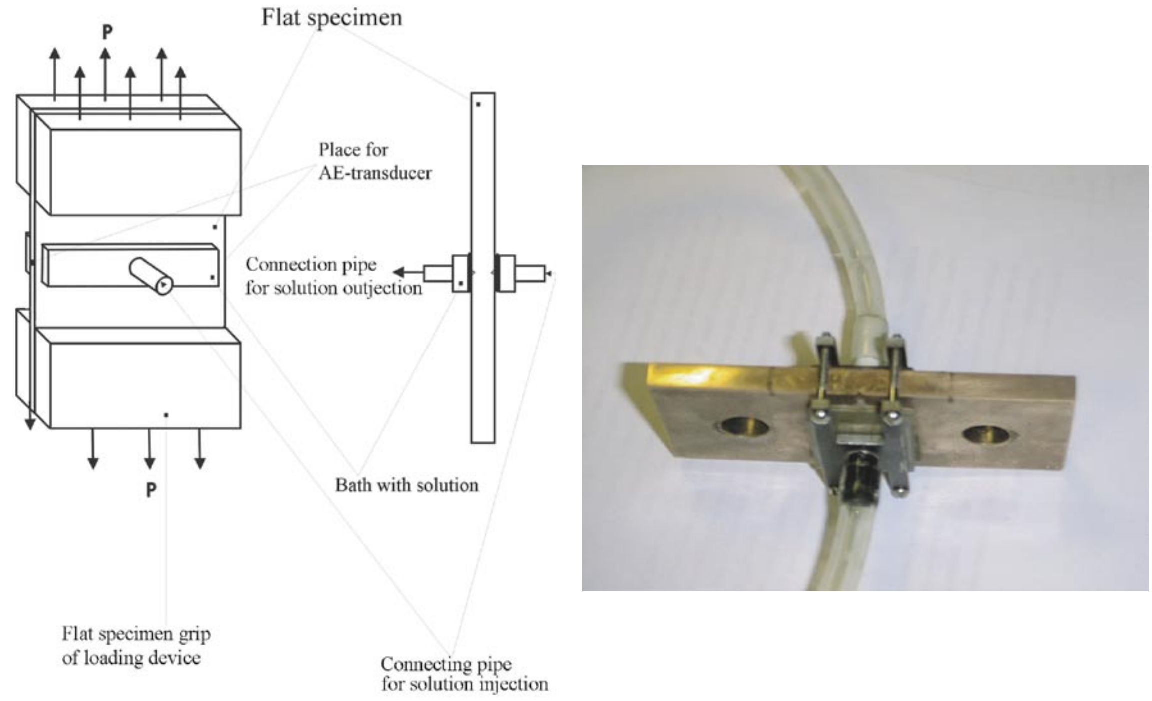

(a) (b)

***Figure 9.*** *MT panel specimen connected to the circulating solution system.*
*a – drawing of an MT panel specimen;*
*b – photo of an MT panel specimens attached to the circulating solution pipeline.*

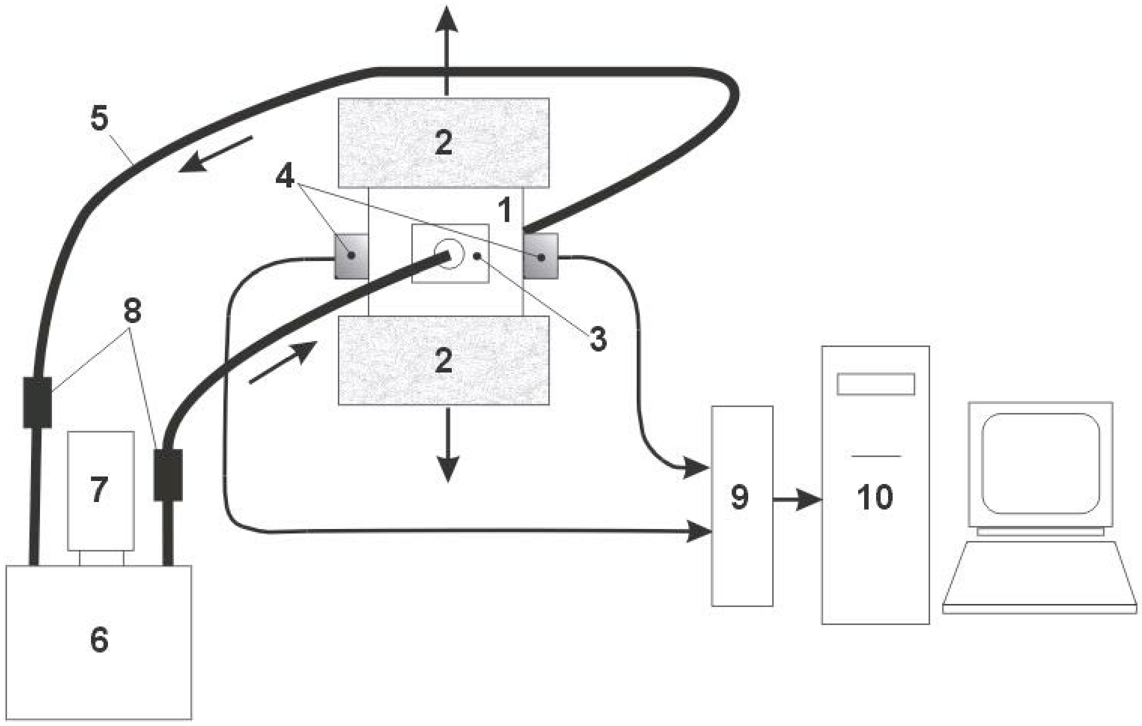

*Figure 10.* *Circulating solution system for the SCC constant extension rate tests combined with the system for acoustic emission monitoring of MT panel specimens.*
*1 – MT panel specimen,*
*2 – flat serrated grips for mounting the specimen,*
*3 – cup for circulation of corrosion solution,*
*4 – AE sensors and modules for signal pre-amplification and pre-processing,*
*5 – pipelines for circulation of the corrosive solution,*
*6 – a 5-liter reservoir with the corrosive solution,*
*7 – pump for solution circulation,*
*8 – acoustic filters,*
*9 – controller L-1250 for analog signal input to a PC,*
*10 – PC for digital processing and storage of the AE signals.*

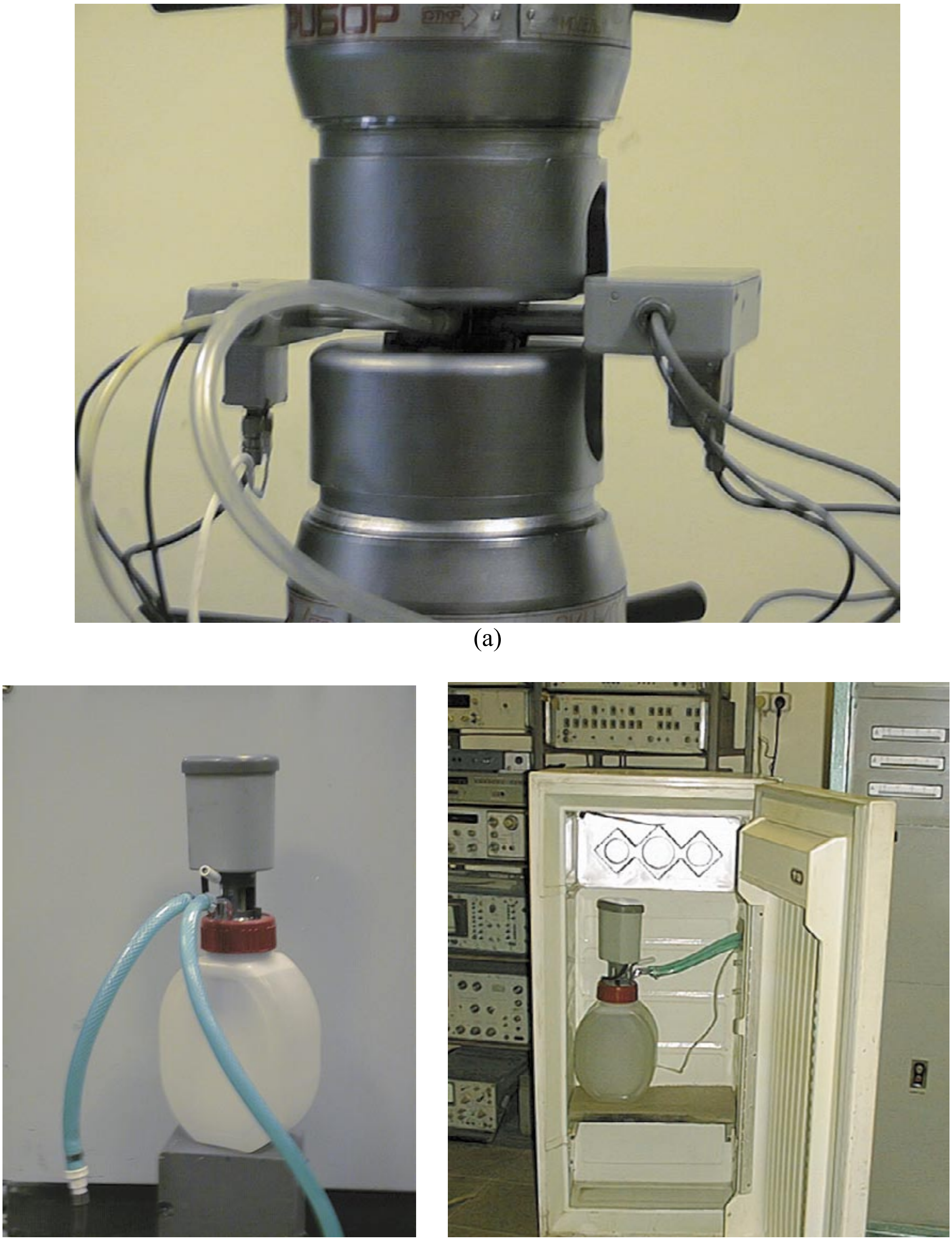

(a)

(b)

(c)

***Figure 11.*** *Elements of the circulating solution system.*
*a – specimen, attached to the circulating solution system, in the grips of the testing machine;*
*b – reservoir containing 0.1M $NaNO_2$ solution, together with the circulation pump;*
*c – assembly of the reservoir with the pump inside the acoustically isolated chamber.*

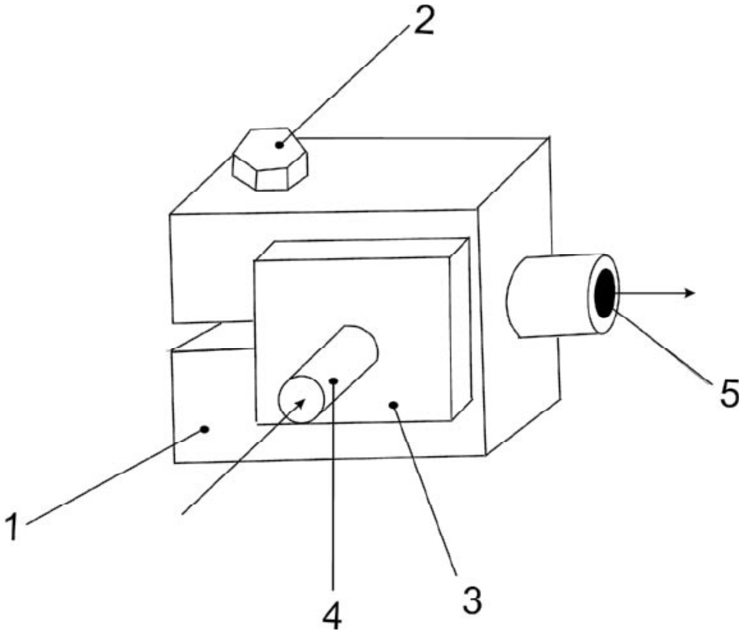

(a)

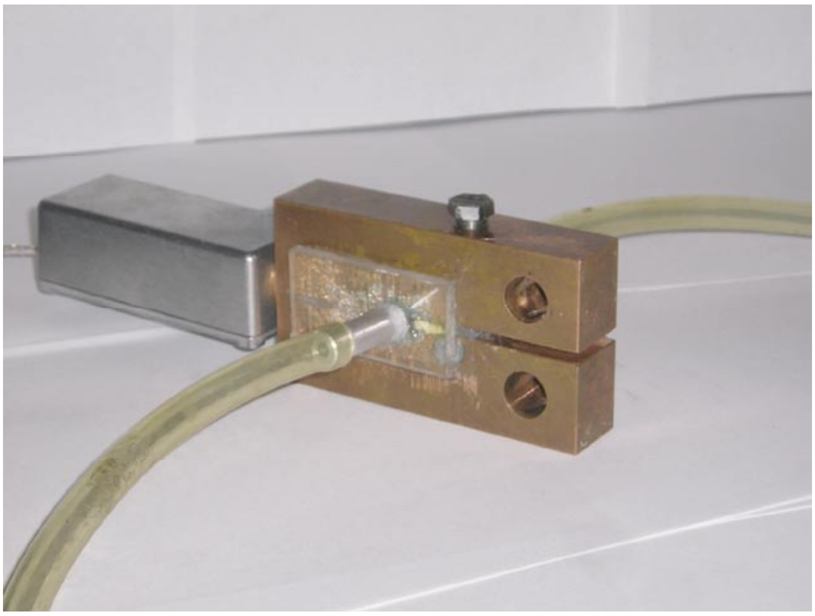

(b)

***Figure 12.*** *System for continuous circulation of the corrosive solution through the cracks in a CT specimen.*

*a – sketch of a CT specimen with an attached cup for the corrosive solution:*

*1 – CT specimen,*
*2 – fixing bolt,*
*3 – cup for corrosive solution,*
*4 – couplings connecting the cups to the pipeline,*
*5 – AE sensor;*

*b – photo of a CT specimen with the connected pipeline of solution supply and the module for analog AE signal pre-amplification and pre-processing.*

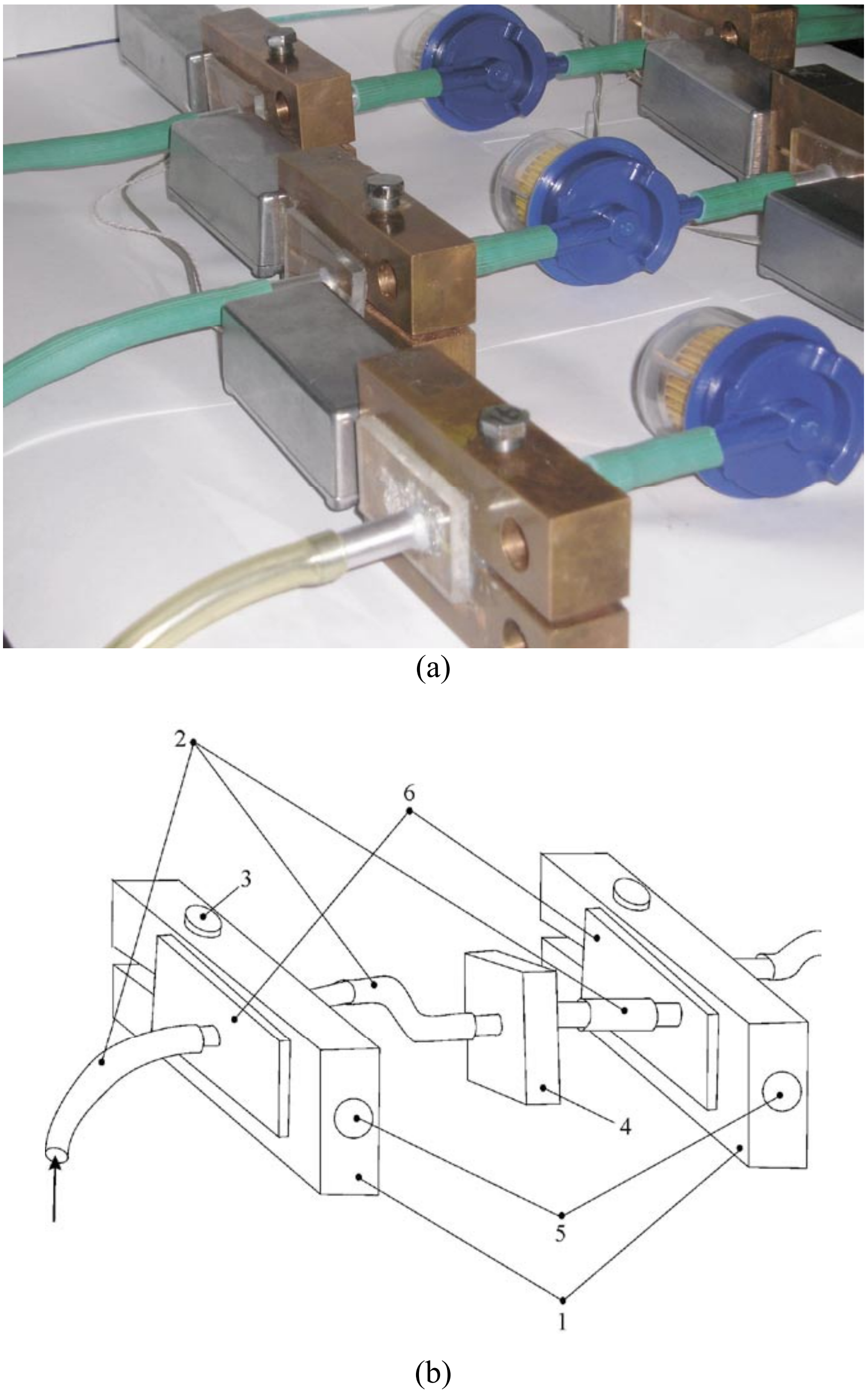

(a)

(b)

*__Figure 13.__ Sequential connection of two CT specimens to a closed-loop recirculation system.*
*a – photo of the specimen connections;*
*b – sketch of a connection:*
*1 – CT specimens,*
*2 – pipeline of the corrosive solution supply,*
*3 – fixing bolts,*
*4 – acoustic filter (acoustic trap),*
*5 – AE sensors,*
*6 – cups for corrosive solution.*

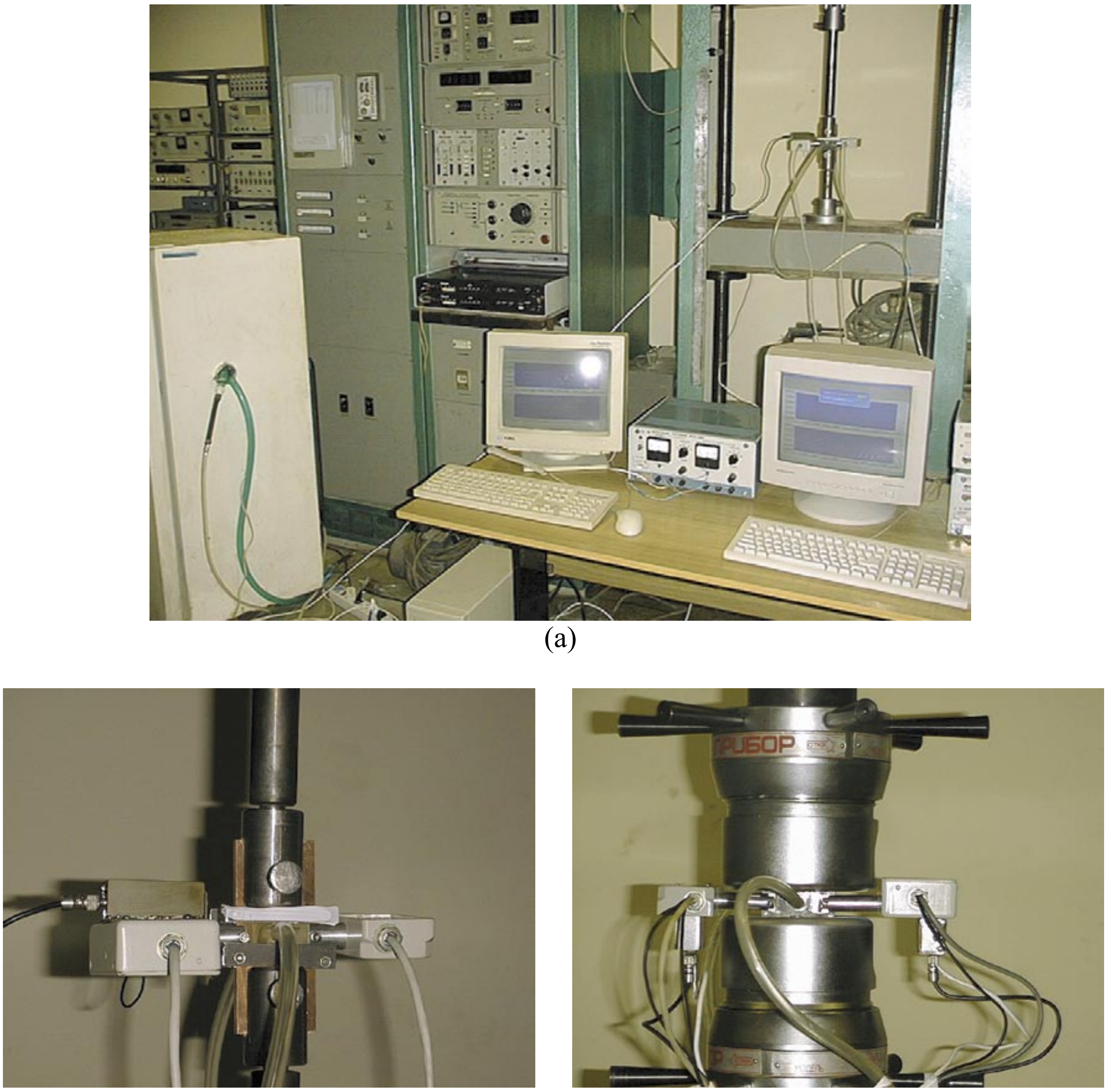

(a)

(b) (c)

***Figure 14.*** *Acoustic emission (AE) monitoring during SCC tests on MT panel specimens.*
*a – installation for SCC tests combined with AE monitoring;*
*b – MT panel specimen with the attached AE sensor that is made physically integral with a small-size electronic module for analog pre-processing;*
*c – placement of the AE sensors on a specimen during tests.*

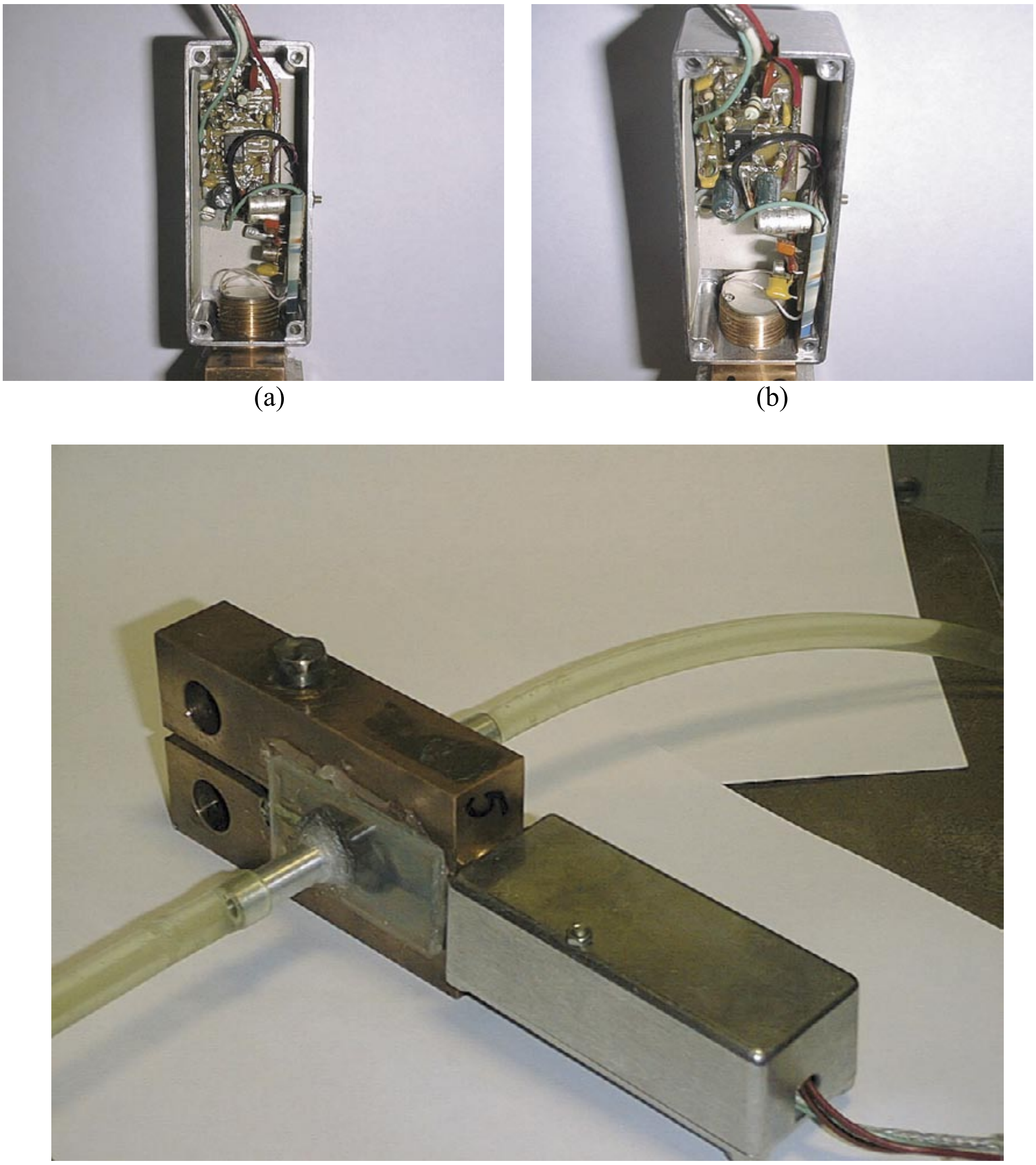
(a) (b)

(c)

***Figure 15.*** *Acoustic emission (AE) monitoring during SCC tests on CT specimens at a fixed crack opening.*
*a, b – mounting of an AE sensor and of an analog pre-processing module on the cylindrical pedestal of a CT specimen;*
*c – CT specimen with the installed electronic module and with the attached system for continuous circulation of corrosive solution through the crack.*

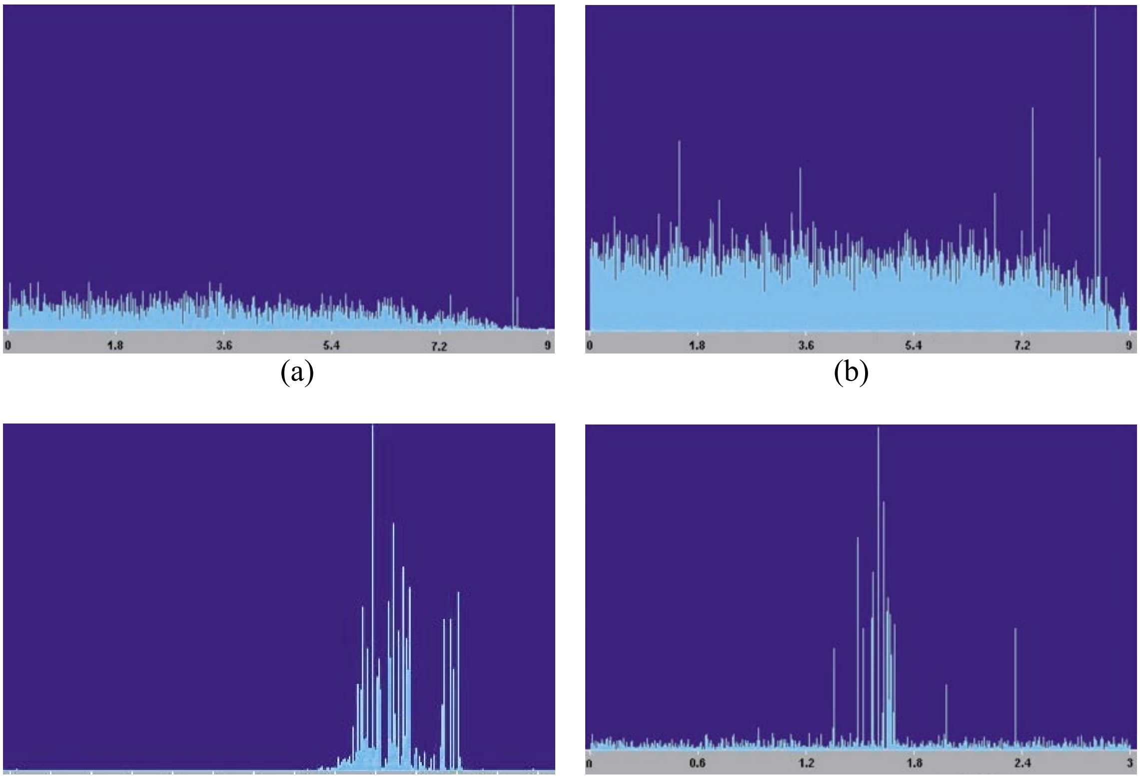

(a) (b)

(c) (d)

***Figure 16.*** *Typical acoustic emission (AE) signals during SCC tests on MT specimens.*
*a, b – decreasing amplitude level of 'continuous' AE (from micro-fracture events during SCC) before the stage of 'burst' AE (from macro-fracture at SCC). The time scale on X-axis – hours (moment t = 0 is offset from the start of the test);*
*c, d – signals of 'burst' AE on AE diagrams of SCC, the time scale on X-axis – hours (moment t = 0 is offset from the start of the test).*

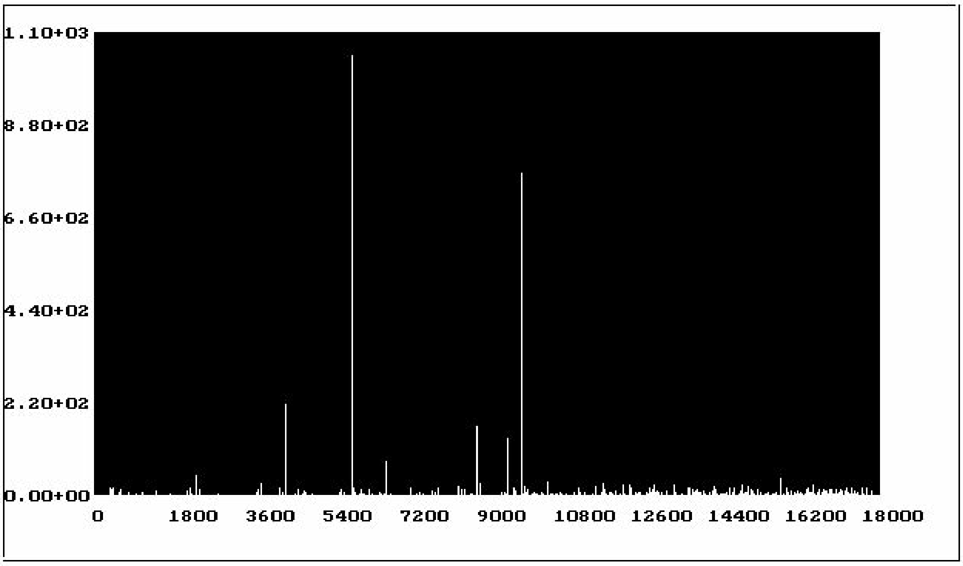

***Figure 17.*** *Scale of the amplitude changes of AE pulses (Y – arbitrary units) during SCC on the part of AE-diagram with 'burst' AE. The time scale on X-axis – seconds.*

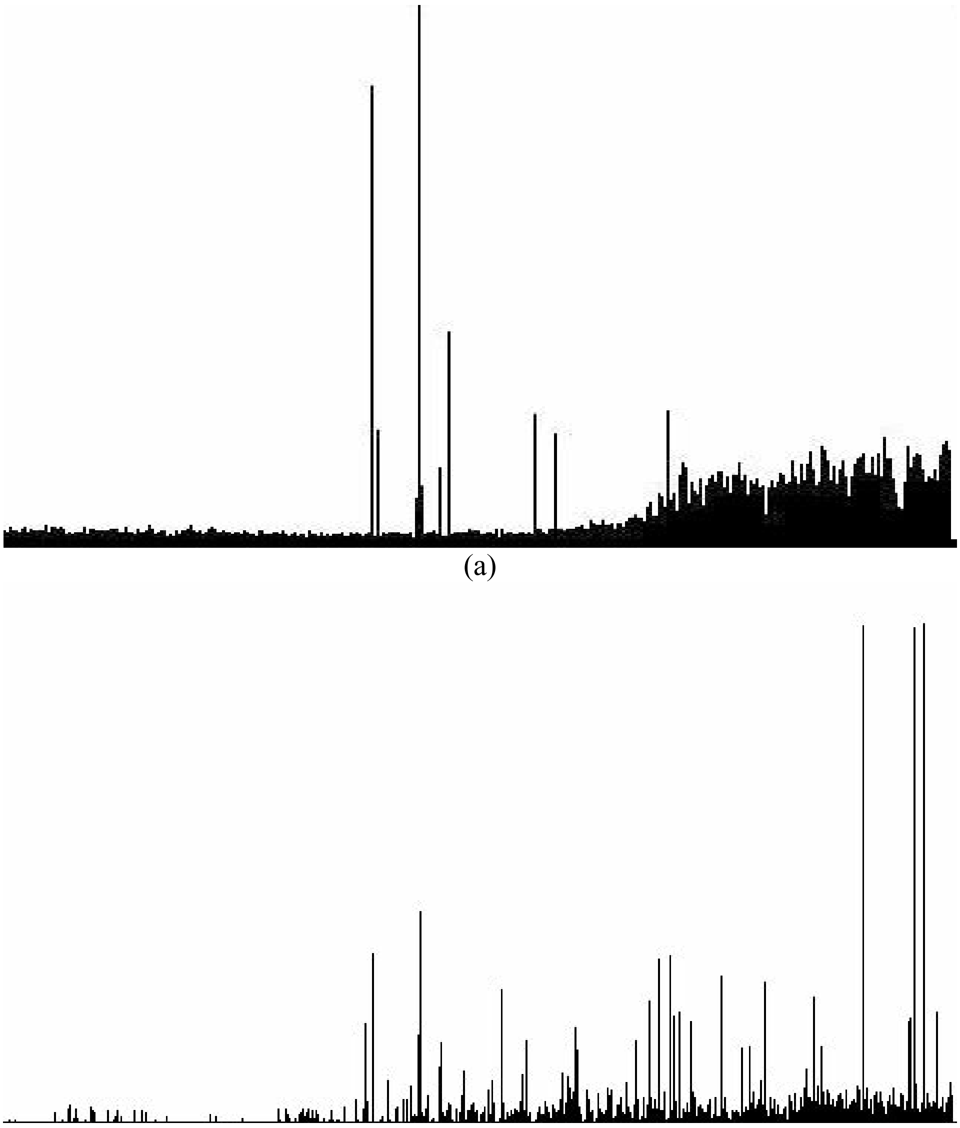

(a)

(b)

***Figure 18.*** *Variants of the SCC kinetics discriminated by AE monitoring during extension of MT panel specimens.*

*a – transition to micro-fracture dominated mode (amplitude growth of 'continuous' AE) at the second stage of SCC kinetics;*

*b – predominance of macro-fracture mode with increasing the load on the specimen (amplitude growth of 'burst' AE) at the second stage of SCC kinetics.*

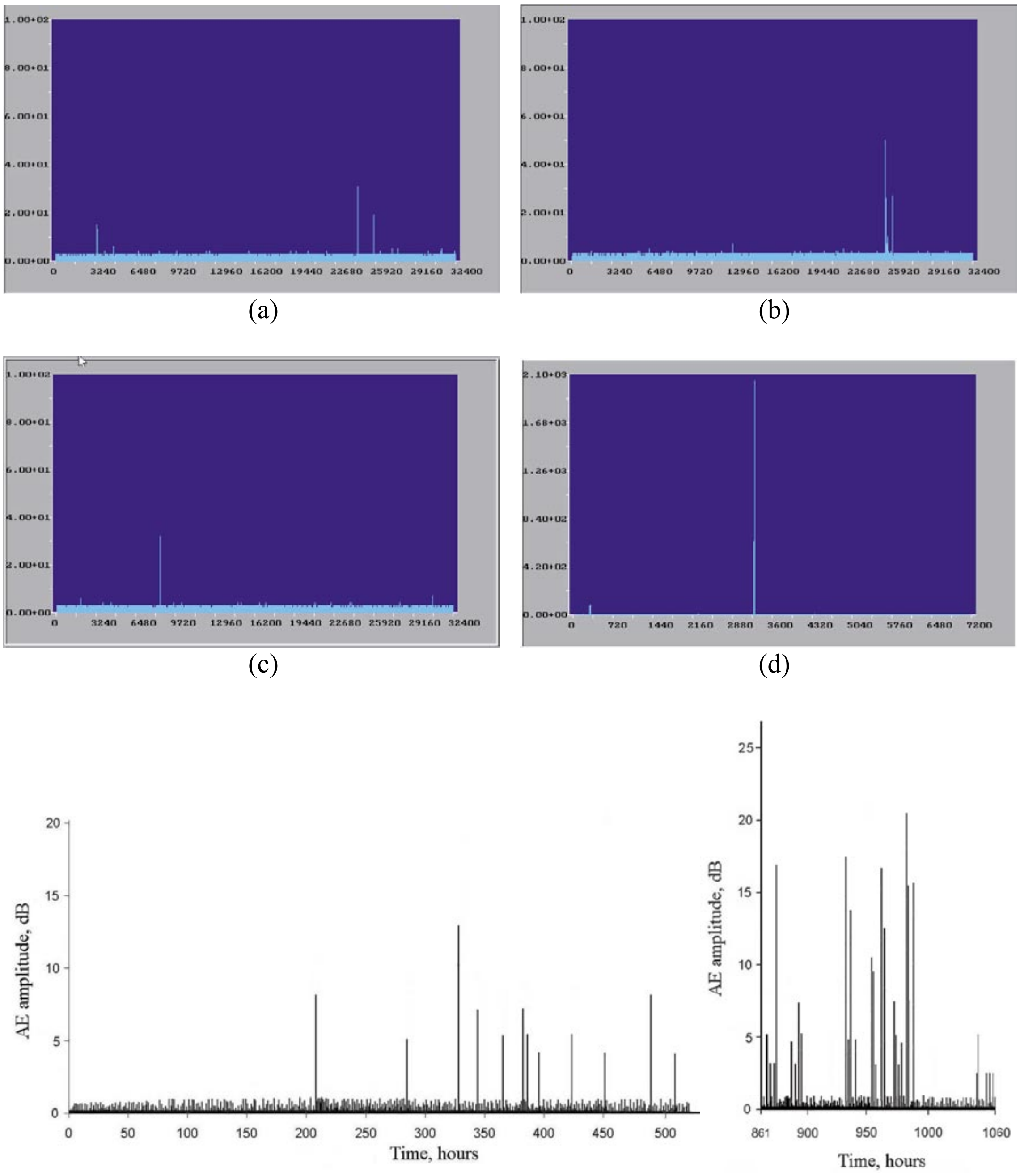

(a) (b)

(c) (d)

(e)

***Figure 19.*** *Acoustic emission signals during SCC test on a compact tension (CT) specimen. a, b, c, d – typical AE-signals (Y – arbitrary units; the time scale on X-axis – seconds); e – AE-signals recorded during 1,050 hours of the SCC test.*

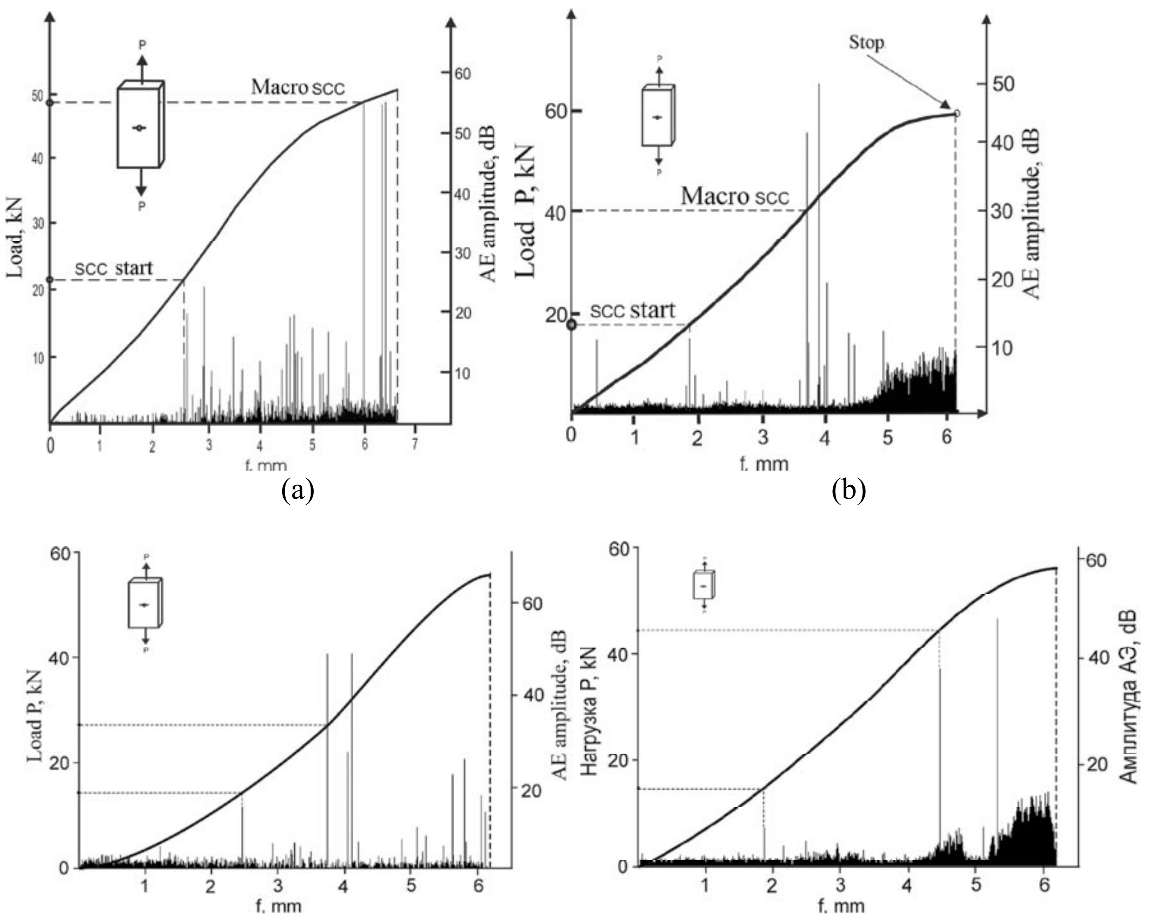

(a) (b)

(c) (d)

***Figure 20.*** *Examples of the joint deformation diagrams and AE diagrams for MT panel specimens during SCC CERT experiments, for obtaining estimates of copper resistance to corrosion-assisted fracture at two characteristic stages of SCC kinetics.*

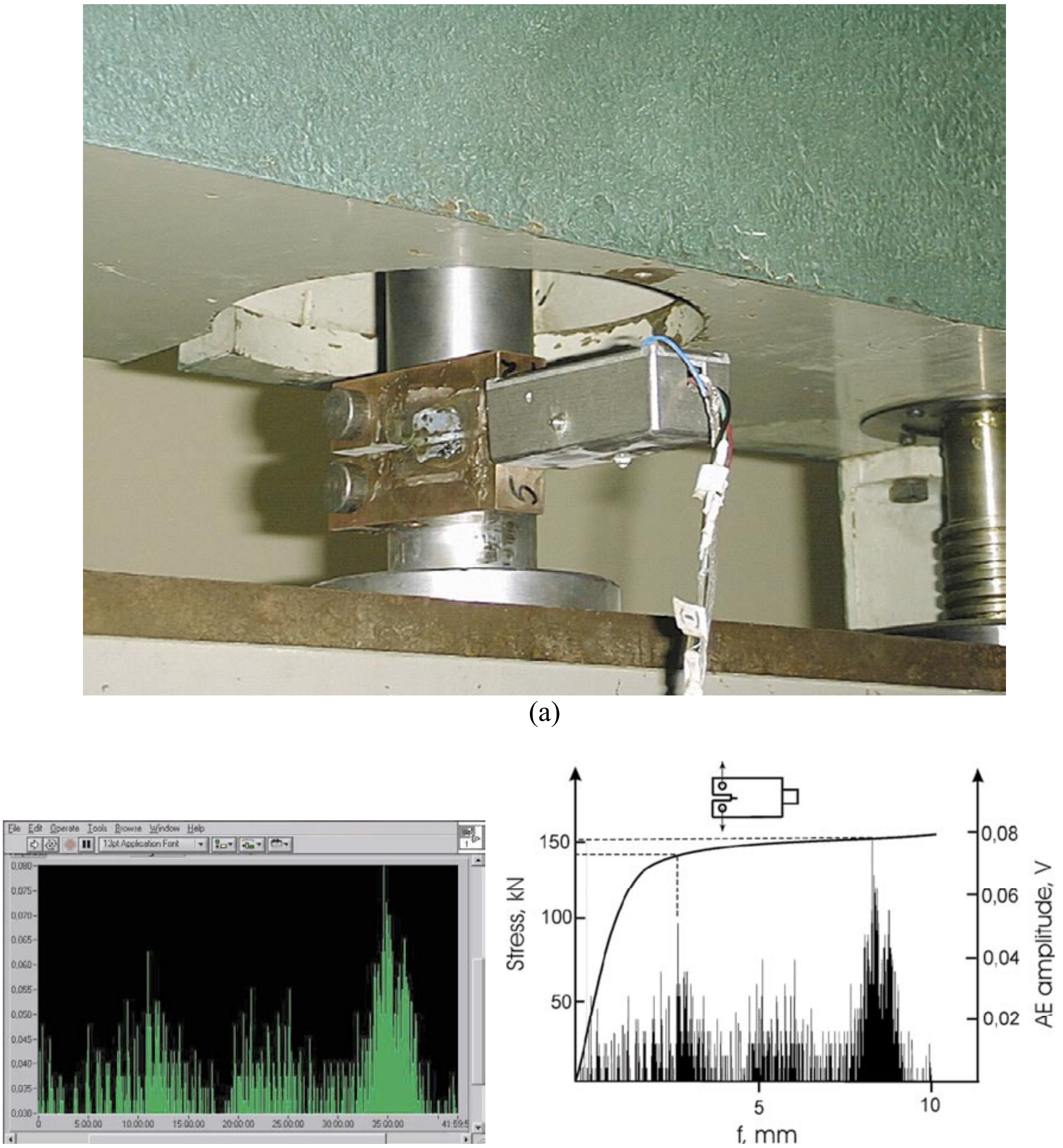

(a)

(b) (c)

***Figure 21.*** *Tensile test on a compact tension (CT) specimen after completion of the SCC test.*
*a – CT-specimen mounted in the grips of a testing machine;*
*b – AE-signals during extension of a CT-specimen;*
*c – the joint deformation diagrams and AE diagrams for compact tension (CT) specimen (using extension rate 0.02 mm/sec). This experiment was performed after completion of the SCC test, for obtaining estimates of the copper fracture resistance, and it also shows two characteristic stages of the fracture kinetics.*

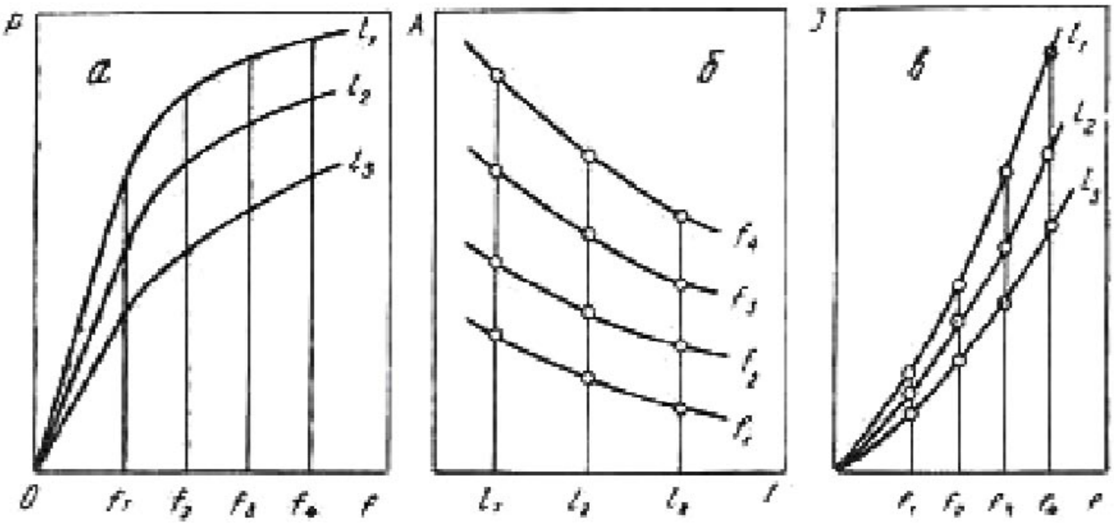

(a) (b) (c)

***Figure 22.*** *Schematic diagrams for J-integral calculations using Begley-Landes technique.*
*a – deformation diagrams "Load (P) – displacement of points of applied load (f)" for several initial crack lengths, L;*
*b – diagrams "work of sample deformation – crack length" for several different displacements of points of applied load, f;*
*c – diagrams "J-integral – displacement of points of applied load (f)" for several cracks with different initial lengths.*

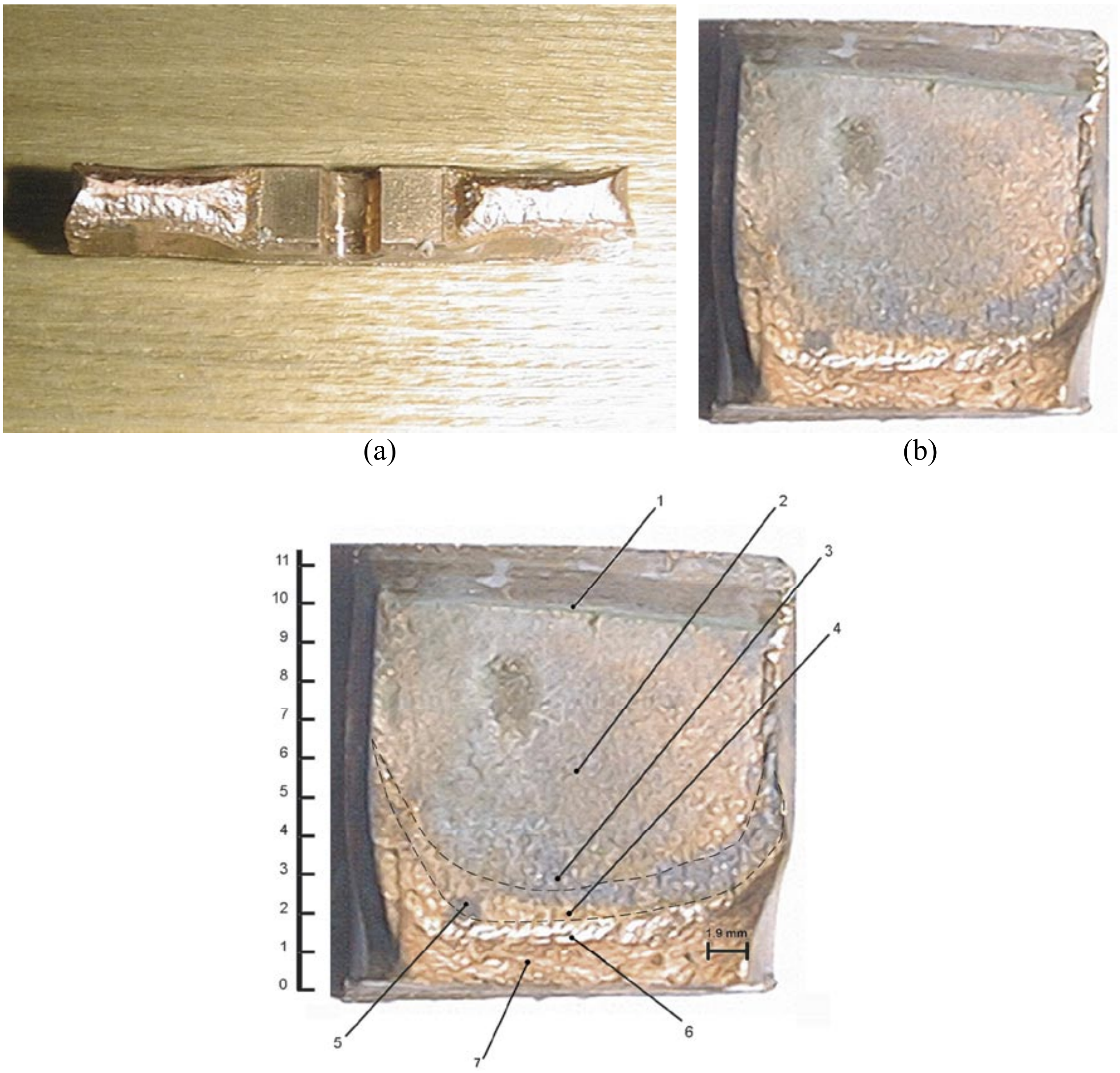

(a) (b)

(c)

***Figure 23.*** *Specimens prepared for microfractographic SEM-analysis.*
*a – panel MT specimen;*
*b, c – compact tension (CT) specimen:*
*1 – edge of the through-thickness notch in the CT specimen,*
*2 – fatigue pre-crack zone,*
*3 – fatigue pre-crack front,*
*4, 5 – SCC fracture zone,*
*6 – stretch zone formed during the specimen rupture (after completion of the SCC test),*
*7 – ductile fracture zone formed during the specimen rupture.*

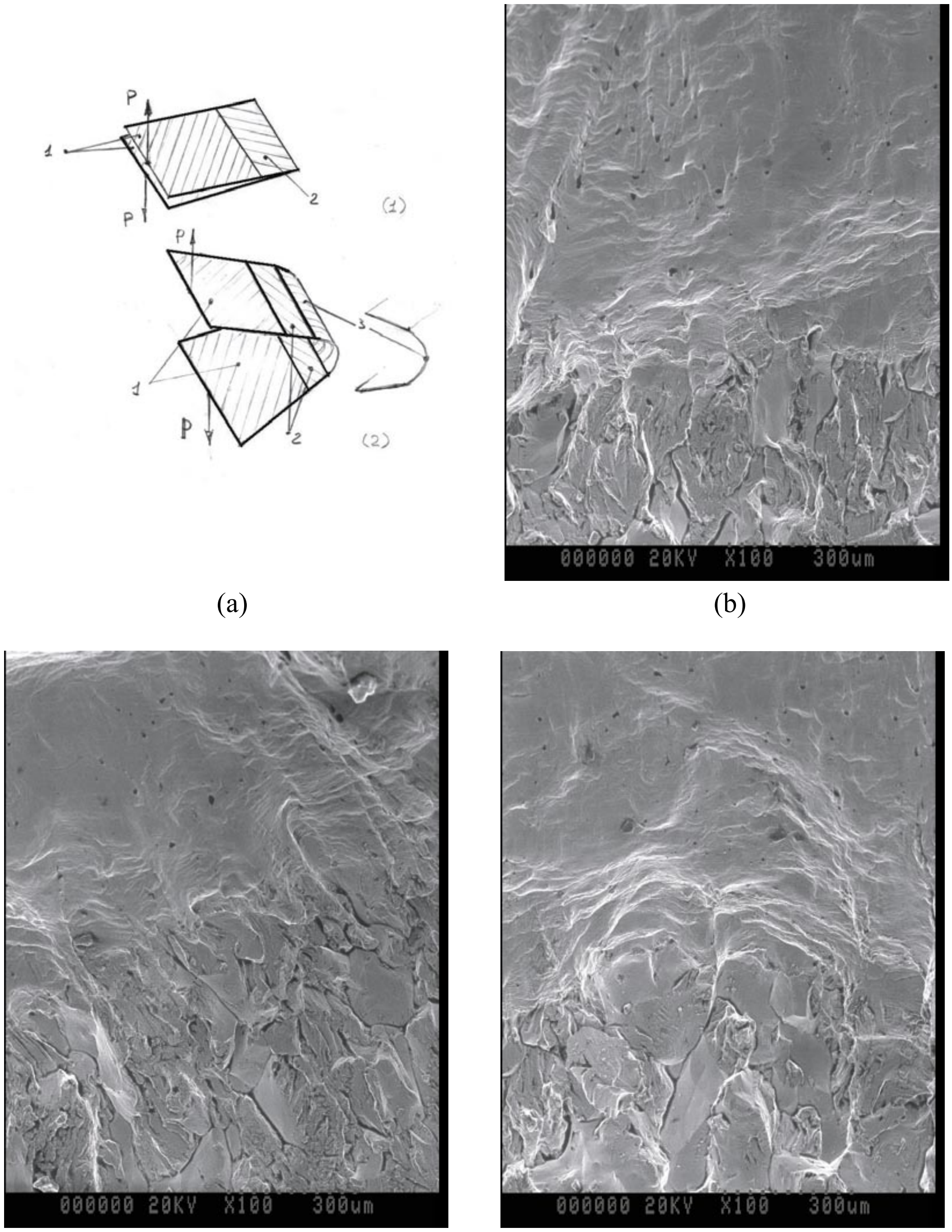

(a) (b)

(c) (d)

***Figure 24.*** *Fracture surface of a copper MT panel specimen, with a sharp fatigue pre-crack, in the absence of SCC.*
*a – scheme of the stretch zone formation upon the fatigue pre-crack opening without SCC:*
*1 – spark-erosion notch,*
*2 – fatigue pre-crack,*
*3 – stretch zone;*
*b, c, d – fractographic micrographs showing fatigue pre-crack zones (at the bottom of each micrograph) and stretch zones (at the top of each micrograph).*

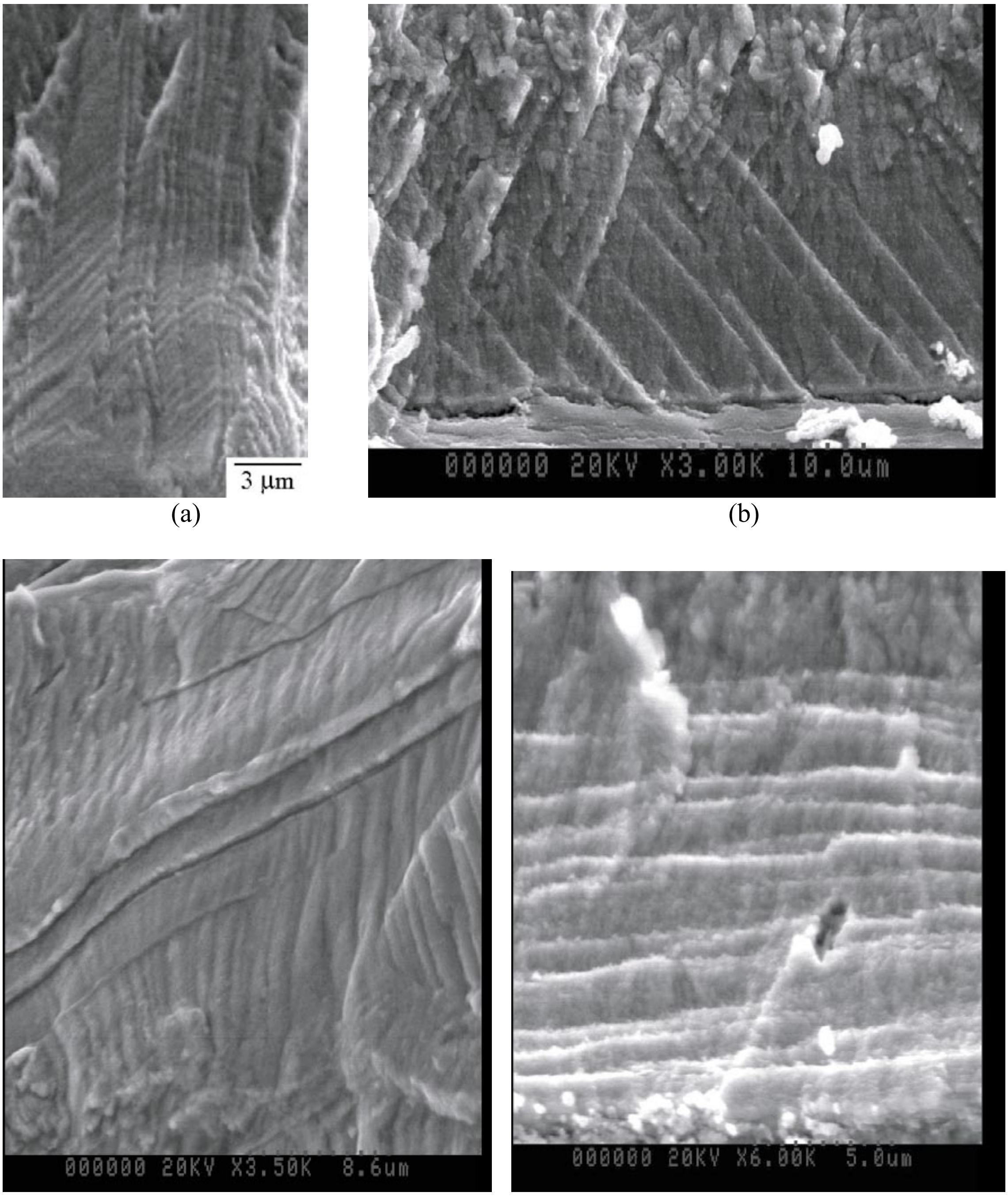

(a) (b)

(c) (d)

***Figure 25.*** *Brittle transgranular SCC fracture (continued on the next page).*
*a, b, c, d – cleavage along parallel planes.*

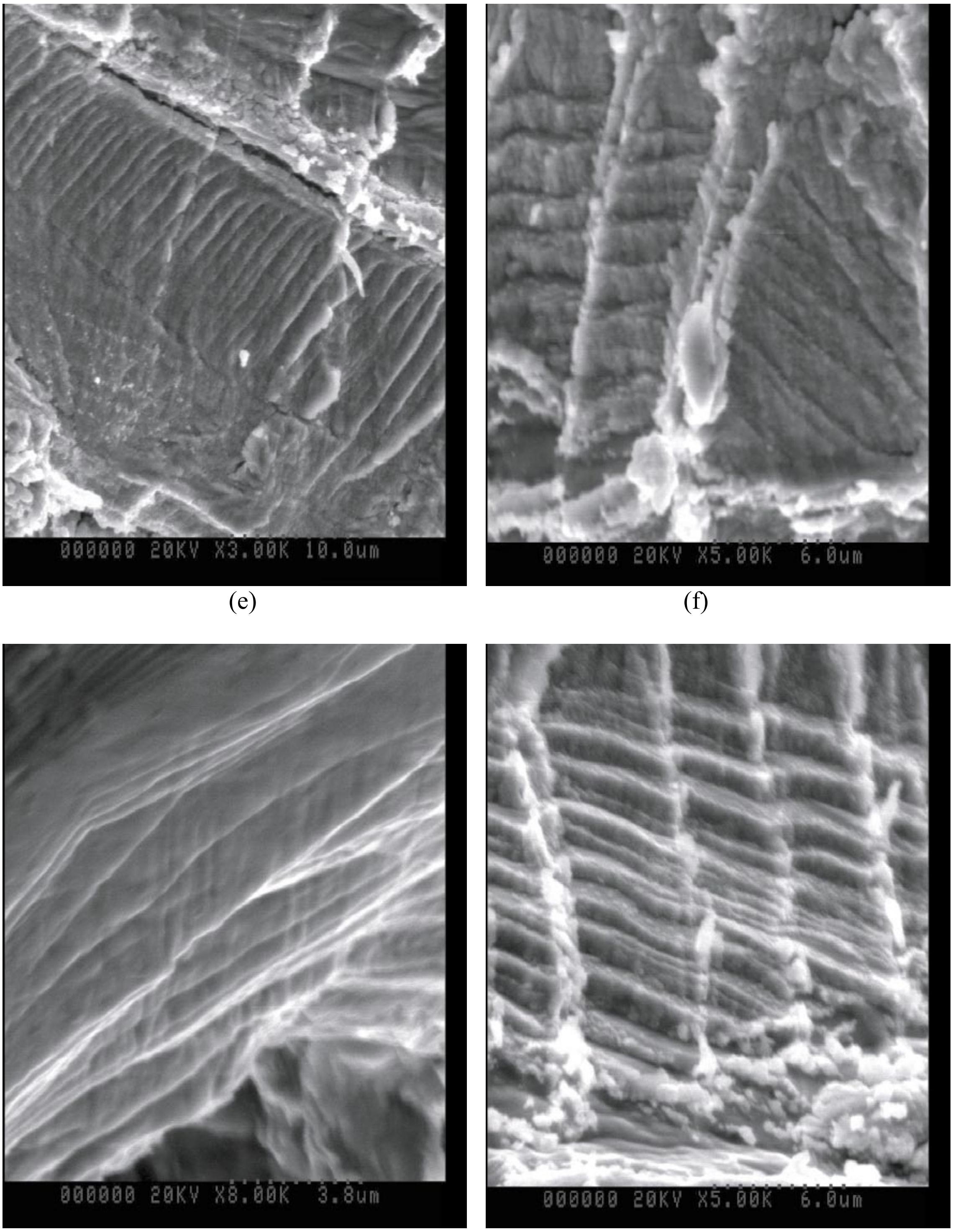

(e) (f)

(g) (h)

***Figure 25.*** *Brittle transgranular SCC fracture (continued on the next page).*
*e, f, g, h – cleavage along parallel planes.*

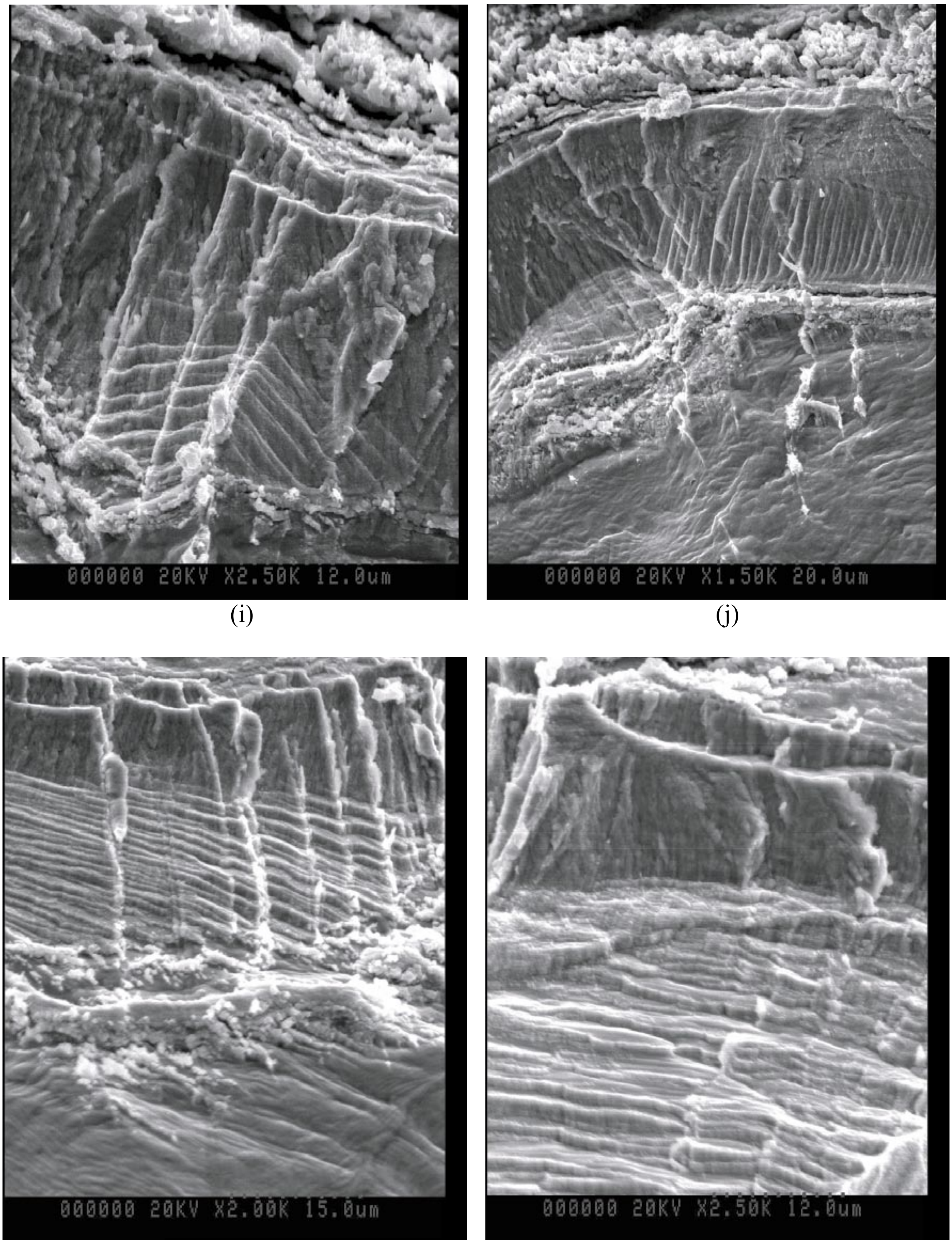

(i) (j) (k) (l)

***Figure 25.*** *Brittle transgranular SCC fracture.*
*i, j, k, l – cleavage steps. SCC fracture propagates from top to bottom.*

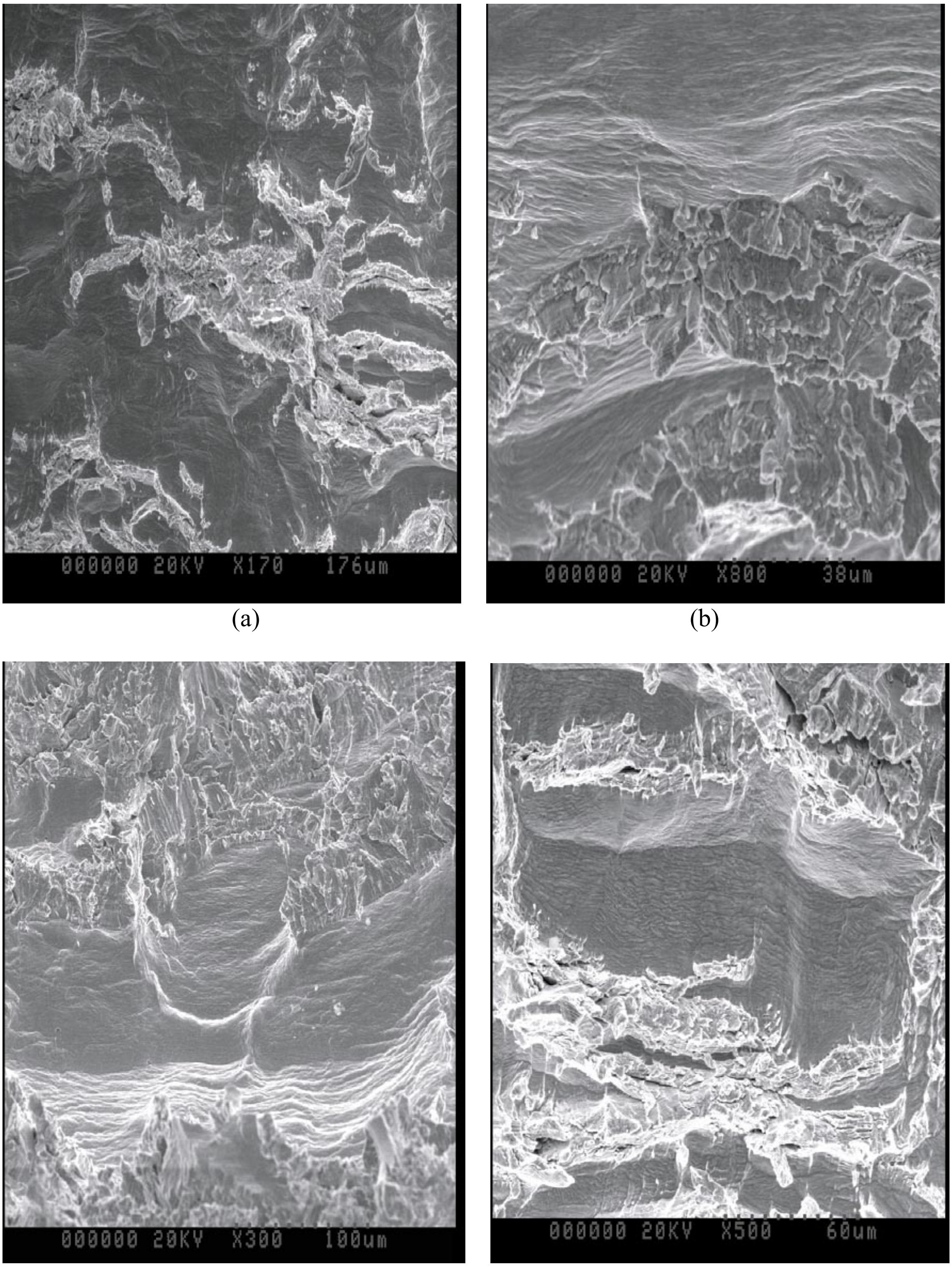

(a) (b)

(c) (d)

***Figure 26.*** *Transgranular SCC fracture not exhibiting crystallographically oriented facets on the fractured surface.*

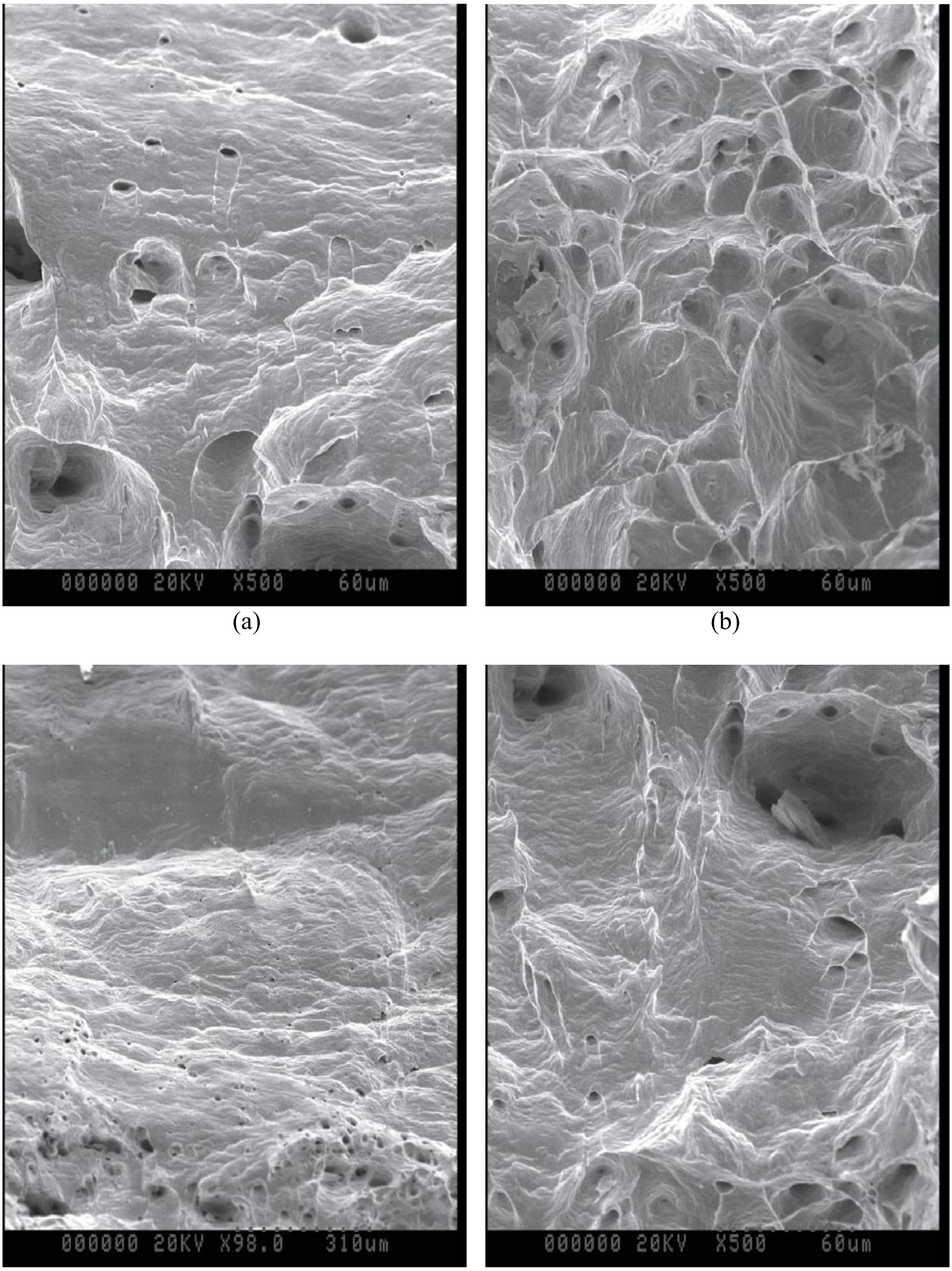

(a) (b)

(c) (d)

***Figure 27.*** *Ductile fracture of copper panel specimens at a late stage of deformation.*

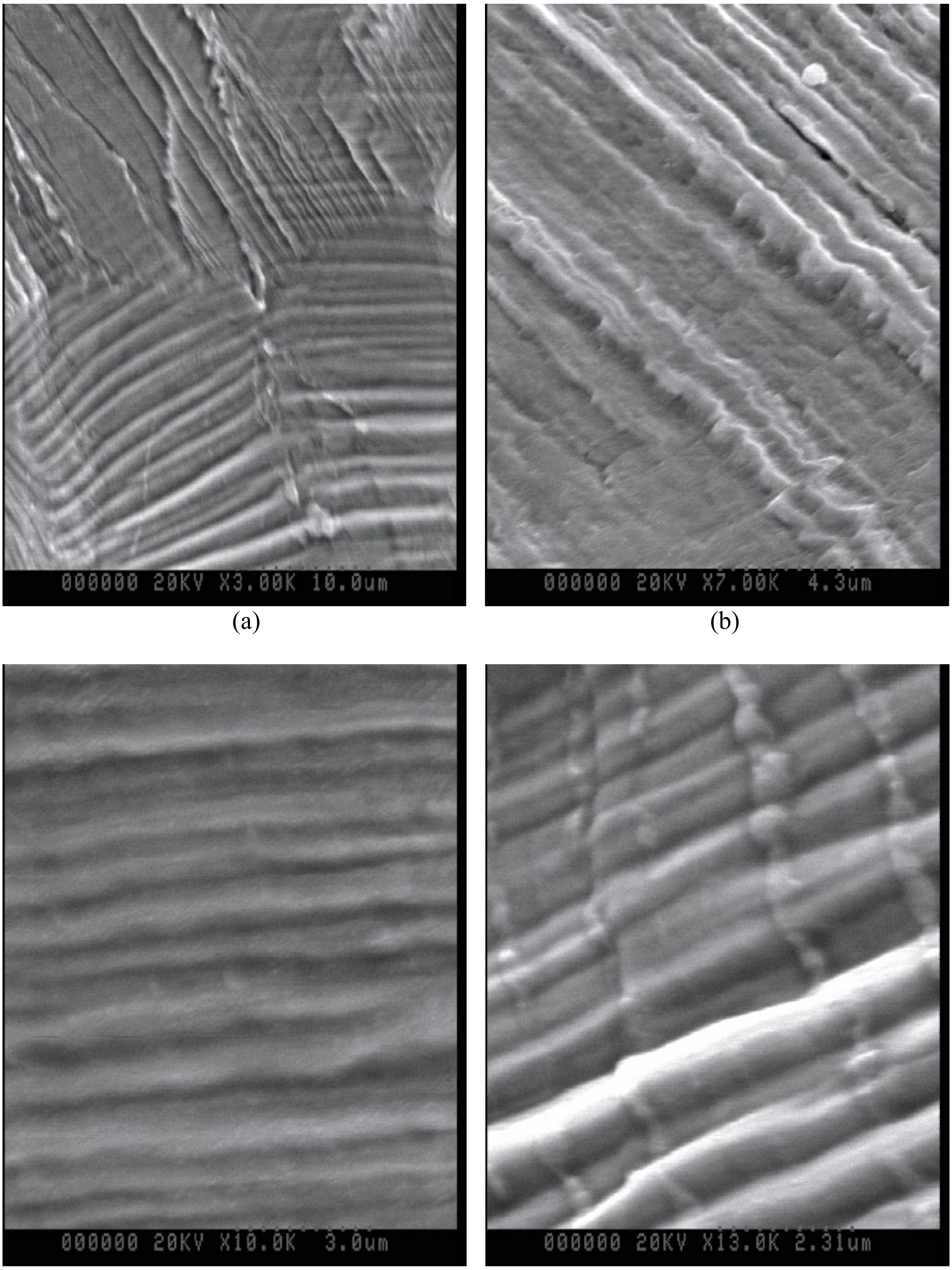

(a) (b)

(c) (d)

***Figure 28.*** *Intermittent character of SCC in copper (continued on the next page).*
*a – transition from the transgranular cleavage along parallel planes (top) to the intermittent transgranular SCC mode;*
*b, c, d – SCC striations.*

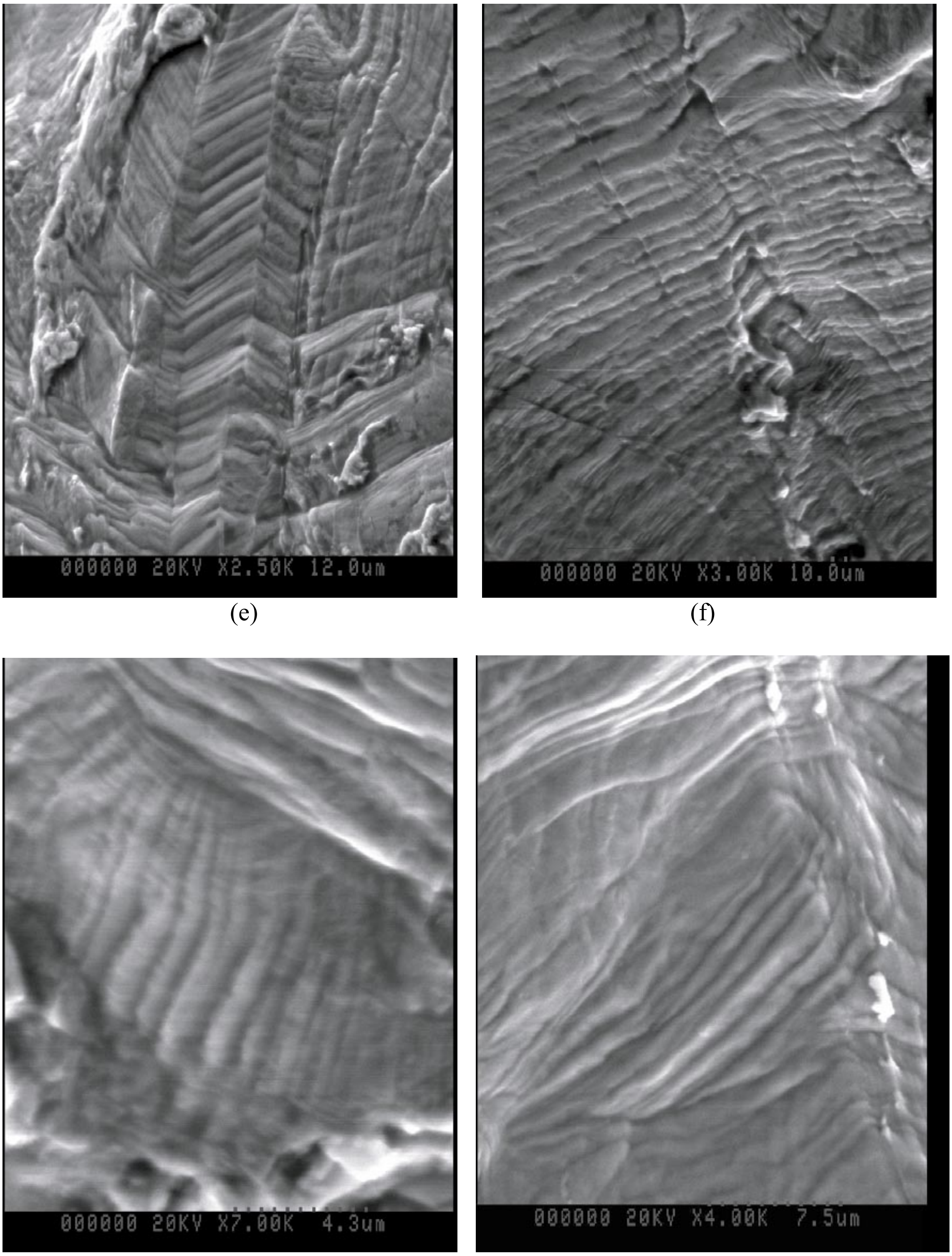

(e) (f)

(g) (h)

***Figure 28.*** *Intermittent character of SCC in copper.*
*e, f, g, h – SCC striations.*

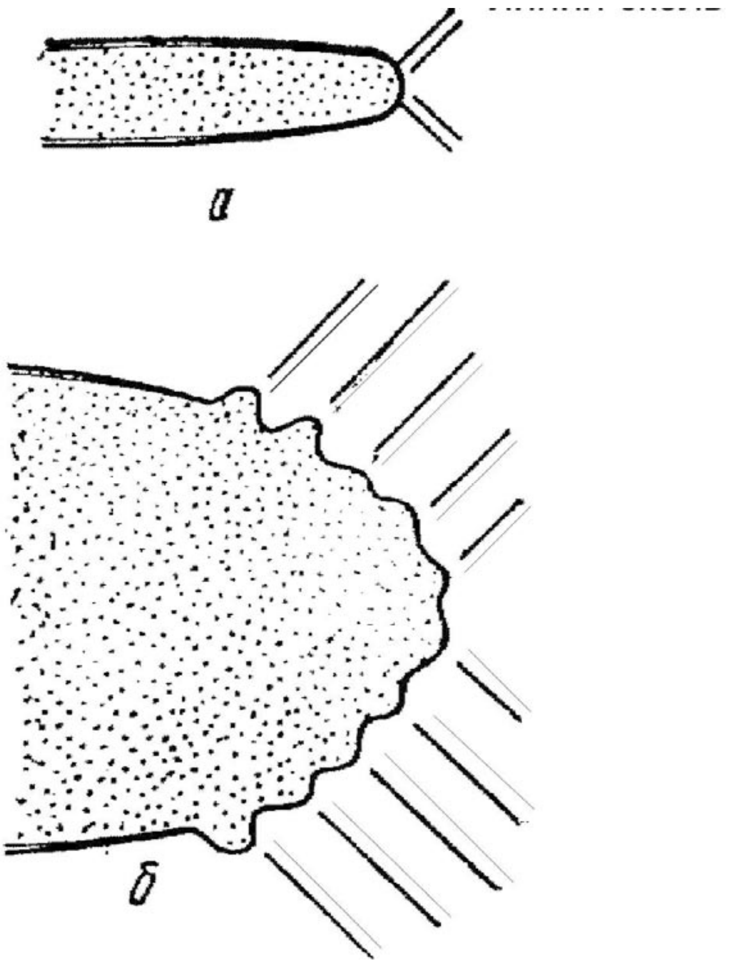

***Figure 29.*** *Scheme of localized plastic flow at the tip of SCC crack, producing rupture of the protective film (a), followed by anodic dissolution of the material at the tip (b).*

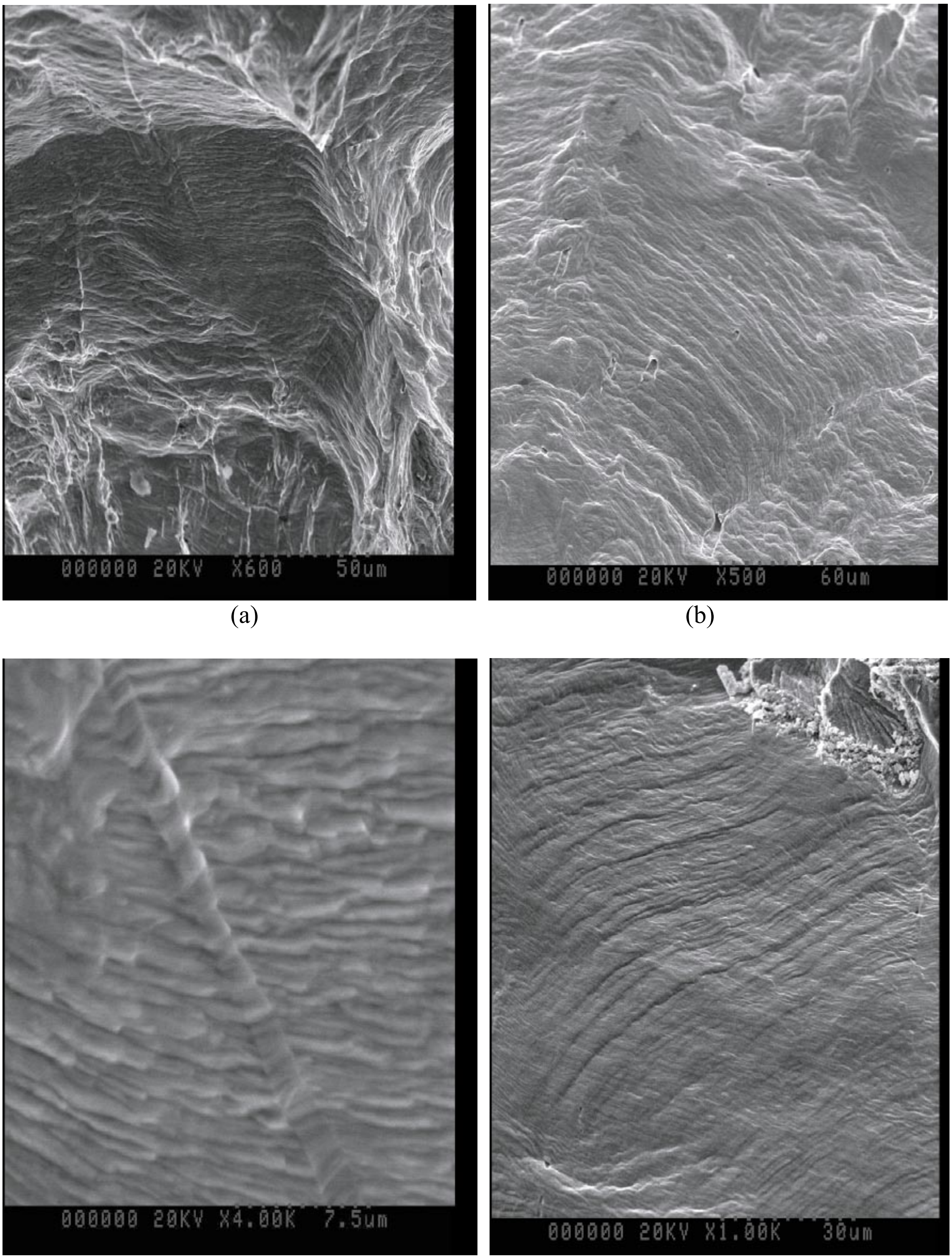

(a) (b)

(c) (d)

***Figure 30.*** *Smoother topography of the fracture surface produced by developed SCC.*

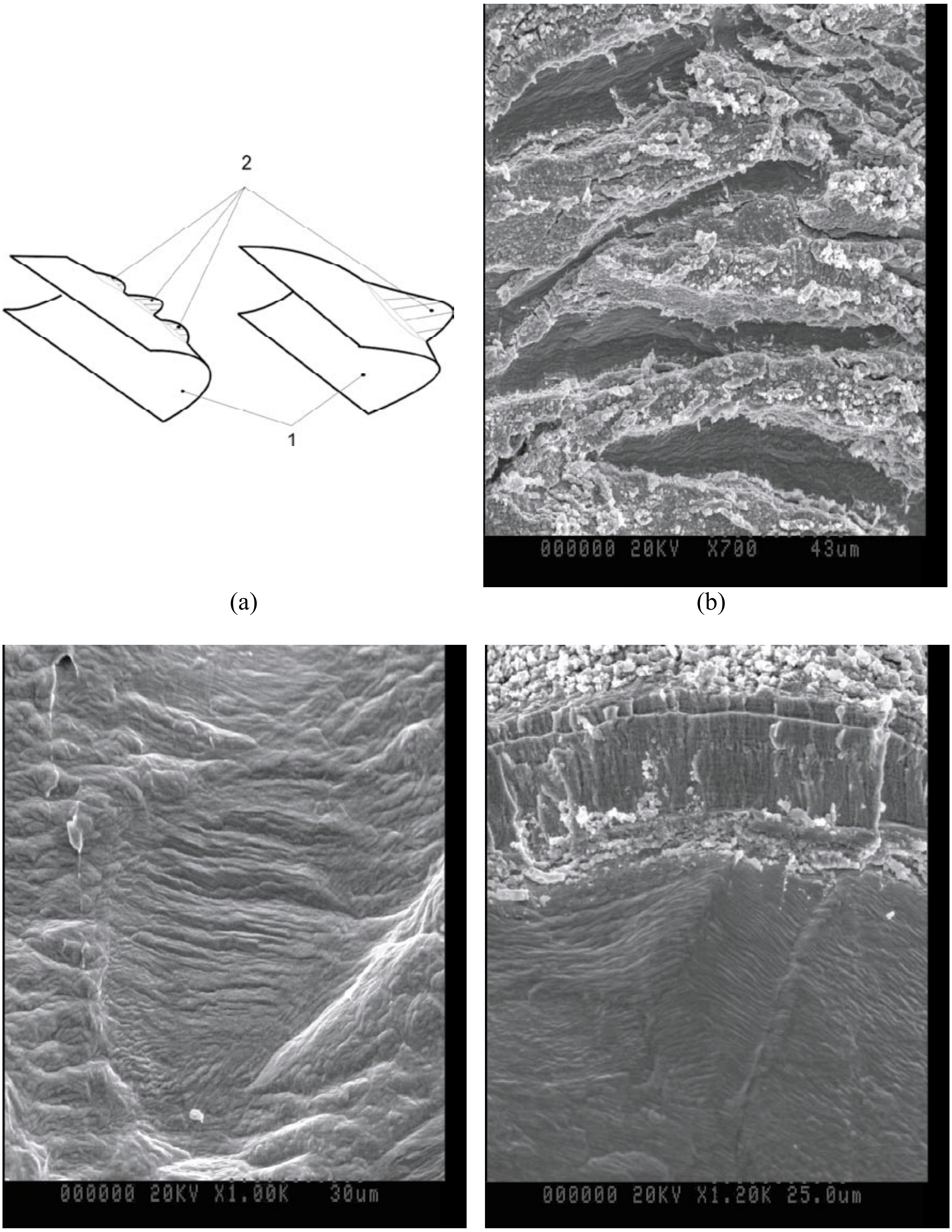

(a) (b)

(c) (d)

***Figure 31.*** *SCC 'lobes' appearing at the stage of slow SCC evolution.*

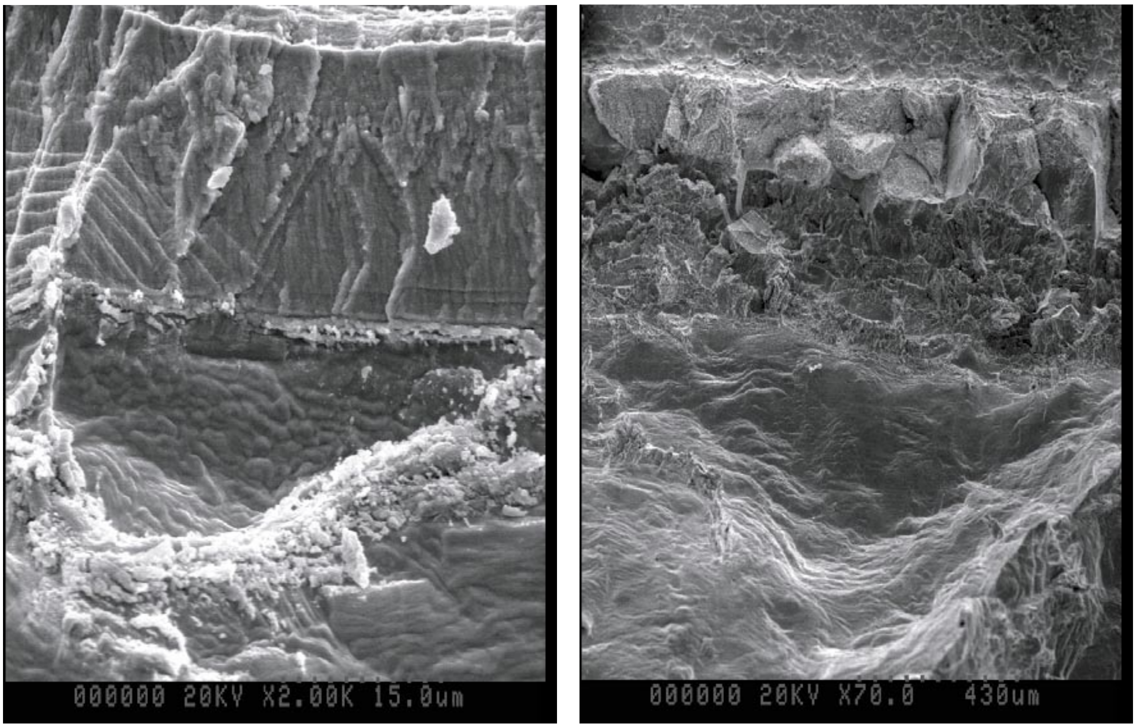

*Figure 32.* Narrowing of the crack front (crack tunneling) with the development of plastic deformation from the side surfaces of the specimen.

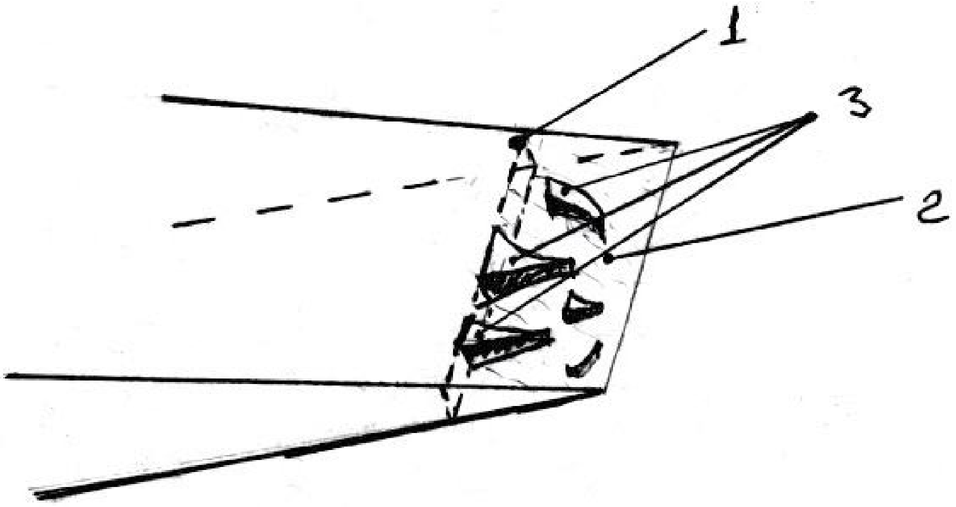

***Figure 33.*** *Formation of ligaments between adjacent SCC zones.*
*1 – fatigue crack front,*
*2 – SCC zones,*
*3 – non-fractured material areas (ligaments).*

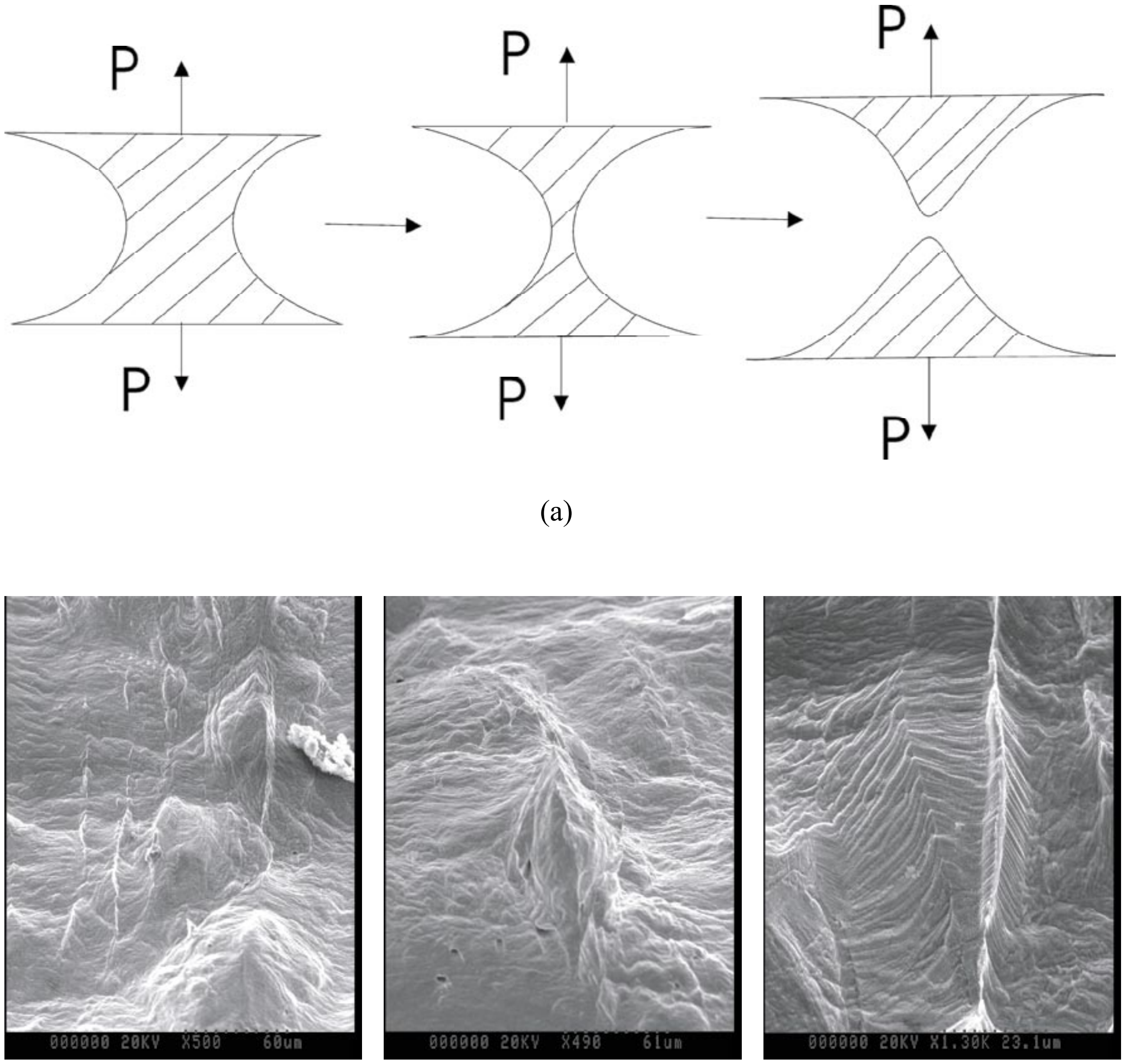

(a)

(b) (c) (d)

***Figure 34.*** *Ductile rupture of ligaments between SCC zones.*
*a – scheme illustrating ductile necking;*
*b, c, d – 'ductile ridges' of ruptured ligaments.*

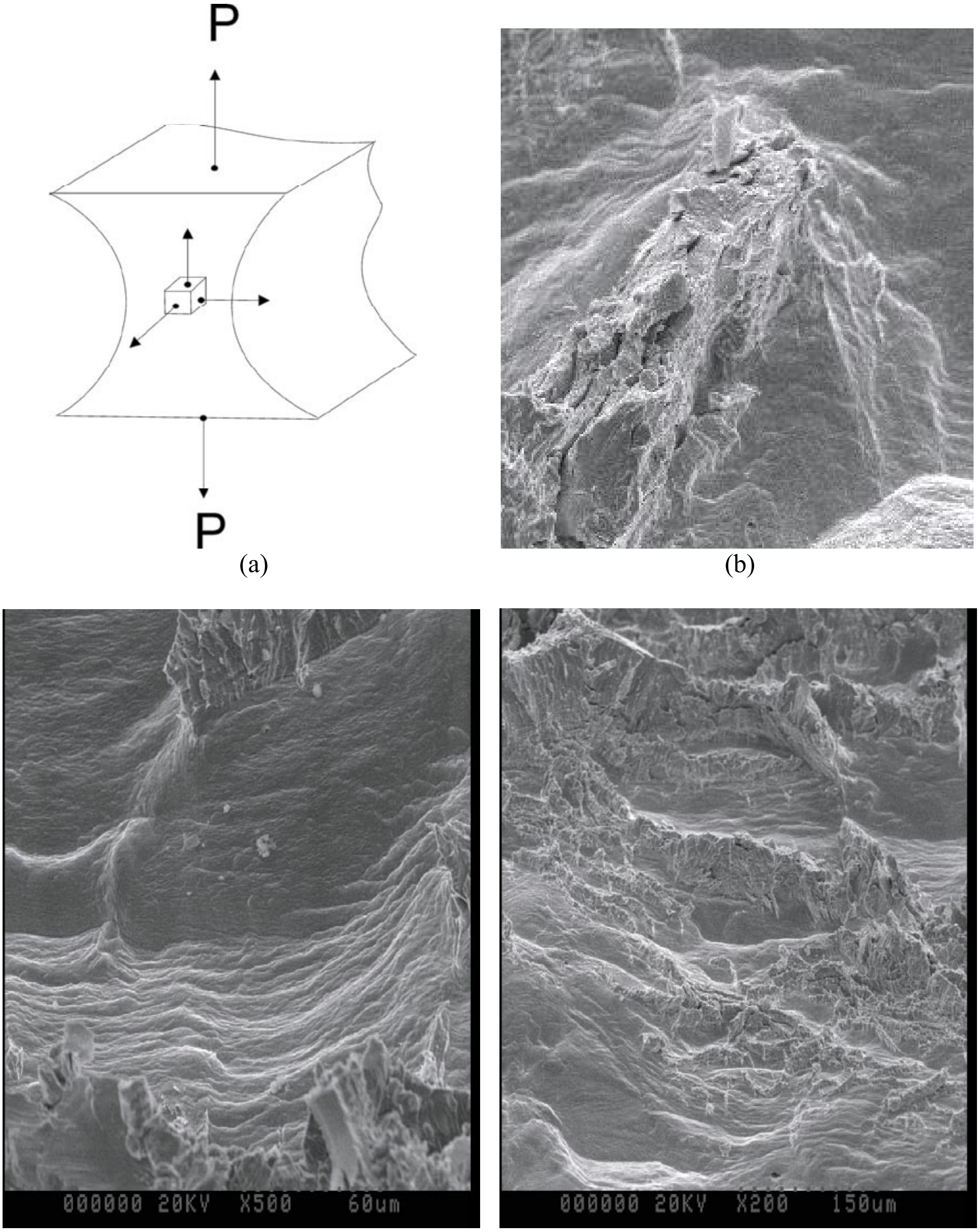

(a) (b)

(c) (d)

***Figure 35.*** *Brittle fracture of ligaments between SCC zones.*
*a – scheme of a three-axial stress state in a ligament (after Bridgman);*
*b, c, d – ‘brittle ridges’ of fractured ligaments.*

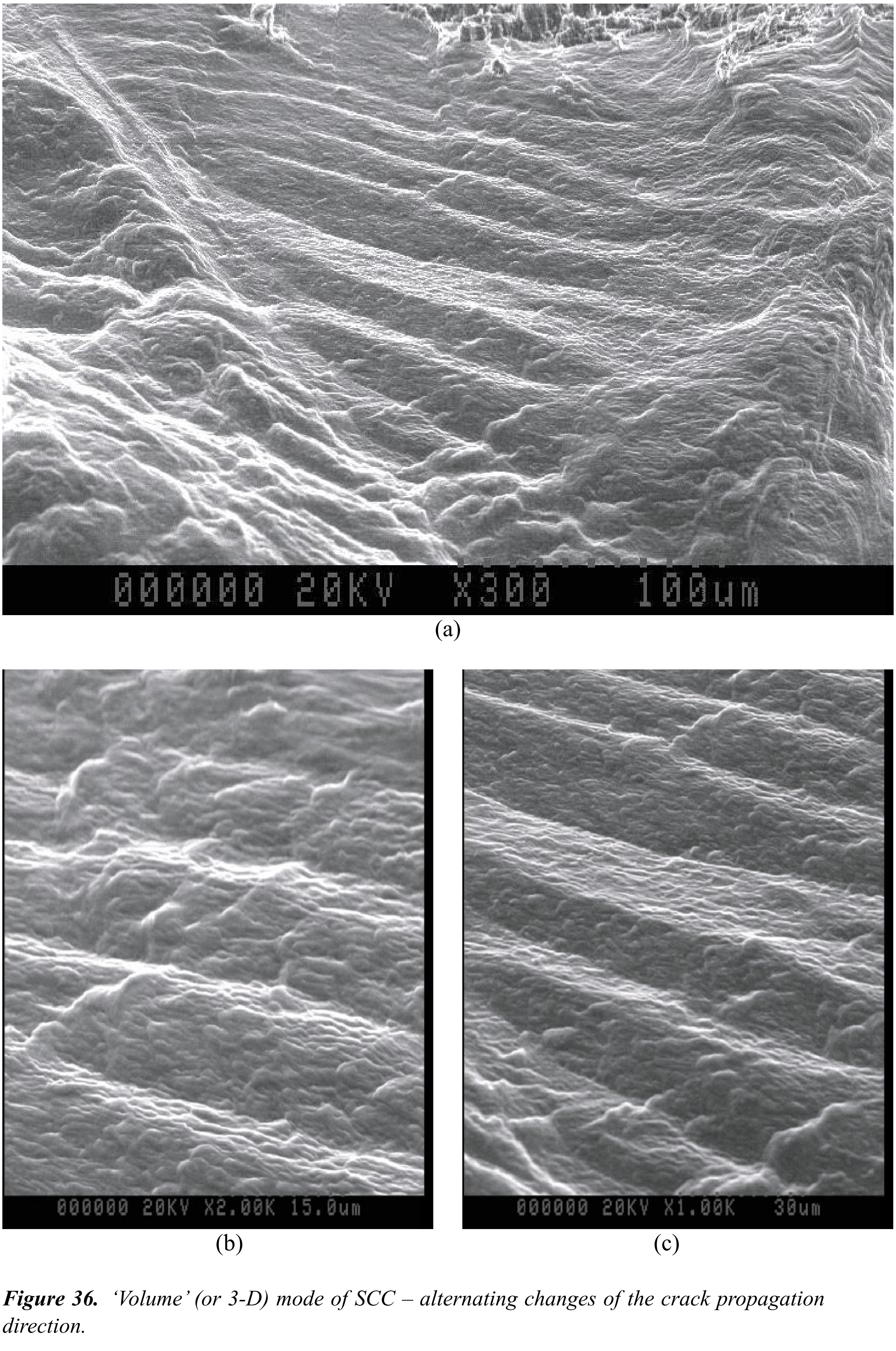

(a)

(b) (c)

***Figure 36.*** *'Volume' (or 3-D) mode of SCC – alternating changes of the crack propagation direction.*

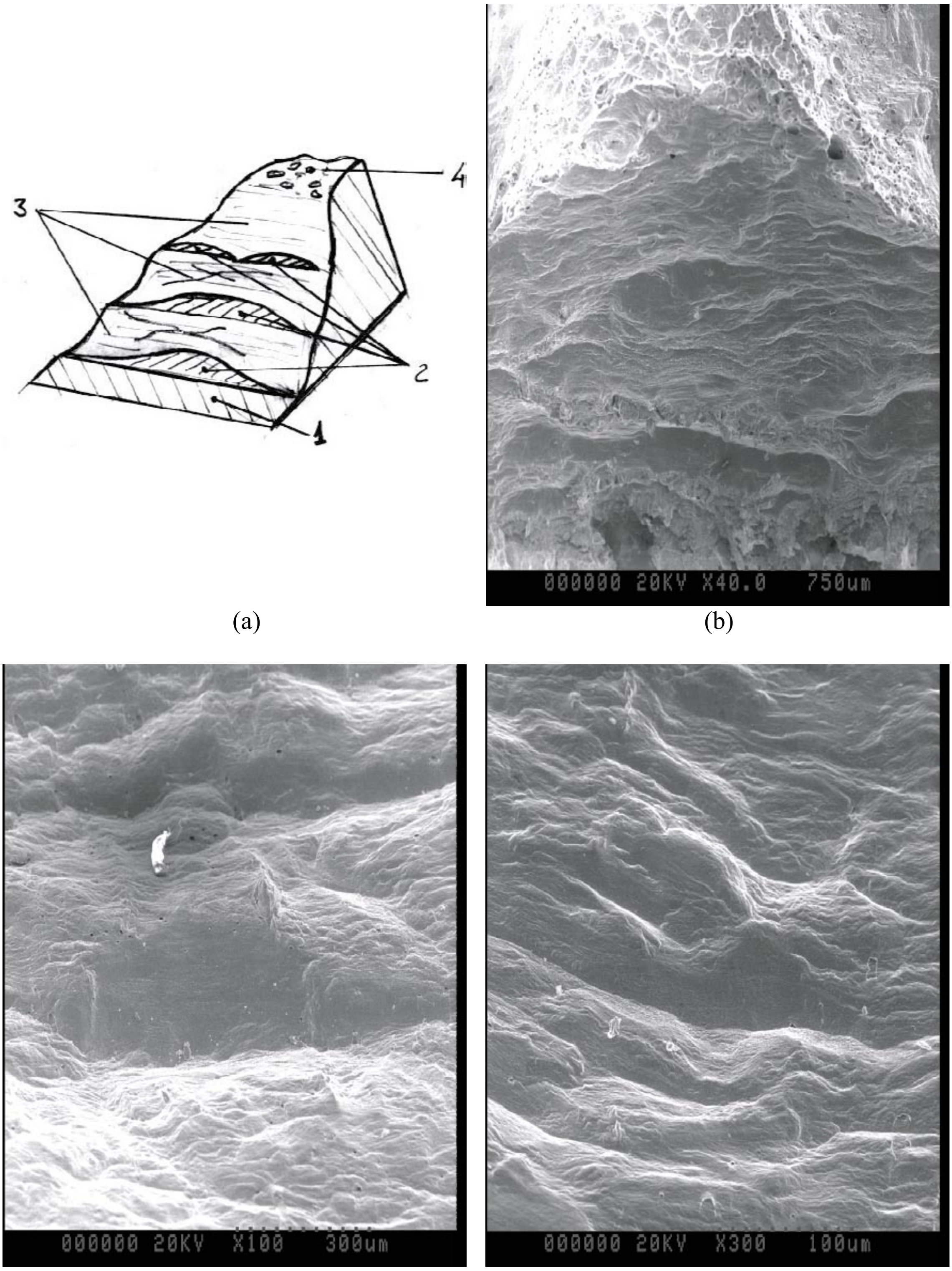

(a) (b)

(c) (d)

***Figure 37.*** *Corrosion under conditions of severe plastic deformation (continued next page).*
*a – scheme illustrating the development of plastic deformation accompanying SCC:*
*1 – fatigue pre-crack,*
*2 – SCC 'lobes',*
*3 – ductile 'stretch' zones,*
*4 – zone of ductile fracture;*
*b, c, d – fractured surfaces.*

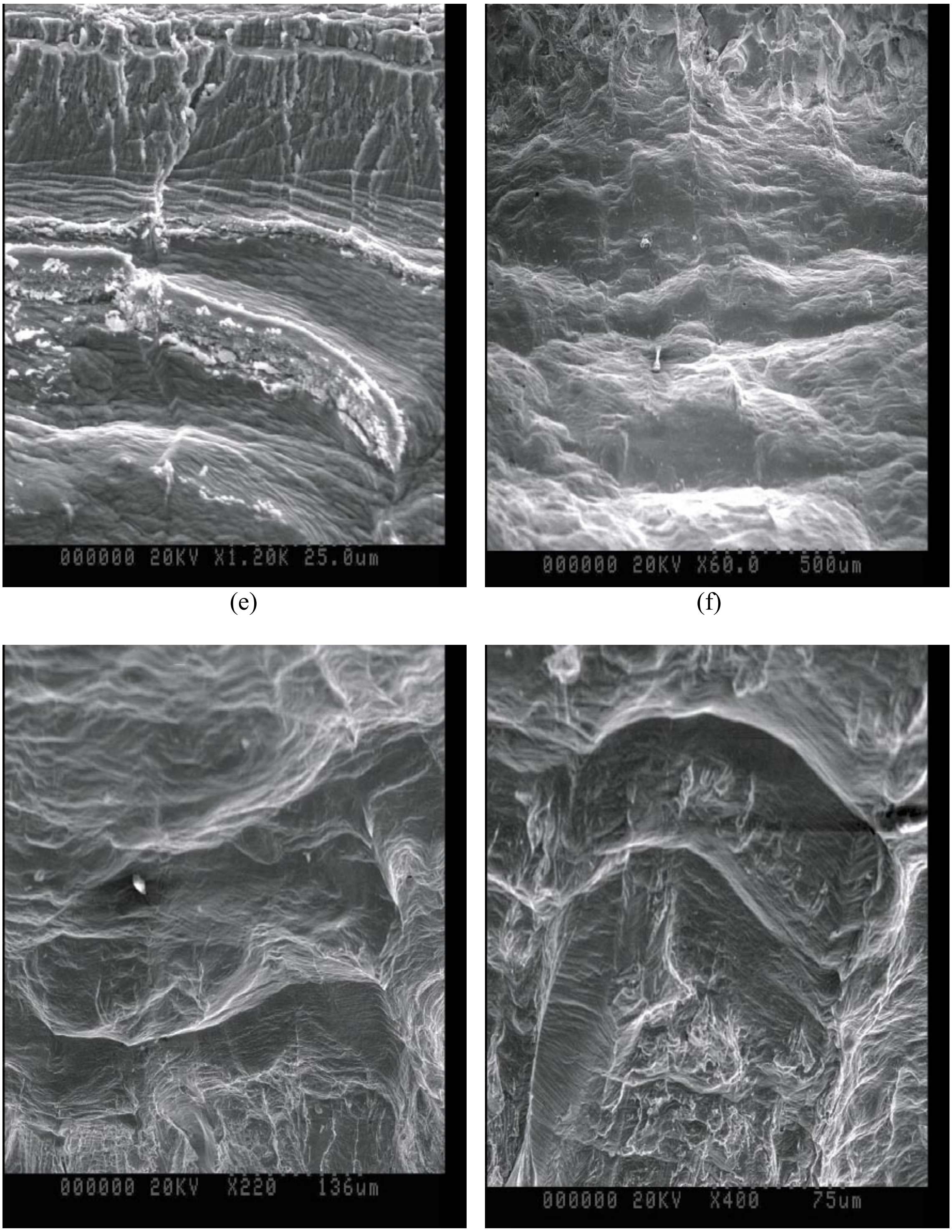

(e) (f)

(g) (h)

***Figure 37.*** *Corrosion under conditions of severe plastic deformation.*
*e, f, g, h – fractured surfaces.*

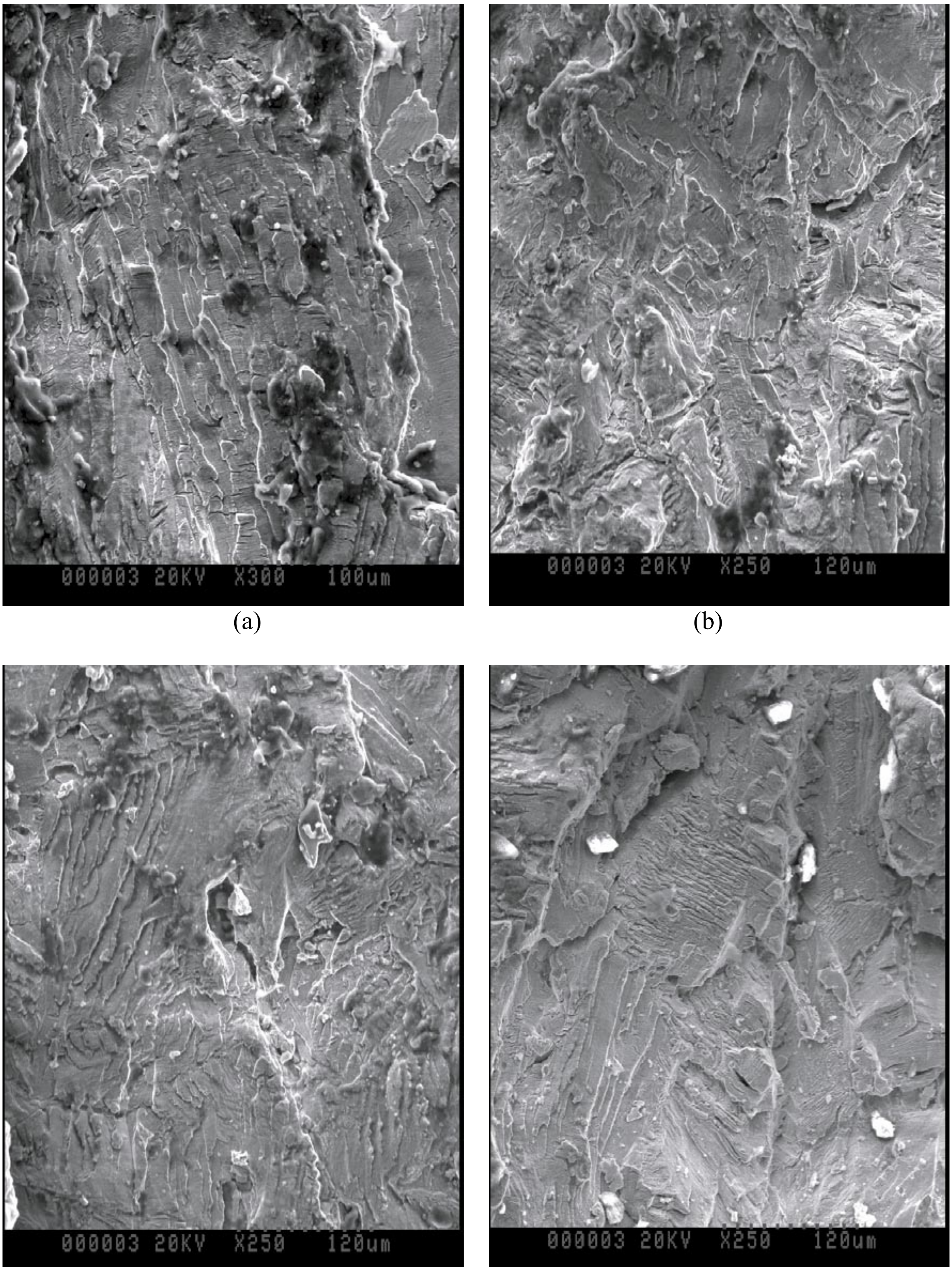

(a) (b) (c) (d)

***Figure 38.*** *Surface fractography of the fatigue-generated pre-crack in a CT specimen (continued on the next page).*

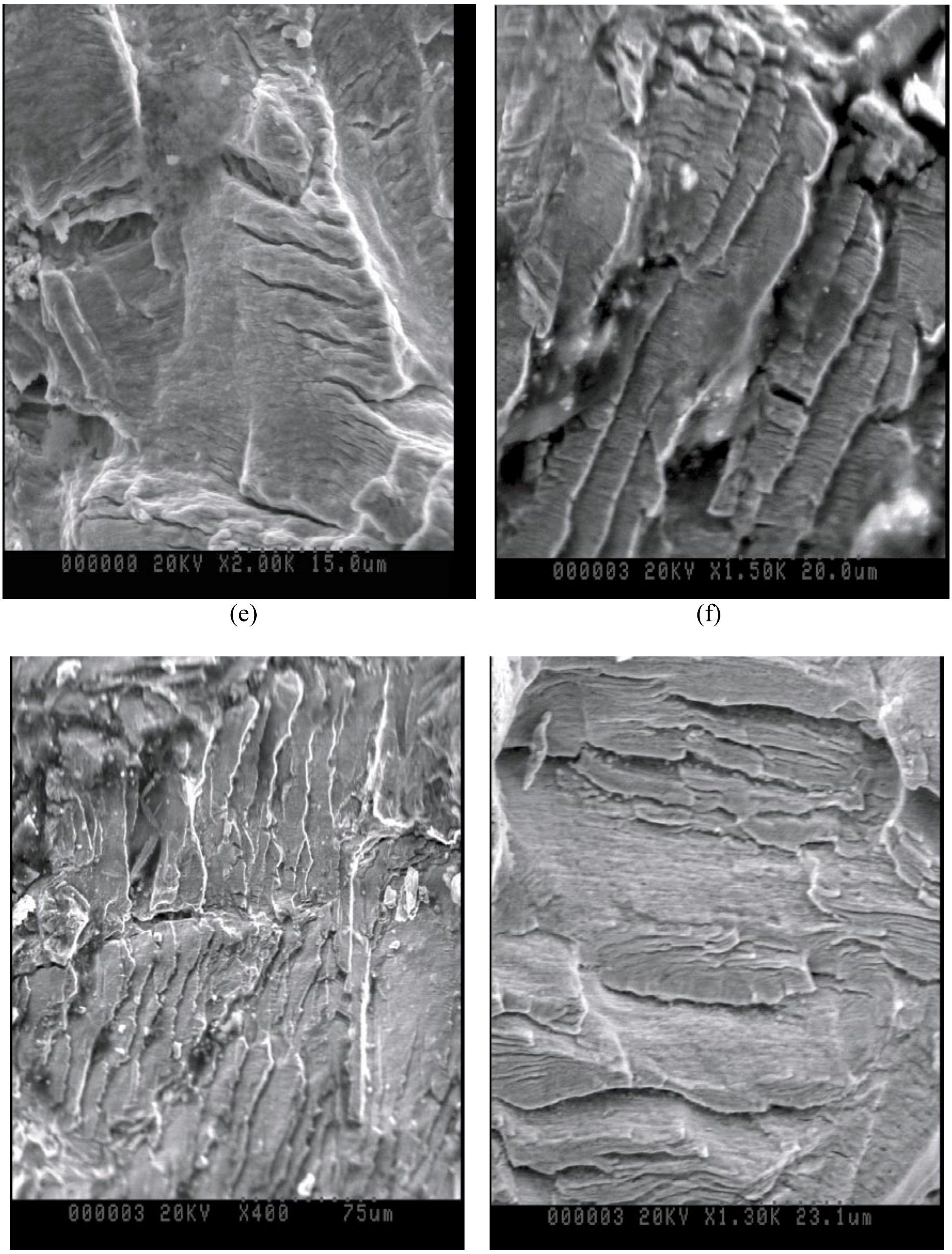

(e) (f)

(g) (h)

***Figure 38.*** *Surface fractography of the fatigue-generated pre-crack in a CT specimen.*

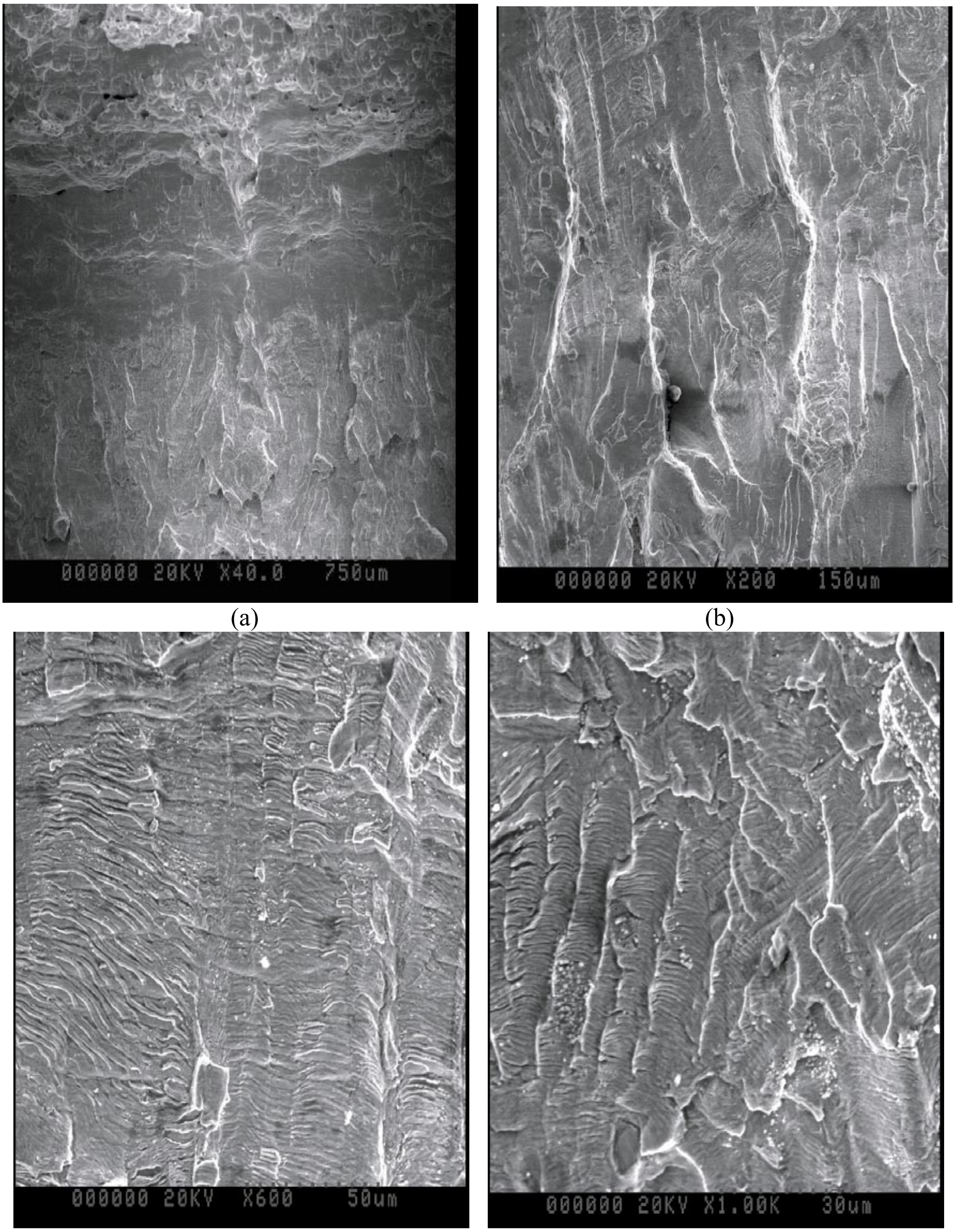

(a) (b)

(c) (d)

***Figure 39.*** *Fracture surface in the SCC zone of a CT specimen (continued on the next page).*
*a – panoramic view of the specimen fracture, from the fatigue pre-crack zone (bottom) to the ductile fracture zone (top). Fatigue pre-crack front is situated near the chain of pores (possibly, pits) in the lower part of the image;*
*b – transition zone to corrosion-assisted fracture (crack propagation from bottom to top);*
*c, d – regions within the SCC fracture zone.*

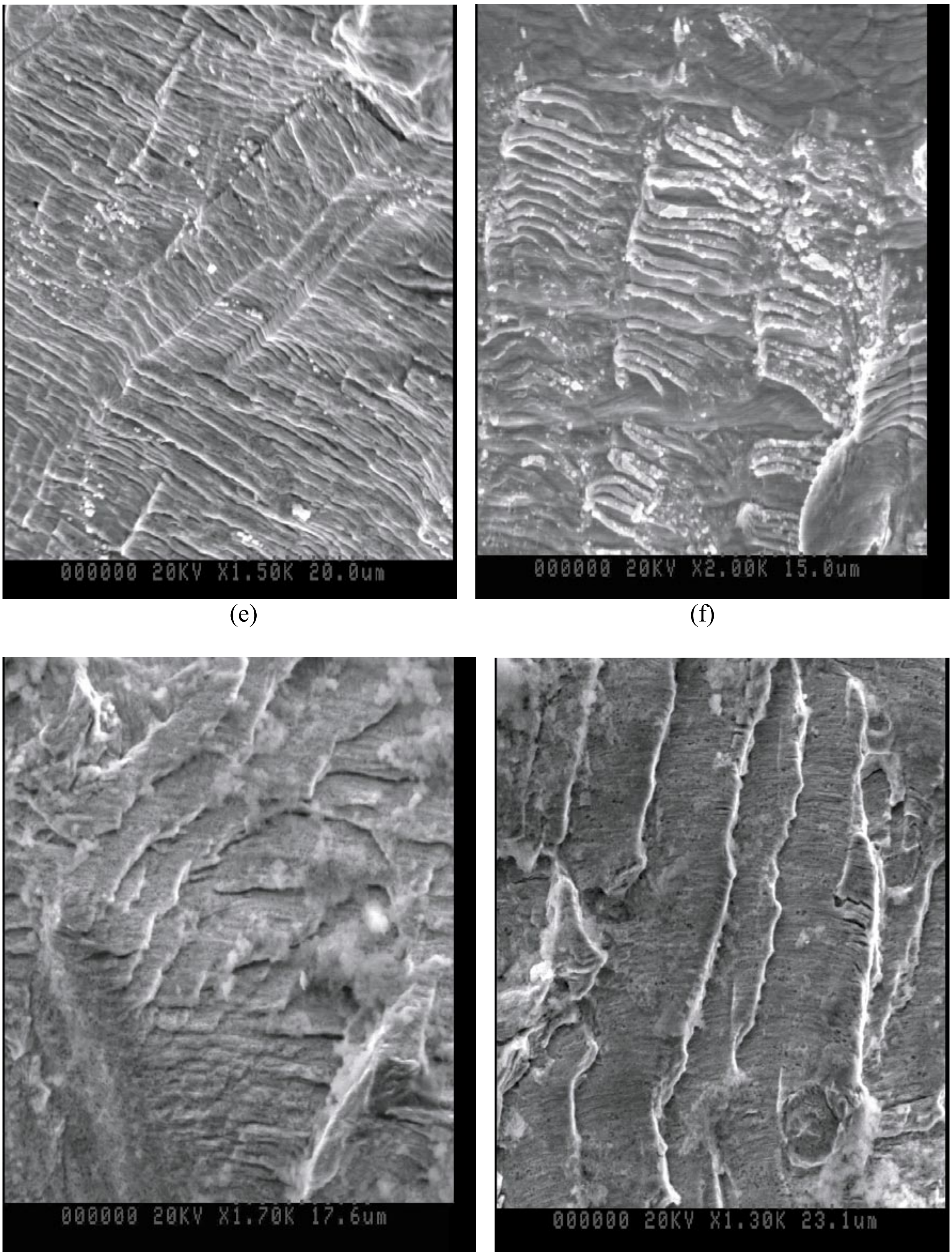

(e) (f)

(g) (h)

***Figure 39.*** *Fracture surface in the SCC zone of a CT specimen (continued on the next page).*
*e – transgranular crack propagation (bottom left to top right) through a twin (center);*
*f, g, h – regions within in the SCC fracture zone.*

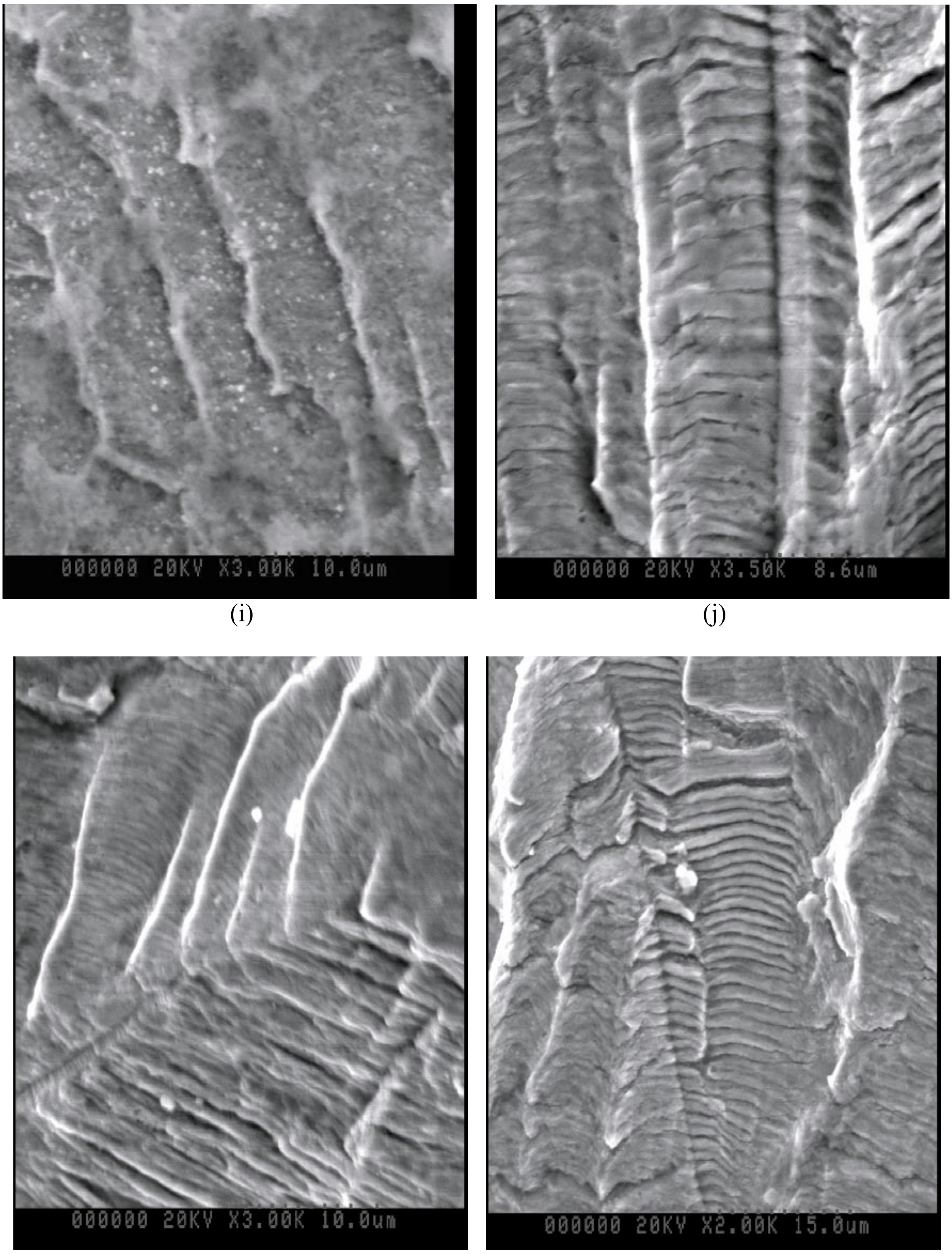

(i) (j)

(k) (l)

***Figure 39.*** *Fracture surface in the SCC zone of a CT specimen.*
*i, j, k, l – regions within the SCC fracture zone.*

ISSN 1404-0344
CM Digitaltryck AB, Bromma, 2005